UNIVERSIDADE DE LISBOA
FACULDADE DE CIÊNCIAS
DEPARTAMENTO DE FÍSICA

STUDY OF MULTICOMPONENT T_2* RELAXATION IN BRAIN TUMOURS

Mónica Rafaela da Cruz Mota Ferreira

Mestrado integrado em Engenharia Biomédica e Biofísica
Perfil em Sinais e Imagens Médicas

Dissertação orientada por:
Dr. Nuno Matela, Faculdade de Ciências da Universidade de Lisboa
Dr. Ana-Maria Oros-Peusquens, Forschungszentrum Jülich

2020

Abstract

Quantitative magnetic resonance imaging (qMRI) allows for the estimation of scanner-independent, tissue-specific parameters. By modelling the relaxation curves, qMRI can help inform on small pathological changes in the brain tissue, that might not be visible in the weighed images used typically in the clinic. However, the use of this imaging technique is often limited in the clinic by the prolonged measurement times and demand for very accurate estimation methods. To improve accuracy, noise reduction and field-inhomogeneity correction methods are of paramount importance. Additionally, the typical analysis of qMRI data assumes a single compartment per voxel, which is often oversimplified and can lead to biased estimations. This thesis addresses the effects of denoising, field-inhomogeneity correction and single compartment vs multiple compartment analysis in the estimation of the qMRI parameters water content and T_2*. We explore these effects in the WM, GM, CSF, tumour and oedema regions of a cohort of 33 brain tumour patients. The images were acquired using a multiple echo gradient echo sequence in a hybrid MR-PET system, which allows for the identification of active tumour tissue. To survey the effects of noise reduction in the estimation of the aforementioned qMRI parameters, we apply two denoising methods, namely Gaussian filtering and principal component analysis (PCA). Furthermore, the effects of two field-inhomogeneity correction methods, in particular sinc correction and voxel spread function (VSF), are also investigated. Finally, we compare mono-exponential models to multi-exponential models and the corresponding T_2* values of the different regions. In the case of multi-exponential model, no a priori assumptions about the number of exponential components are made. Regarding T_2*, high differences are found in the tumour region between the obtained mean T_2* with a mono-exponential approach (~58 ms) and the obtained geometric mean T_2* with a multi-exponential approach (~74 ms), across the different patients. High heterogeneity in the T_2* values is found for different tumour types, as well as inside of the active tumour tissue within the same patient, which lead to an individual study of each patient. Significant differences are found between the T_2* distributions within distinct regions of the active tumour tissue and the corresponding contralateral regions. Water content was found to be highly dependent on the used correction method. Overall, water content in the tumour is found to be close to that of GM, and higher than that of oedema. Water content in WM is lower than that of the other tissue classes. Finally, water content and geometric mean T_2* values do not display significant correlations in any of the tissue classes investigated, thus offering a complementary view of the properties of tissue. We conclude that a quantitative interpretation of T_2* relaxation in brain tumours is a very challenging task, but due to the heterogeneity found not only across the cohort but also within the active tumour tissue for each patient, it might be a potential non-invasive tool in monitoring, evaluation and grading of tumours.

Keywords: qMRI; field inhomogeneity; noise reduction; multi-exponential; T_2*.

Resumo

Nas últimas décadas, o desenvolvimento e aperfeiçoamento de modalidades de imagem tem revolucionado o tratamento de pacientes com as mais variadas patologias. Inúmeros estudos científicos têm surgido no seguimento destas técnicas com o objetivo de ajudar no diagnóstico, no prognóstico e na monitorização das doenças. É o caso do cancro que segundo a Organização Mundial de Saúde (acrónimo em inglês: WHO), é a segunda maior causa de morte a nível mundial.

Tumores cerebrais resultam do crescimento descontrolado de células, processo que pode ter origem direta no cérebro ou resultar da invasão de células de outros tecidos do corpo, também conhecido como metastização. Podem ser classificados como benignos ou malignos consoante os critérios de agressividade definidos pela WHO numa escala de I-IV. A alta subjetividade entre médicos na classificação dos tumores cerebrais levou a uma recente reformulação dos critérios de diferenciação que agora engloba tanto parâmetros fenotípicos como genotípicos. A sobrevivência dos pacientes está altamente dependente do tipo de tumor, do estágio em que se encontra aquando do diagnóstico e da avaliação médica que deverá definir o tratamento a ser aplicado. Os exames médicos que costumam ser realizados incluem imagem por ressonância magnética (acrónimo em inglês: MRI) e tomografia por emissão de positrões (acrónimo em inglês: PET).

No Instituto de Neurociência e Medicina – 4 (acrónimo em inglês: INM-4) do centro de investigação em Jülich, a existência de um scanner híbrido permite a aquisição simultânea de imagens de PET e MRI. Esta tese não engloba o estudo de PET mas a informação metabólica proveniente das imagens simultaneamente adquiridas é usada para gerar máscaras tumorais, utilizadas ao longo deste trabalho. A MRI é uma modalidade não invasiva que tem por base a aplicação de um campo magnético externo e a emissão de ondas de radiofrequência que variam no tempo. Tem as vantagens de não utilizar radiação ionizante e providenciar excelentes contrastes entre os diferentes tipos de tecido. O contraste da imagem depende do peso relativo dado aos parâmetros específicos aquando da aquisição. A possibilidade de adaptar o contraste consoante o que se pretende visualizar ou estudar, faz desta uma modalidade de imagem essencial tanto na clínica médica como em investigação científica.

A utilização de imagens ponderadas, também conhecido como *MRI qualitativo*, apresenta em si algumas limitações. A decisão do tratamento a aplicar é muitas vezes subjetiva, e pode diferir entre diferentes grupos de médicos. Por outro lado, o desenvolvimento de sequências que permitem a aquisição de séries de imagens introduziu a estimação de parâmetros específicos e independentes do scanner usados para avaliar quantitativamente os diferentes tecidos, o que é designado como *MRI quantitativo* (acrónimo em inglês: qMRI). Através da modelação das curvas de relaxação, qMRI pode ajudar na deteção de pequenas patologias no tecido cerebral, que podem não ser possíveis de observar nas imagens ponderadas usadas na clínica médica. Apesar das suas grandes vantagens, qMRI é maioritariamente uma área de investigação, e a sua inclusão clínica está ainda limitada pelo prolongamento do tempo de aquisição, necessário para adquirir as imagens extra, e pela necessidade de métodos de estimação com extrema exatidão e precisão.

Para este estudo, 33 pacientes (entre os 27 e os 76 anos de idade) com suspeita de tumor cerebral ou recorrência de tumores previamente tratados, foram submetidos à aquisição simultânea de MRI e PET. O estudo de modelos de relaxação exponencial foi realizado através de imagens ponderadas em T_2*, adquiridas com a uma sequência multi-eco gradiente-eco (acrónimo em inglês: mGRE).

T_2* permite caracterizar não homogeneidades de campo magnético associadas a concentrações locais de moléculas paramagnéticas, tais como o ferro. Contudo, existem outros fatores que contribuem para o decaimento exponencial mais rápido, nomeadamente contribuições de campos magnéticos externos não homogéneos. Uma vez que estas contribuições não contêm nenhuma informação sobre a fisiologia ou patofisiologia do tecido, torna-se necessário corrigir distorções associadas a campos magnéticos não homogéneos antes de qualquer método de processamento.

Neste trabalho, é estudada a influência de dois métodos de correção de campos magnéticos não homogéneos, nomeadamente sinc correction e voxel spread function (VSF). O método de sinc correction considera o desfasamento causado pelo intervalo entre fatias e estima uma modulação sinc do sinal, associada às distorções macroscópicas do campo magnético, para que o sinal seja posteriormente reconstruído. O segundo método, VSF, é um algoritmo matemático que corrige os efeitos do campo magnético não homogéneo nas direções de codificação da fase e da frequência.

Para estudar a influência dos efeitos de redução do ruído, dois métodos foram aplicados, nomeadamente filtragem Gaussiana e redução de ruído baseada na análise de componentes principais (acrónimo em inglês: PCA).

A típica análise de dados em qMRI assume a existência de um único compartimento por voxel, que muitas vezes é demasiado simplista e pode levar a estimativas tendenciosas. Na realidade, um voxel pode ser constituído por múltiplos compartimentos, cada qual com o seu próprio tempo de relaxação T_2*. Por isso, neste trabalho, comparam-se os resultados quantitativos de um modelo que descreve um único compartimento, com um modelo que descreve múltiplos compartimentos. Para tal, o algoritmo dos mínimos quadrados não negativos (acrónimo em inglês: NNLS) é utilizado, com a vantagem de não necessitar de um conhecimento prévio do número de compartimentos (ou seja, do número de exponenciais T_2*). Contudo, a relaxometria multi-exponencial é um problema mal condicionado onde várias soluções são possíveis, e, por isso, extremamente sensível ao ruído. Para ultrapassar estas dificuldades e estabilizar as soluções é utilizada uma versão regularizada do algoritmo NNLS, que adicionalmente requer uma restrição da regularização a usar. Para encontrar o melhor intervalo de parâmetros de regularização foi implementado o método da curva L. Com este método, foram também estudadas a influência de escalas logarítmicas e lineares no intervalo de soluções de T_2* e no intervalo de regularização.

Em relação aos valores de T_2*, foram encontradas diferenças significativas nas regiões tumorais entre a média de T_2* obtida com uma abordagem mono-exponencial (~58 ms) e a média geométrica de T_2* obtida com uma abordagem multi-exponencial (~74 ms), para todos os pacientes. É também demonstrada alta heterogeneidade nos valores de T_2*, não só entre pacientes, mas também dentro do mesmo tumor, o que levou a um estudo individual de cada paciente. São relatadas diferenças significativas entre regiões de tecido tumoral ativo e regiões de controlo localizadas no lado contralateral às regiões tumorais (aparentemente saudáveis). De um modo geral, os métodos propostos para remoção do ruído demonstraram reduções substanciais de ruído nas imagens, enquanto que ambos os métodos de correção das não homogeneidades de campo magnético não revelaram ser robustos, e no caso particular da VSF, sendo que bons resultados foram publicados em experimentos 3D, o problema pode estar associado a uma má otimização para o caso de experimentos 2D. O conteúdo de água foi considerado altamente dependente do método de correção usado. Verificou-se que o conteúdo de água em regiões tumorais é próximo ao conteúdo de água encontrado em regiões de substância cinzenta, e maior do que o encontrado em regiões de edema. Ainda, o conteúdo de água na substância branca apresentou valores inferiores que as demais regiões. Finalmente, foi estudada a relação entre o conteúdo de água e os valores de T_2^*, apesar de nenhuma correlação ter sido evidenciada nas diferentes regiões de interesse.

Com este trabalho concluiu-se que a interpretação quantitativa do relaxação de T_2^* em tumores cerebrais é uma tarefa complicada que exige métodos de elevada exatidão. No entanto, devido à heterogeneidade encontrada não só entre os diferentes tumores mas também no mesmo paciente, pode ser uma ferramenta não invasiva com potencial para monitorizar, avaliar e classificar tumores.

Palavras-chave: qMRI; campos magnéticos não homogéneos; redução do ruído; relaxometria multi-exponencial; T_2^*.

Contents

List of Figures

List of Tables

List of Abbreviations

2D	Two dimensional
3D	Three dimensional
B_0	External magnetic field
B_1	Time-varying magnetic field
CNS	Central nervous system
CSF	Cerebrospinal fluid
CT	Computed tomography
DNA	Deoxyribonucleic acid
FID	Free induction decay
FOV	Field of view
GM	Grey matter
gmT_2^*	Geometric mean T_2^*
GRE	Gradient echo
INM4	Institute of Neuroscience and Medicine 4
mGRE	Multiple-echo gradient-echo
MR	Magnetic resonance
MRI	Magnetic resonance imaging
M_{xy}	Transverse magnetisation
M_z	Longitudinal magnetisation
NLLS	Non-linear least squares
NNLS	Non-negative least squares
PCA	Principal component analysis
PDF	Probability density function
PET	Positron emission tomography
qMRI	Quantitative magnetic resonance imaging
QUTE	Quantitative T_2^* image
RF	Radio frequency
RMSE	Root mean square error
rNNLS	Reguralised non-negative least squares
ROI	Region of interest
ROIs	Regions of interest
SE	Spin echo
SNR	Signal-to-noise ratio
SPIO	Superparamagnetic iron oxide
SVD	Single value decomposition
T_2	Transverse relaxation time
T_2^*	Effective transverse relaxation time
TE	Echo time
VSF	Voxel spread function
WHO	World Health Organization
WM	White matter

1. Introduction

According to the World Health Organization (WHO), cancer is the second leading cause of death worldwide [1]. Brain tumours are one of the most common brain pathologies [2] and, in 2018, there were approximately 65 thousand new cases regarding brain cancer in Europe, and more than 50 thousand deaths [3], demonstrating that there is still a lot to understand about the morphologic changes and growth patterns of brain tumours. Combined or alone, radiation therapy, surgery and chemotherapy are the most common treatments for cancer even though there is a risk that the surrounding organs are affected.

Magnetic resonance imaging (MRI) is a non-invasive imaging modality that provides medical information by using a static magnetic field and additional time-varying magnetic fields to excite nuclei in the tissue. In contrast to other commonly used imaging modalities, such as computed tomography (CT) and positron emission tomography (PET), MRI does not employ ionizing radiation, which, coupled with its excellent soft-tissue contrast, makes MRI an essential imaging modality for both clinical routine and scientific research.

For the past decades, methodological research and the constant development in hardware, have improved the quality and contrast of medical images. The typical MRI experiment is tuned in such a way that the measured images turn out weighted to a specific parameter. This means that if the experiment tuning is not the same from one experiment to the next, the measured images will not be the same, despite potentially showing similar contrasts. This is often called *qualitative* imaging [4].

However, *qualitative* MRI often does not provide enough information regarding the integrity of the tissue, and irreversible damages are often expected since pathologies cannot be predicted before differences in the image contrast are clear. On the other hand, in *quantitative* MRI (qMRI) the magnetic resonance (MR) parameters, which are a reflection of the microstructure of the tissue at a microscopic level [5], are estimated from a series of images [6]. In the clinical routine, qMRI holds great promise in the detection and monitoring of changes in the MR parameters due to pathologies [4]. Nevertheless, qMRI is slowly finding its way into the clinical routine due to the longer measurement times to acquire the multiple images required [7]. Additionally, the accuracy and precision of the estimated parameters is influenced by the number of data points as well as the signal-to-noise ratio (SNR) [8].

In qMRI, each microstructural environment can be characterised by the estimated relaxation time of that specific compartment [7]. Although an image voxel can contain multiple micro-environments with very different relaxation times, it is common to assume that each voxel can be described by a single relaxation time. Naturally, in a nonhomogeneous voxel, assigning a single time value is often too simplistic and leads to biased estimations. A better, more accurate approach is to consider several homogenous compartments within the voxel, each one with its own relaxation time [9]. This multi-compartment model allows for a more detailed characterisation of the water compartmentalization and retrieves information at the sub-voxel level [10]. Multiple sclerosis, for example, is a neurodegenerative disease where the myelination is affected [11]. A model where the myelin pool is possible to be characterised can be used to describe the small changes originated by the disease and, therefore, be used in its early diagnosis. qMRI and especially multi- compartment models can therefore have an important role in the study of brain tumours.

Among others, multi-echo spin-echo (MESE) and multi-echo gradient-echo (mGRE) sequences can be used for exponential relaxometry models, where a series of transverse relaxation (T_2) and effective transverse relaxation (T_2*) weighted images are acquired, respectively [7]. However, mGRE sequence has some advantages since it provides faster acquisition time and lower specific absorption rate (SAR), which is extremely relevant at high field strengths [12]. Particularly, T_2* characterises static magnetic field inhomogeneities on the mesoscopic level (see more in section 2.6), which is associated with local concentrations of paramagnetic molecules, such as iron [13]. However, T_2* is also sensitive to external magnetic field variations and, therefore, inhomogeneity correction methods need to be applied as a pre-processing step [13], [14]. Additionally, in order to improve lower SNR provided by the mGRE sequences, denoising techniques are often implemented [7].

We investigate the presence of specific T_2^* components in brain tumours, based on a multi-component decomposition of T_2^* relaxation curves. Different techniques can be used although the most common approaches are the non-linear least squares (NLLS) and the non-negative least squares (NNLS) algorithms [7]. In this work, a NNLS algorithm is used, since, unlike NLLS, the NNLS algorithm determines a solution to the problem with no prior knowledge of the number of exponentials (i.e. compartments) in the time signal. Since more than one solution is possible, multi-exponential relaxometry presents itself as an ill-conditioned problem, and, therefore, extremely sensitive to noise and measurement imperfections [6][7]. For these reasons, denoising and magnetic field inhomogeneity correction methods have an even higher relevance. Additionally, to deal with potential remaining noise in the images, regularisation is used in order to improve stability (rNNLS) [6], and only requires a regularisation constraint [7].

In this thesis we investigate another quantitative parameter to the characterisation of the brain and brain tumours. Most of the MRI visible protons belonging to the brain are related to the existence of water molecules that form layers of hydration around molecules, ions and membranes, with whom they interact directly [8]. Water content is highly regulated in the healthy brain and for this reason, even small pathological changes can be easily identified. Extracting the water content is, however, a non-trivial task due to the need of numerous corrections (see more in section 3.4.1). It demands techniques with very high precision [15][16] where noise reduction is extremely important.

In summary, the main goals of this work include (1) comparing mono and multi-exponential models to characterise regions of interest (ROI) in the brain, (2) comparing and studying the influence of denoising and magnetic field inhomogeneity correction methods in both, mono and multi-exponential approaches, (3) studying the existence of tumour characteristic peaks, and (4) correlating water content and effective transverse relaxation time (T_2*) values.

This thesis is divided into 5 chapters. The theoretical background behind MRI, the state-of-the-art of brain tumours and the theory of the used algorithms are summarised in Chapter 2. The materials and methods used are described in Chapter 3, including information about the subjects and the means used for processing the data. In chapter 4 are presented the results and discussion of this project. And finally, Chapter 5 contains the main conclusions and further work to be consider from the study.

2. Background Theory

2.1 Cellular types and the central nervous system

The central nervous system (CNS) is composed of two groups of cells, glial cells and neurons. Neurons are responsible for processing and transmitting information in the form of action potentials (electrical signals) and are composed of four important sections: the soma or cell body, where the nucleus that is responsible for cellular metabolism resides; the dendrites, which transmit the received signal from other neurons; the axon, along which the action potentials are conducted; and the axon terminals (or synaptic endings), which relay the information to the next neuron by releasing neurotransmitters [17]. Glial cells are the supporting cells of the brain and are also responsible for protecting the neurons and assuring their nourishment and electrochemical stability. In the CNS, glial cells can be differentiated in four major cell types: astrocytes, which provide structural and metabolic support; oligodendrocytes, which insulate the axons by surrounding them with myelin sheaths; microglia, which are activated in response to tissue damage; and ependymal cells which are attached to astrocytes and produces the cerebrospinal fluid (CSF) [18].

Myelin integrity plays an important role in brain function since myelinization increases the thickness of the membrane and decreases the amount of charge stored on both sides of the membrane. Therefore, myelin reduces internodal membrane capacitance and provides a faster conduction of the action potentials [19].

The CNS is spatially characterized by having white matter (WM) and grey matter (GM). While the GM contains the cell body of neurons and some glial cells, the WM is approximately 40% consisting of myelinated axons [20]. Furthermore, because 70-85% of the brain mass consists simply of H_2O, four compartments, so-called intracellular water, extracellular water, myelin water (between myelin sheets) and cerebrospinal fluid, can be established [21]. These different water compartments can be seen in figure 2.1, where an electron micrograph shows a cross section of a myelinated axon.

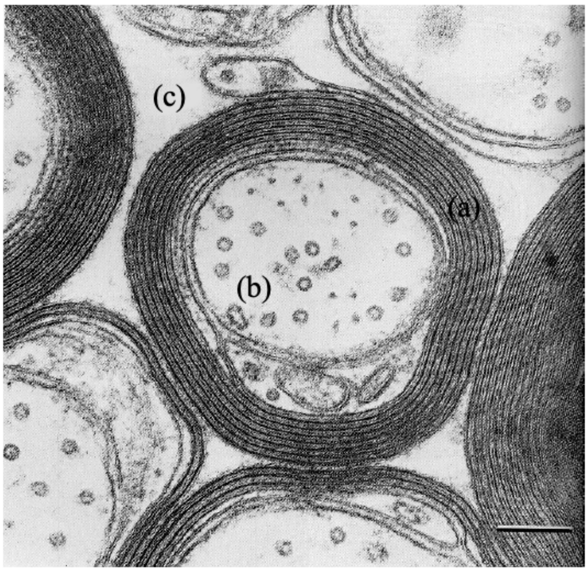

Figure 2.1- Electron micrograph of a myelinated axon. Indicated by a) is the myelin sheets, b) intracellular water and c) extracellular water. The bar in the right bottom represents 0.1 µm x 15000 (taken from[22]).

2.2 Brain tumours

A tumour is an uncontrolled growth of cells in the tissue and the cause of most brain tumours is not fully understood [23]. Normal human cells grow, and function based mainly on the information in each cell's DNA (deoxyribonucleic acid). Oncogenes are genes that contribute to the cell growth, cell division and help cells to stay alive. On the other hand, tumour suppressor genes are genes that maintain the cell division under control, repair mistakes in DNA or assure that apoptosis, i.e. cell death, occurs at the right time [24]. Brain tumours, like other tumours, can be caused by mutations in the DNA that turn on oncogenes or turn off tumour suppressor genes [25].

In order to characterize brain tumours, the WHO established the standard system for the classification of tumours of the CNS. In 2007, this classification was based on histological information from microscopic comparisons between different putative cells and their supposed differentiation levels. This classification system often lead to some doubts among pathologists, and so, eight years later, the 2016 WHO classification of CNS tumours introduced both phenotypic and genotypic parameters to avoid subjectivity [26]–[28].

The rating scale is used to classify the type of tumour as benign or malignant, on a scale from grades I to IV as an indication of aggressiveness. Benign tumours are usually localised, and the surrounding tissue is typically not invaded. Unlike benign tumours, malignant tumours often need several treatment sessions and/or surgeries for tumour removal due to the infiltration in the surrounding healthy tissues or due to spreading to other parts of the body. Table 2.1 summarizes all grades of CNS tumours according to the following four criteria: cytological atypia, mitotic activity, microvascular proliferation and necrosis [29].

Table 2.1- CNS tumour classification according to the above criteria of the WHO [26].

CNS tumour grading	
Grade I	Characterized by a slow growing, these tumours are non-malignant and a long-term survival is expected. Tumours of grade I do not satisfy any of the for four criteria.
Grade II	Characterized by a slow growth but can be malignant or non-malignant. Tumours of grade II satisfy the cytological atypia criteria.
Grade III	Characterized by its malignancy, these tumours often recur as higher-grade tumours. Tumours of grade III satisfy the anaplasia and the mitotic activity criterions.
Grade IV	Characterized by a rapid growing, these tumours are very aggressive malignant tumours. Tumours of grade IV show anaplasia, mitotic activity with microvascular proliferation, and/or necrosis.

Primary brain tumours originate in the brain and can develop from brain cells, membranes, nerve cells and glands which will define the respective name of the tumour. Secondary brain tumours, or metastatic tumours, originate from other parts of the body [30]. Knowing the cell type and the grade of tumours is essential to determine the appropriated treatment and the prognosis but, nowadays, the tissue analysis is done by biopsy, a highly invasive method.

Highly accurate and non-invasive diagnostic methods are desirable to identify the type of tumour, and these can be provided by advanced imaging techniques. For the past decades, unnecessary surgeries were avoided with the introduction of non-invasive imaging methods, e.g. MRI, CT and PET [31].

MRI represents an essential tool in the clinical routine, since it provides detailed anatomic images of the brain tumour and the surrounding tissues with a superior soft tissue contrast and high-resolution information. However, MRI lacks specificity and is, therefore, not so suitable to provide with metabolic information.

2.3 Magnetic Resonance Imaging

2.3.1 MRI Physics

Magnetic resonance imaging is a powerful imaging technique that uses non-ionizing radiation and strong magnetic fields to provide *in vivo* images of the human body. Its fundamental principle is based on the interaction of a nucleus with the strong magnetic fields. The nucleus is composed of protons and neutrons. These are atomic particles and have intrinsic quantum mechanical properties, one of which is spin angular momentum, often abbreviated as spin. Both protons and neutrons contribute to the spin of the nucleus. Only nuclei with non-zero spins are suitable for MRI, since these are the only ones which can absorb and emit electromagnetic radiation when subject to an external magnetic field. The spin property is represented in figure 2.2 and can be classically portrayed as the rotation of the nucleus around its own axis.

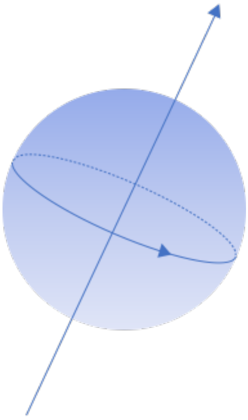

Figure 2.2 – Spinning nucleus creating a magnetic moment.

In MRI, hydrogen is the most commonly used element due to its abundance in the human body and its sensitivity to the MR signal. The magnitude of spin is quantised which means that the possible values are semi-integer steps. In the case of hydrogen, the atom is a single proton and its possible values of the spins' z-component are given by [32]

$$I_z = \pm\frac{1}{2}\hbar, \qquad 2.1$$

where $2\pi\hbar = h =$ Planck's constant. Associated to every nuclear spin is a magnetic dipole moment by the relationship [32]

$$\boldsymbol{\mu} = \gamma\boldsymbol{I}, \qquad 2.2$$

where γ is the gyromagnetic ratio, which is nuclear-specific (for hydrogen, $\gamma = 267.513 \cdot 10^6\ rad/(s \cdot T)$). Spins possess a unique characteristic that allows magnetic resonance, they precess. The type of nucleus and the strength of the magnetic field applied, will define the speed or characteristic frequency of precession. This frequency at which protons precess is called Larmor frequency and is defined as [32]

$$\omega_0 = \gamma B_0. \tag{2.3}$$

Where B_0 is the external magnetic field. Without B_0, the spins are randomly oriented, and their spins cancel each other, leading to a null net magnetization. In the presence of a static external magnetic field B_0, the z-components of the nuclear magnetic moments tend to align themselves with the direction of the field. Since protons have a spin quantum number of ½, its spin has two eigenstates, often referred to as "spin up" or "spin down" states. The energy values of the two possible orientations are given by [32]

$$E_{\uparrow,\downarrow} = \mu_{z_{\uparrow,\downarrow}} B_0 = \mp\frac{1}{2}\hbar\gamma B_0, \tag{2.4}$$

and therefore

$$\Delta E = \hbar\gamma B_0. \tag{2.5}$$

When a photon with energy $E_{photon} = \hbar\boldsymbol{\omega}$ interacts with a spin and matches the energy difference ΔE, it causes a transition of the state [33]. This transition means that the spins in the up orientation will switch to the down orientation, which is described by the Zeeman splitting. The up state has the lower energy, whereas the down state is the less stable state as it has a slightly higher energy. The Zeeman splitting is graphically represented in figure 2.3.

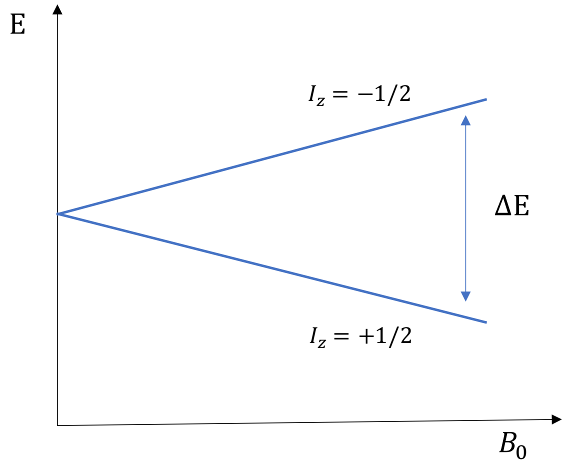

Figure 2.3 - Zeeman splitting in an external magnetic field B_0.

The number of excess spins in the lower energy state depends on the external magnetic field strength, the sample temperature and the overall number of protons. The ensemble of hydrogen atoms are distributed according to the Boltzmann distribution [32],

$$\frac{n_\downarrow}{n_\uparrow} = e^{-\Delta E/k_B T}, \tag{2.6}$$

where k_B corresponds to the Boltzmann constant and T to the temperature. However, only a few numbers of nuclei change to the lower energy state and therefore, only those few spins in the up state participate in the MR signal. The measurable macroscopic magnetisation M is associated to this small excess of spins, which is the ensemble average of the nuclear magnetic moments. In a homogeneous magnetic field, as long as all (excess) spins are of random phase orientation, rotating at the same frequency, their transverse components to the magnetic field cancel to zero (parallel to the xy-plane), and therefore, M will only be along the z-axis. The behaviour of M in the presence of an external magnetic field is described by Bloch's equations [34]. By the moment that the magnetization is no longer in the parallel state, it starts precessing about the external magnetic field direction. Since the magnetization vector is precessing in space, it can be described by its transverse components $M_x(t)$, $M_y(t)$ and longitudinal component $M_z(t)$

$$\frac{d\boldsymbol{M}}{dt} = \boldsymbol{M} \times \gamma \boldsymbol{B} \Rightarrow \boldsymbol{M}(t) = \begin{pmatrix} 0 \\ \boldsymbol{M}_0 \cdot \sin(\omega t) \\ \boldsymbol{M}_0 \cdot cos(\omega t) \end{pmatrix} \qquad 2.7$$

if the initial condition (at equilibrium) is $\boldsymbol{M}(0) = (0,0,M_0)^T$ [34]. During excitation, the magnetization is tipped away from the longitudinal magnetization by applying an external field B_1, perpendicular to B_0, for a short time, often called the excitation pulse. The amount of destabilization is given by the flip angle, $\alpha = \angle(\boldsymbol{M}, \boldsymbol{B}_0)$. When the B_1 field is turned off, the spins relax back into the equilibrium, releasing energy, which is then measured by the receive coils of the scanner [35].

Ideally, all spins precess with the same frequency in the presence of a homogeneous magnetic field. However, due to spin-spin interactions, the spin ensemble starts to dephase by interacting with the surrounding substances, which leads to a distribution of resonance frequencies. It can be observed that the measured signal decays with relaxation time constant referred to as T_2, transverse or spin-spin relaxation. The evolution of M_{xy}, after the application of an excitation pulse, is given by [32]

$$M_{xy}(t) = M_{xy}(0)e^{-t/T_2} \qquad 2.8$$

As a matter of fact, M_{xy} decays much faster due to the additional dephasing caused by inhomogeneities in the external magnetic field. This way, T_2* relaxation, or effective transverse relaxation, represents the decay caused by T_2 relaxation, combined with magnetic field inhomogeneities (T_2'), and their relationship is given by [33]

$$\frac{1}{T_2^*} = \frac{1}{T_2'} + \frac{1}{T_2} = \frac{1}{\gamma \, \Delta B_0} + \frac{1}{T_2} \qquad 2.9$$

2.3.2 Imaging principles

Phenomena play a part in decomposing the acquired MR signal into its contributions from the different locations in the brain. And these are the slice selective excitation, frequency encoding and phase encoding.

In two-dimensional (2D) MR experiments, it is possible to select a specific plane of interest by applying a slice selection gradient simultaneously with a limited bandwidth radio frequency (RF) -pulse. Firstly, the slice selection gradient in the z-direction, G_z, results in a linear dependency between the resonance frequency and the spatial position $r_{z'}$. Secondly, the applied excitation pulse leads to the formation of transverse magnetization at the locations where the Larmor frequency matches the frequency of the pulse [33]. As it is represented in figure 2.4, the excitation with a rectangular slice profile of width $\boldsymbol{\Delta\omega}$ in frequency domain, corresponds to the Fourier transform of the temporal pulse shape, i.e., a sinc pulse in the time domain.

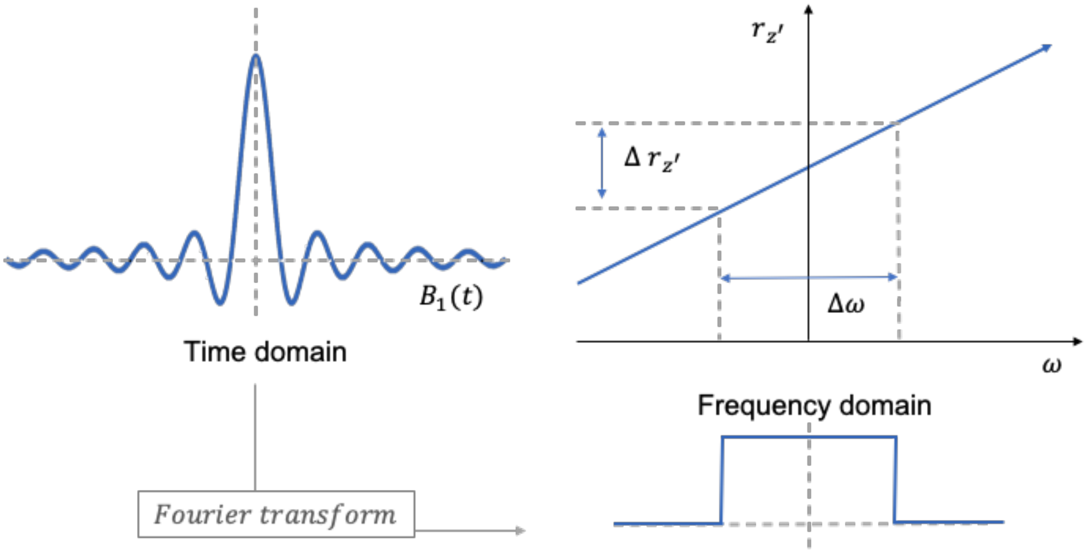

Figure 2.4 – Slice selective excitation. On the left, a sinc pulse in the time domain generates a rectangular spectrum of width $\Delta\omega$. On the top right, the frequency pulse excites a slice of finite thickness $\Delta r_{z'}$.

The combination of the previous steps ensures that it is possible to differentiate the signal between protons of different slices.

Between the excitation and the read-out period, a phase encoding gradient is applied to establish one of the two remaining spatial dimensions. Commonly along the y-direction, the phase encoding gradient, G_y, causes the phase of the precessing protons to vary depending on their y-position.

The third spatial dimension is encoded by another gradient referred to as frequency encoding gradient, which is applied during the read-out period. Usually in the x-direction, the frequency encoding gradient, G_x, assigns the frequencies to the x-position according to

$$\boldsymbol{\omega}(\boldsymbol{x}) = \omega_0 + \gamma \boldsymbol{G_x x} \qquad 2.10$$

K-space and image reconstruction

The frequency-encoded data collected from the scanner is then used to fill in a data matrix, typically referred to as k-space. This matrix contains the image points in the frequency domain. In order to reconstruct the image, a 2D Fourier transform is applied to the space of spatial frequencies (k_x, k_y), which will then retrieve the coordinates in the physical system (x,y). Therefore, a point in the k-space matrix does not correspond to a point in the image matrix [36].

General information about the contrast, brightness and shape of the image is provided by the low spatial frequencies, filled in the center of the k-space. On the other hand, the details of the structures, edges and contours of the image is provided by the high spatial frequencies, filled in the periphery of the k-space [36].

The size of the field of view (FOV) in the x- and y-directions is limited by the spacing between samples in k-space, Δk_x and Δk_y. Additionally, k_x and k_y have limited maximum values according to the desired resolution of the final image. The FOV is inversely related to Δk, and the pixel width is inversely related to k_x and k_y.

K-space has a particular property of symmetry, known as Hermitian conjugate symmetry, that reflects the redundancy between the real and imaginary components located diagonally from each other across the origin of k-space [37]. Consequently, part of the k-space can be inferred, and the matrix does not need to be fully sampled. Inferring k-space leads to smaller acquisition times, although often at the cost of image quality [38]. A drawback of this approach is that the magnetic field is assumed to be homogeneous. However, magnetic field inhomogeneities lead to imperfect approximations of the inferred portion of the k-space, and, therefore, to image artefacts [37].

Two major partial Fourier techniques exist to estimate the missing data. *Half Fourier*, or phase-conjugate symmetry, allows for the reduction of the number of phase encoding steps and estimates the lower half of the k-space from the top half. Therefore, k-space consists in full lines but only half of the lines and some few extra lines are measured to correct imperfections [36], as it is represented in figure 2.5 (left panel).

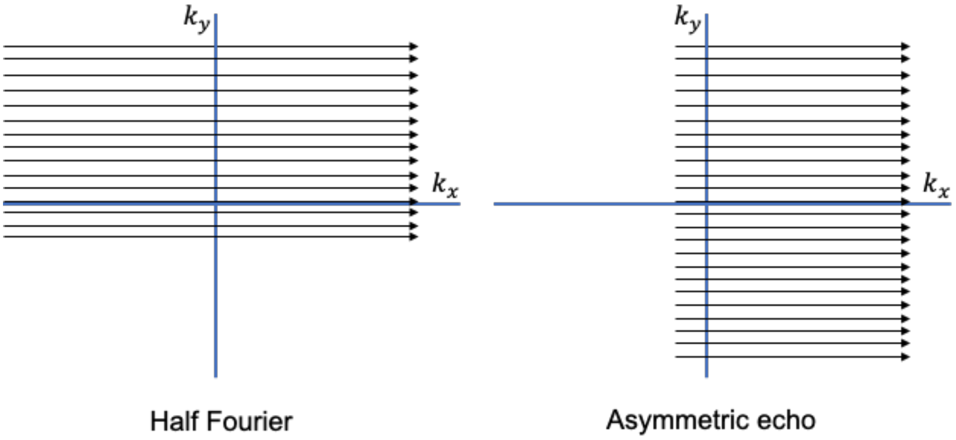

Figure 2.5 – K-space sampling techniques.

Asymmetric echo, or read-conjugate symmetry, is another technique where, unlike the previous method, all phase encoding steps are acquired. Instead, the missing k-space arises from a short echo time (TE) where the early portion of the echo may overlap in time the free induction decay (FID) but can then be reconstructed from the acquired back half of the echo [38].

2.3.3 Echo sequences

One of the main advantages of MRI is its flexibility regarding different types of contrast, obtained through the application of MR sequences. The two most common types of echo sequences, which allow the measurement of T_2 and T_2*, are the *spin-echo* (SE) sequence and the *gradient-echo* (GRE) sequence, respectively.

In SE sequences, a 90º RF-pulse is applied simultaneously with the slice selection gradient to tip the spins into the transverse plane. Since spins interact with other spins, they become out of phase and a

180º RF-pulse is applied together with the slice selection gradient, at an arbitrary time t, to rephased them. At time 2t, equals to TE, the phase coherence is achieved which causes the echo formation [39]. A schematic overview of a SE sequence is shown in figure 2.6.

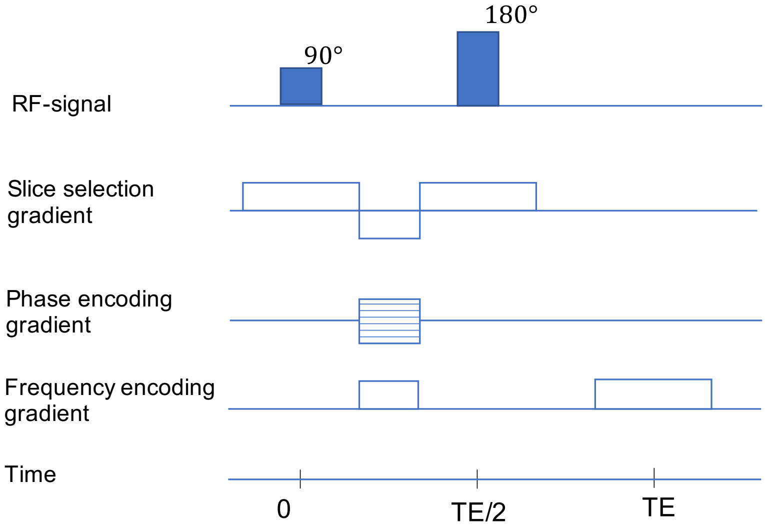

Figure 2.6 – Spin-echo sequence diagram. A 90º pulse is applied for excitation. At TE/2 a 180º pulse allows to refocus the spins that will form the signal at TE.

In GRE sequences, field gradients are used to compensate the spin dephasing. Initially, the application of a RF-pulse is played out along with the slice selection gradient. When the pulse is turned off, a phase encoding gradient is applied along the y-direction. Prior to data acquisition, a dephasing readout gradient is applied in the x-direction to induce a faster dephasing of the spins. During data acquisition, a readout gradient, opposite to the previous one, is applied to rephase the spins and one line of the k-space can then be read out, as it can be seen in figure 2.7. This process is repeated until a sufficient amount of data is acquired.

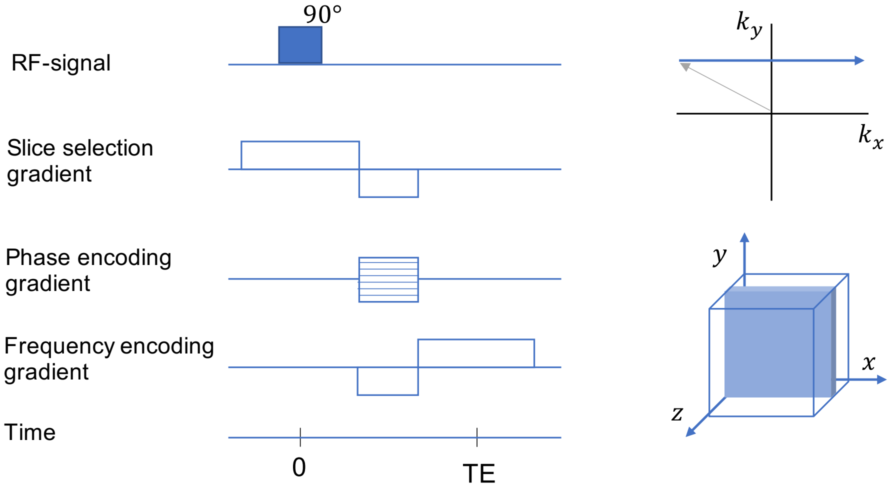

Figure 2.7 – On the left, the gradient-echo sequence diagram. A 90º pulse is applied for excitation. A negative frequency encoding gradient is applied for faster dephasing, followed by a positive frequency encoding gradient to rephase the spins. On the right, the first line of the k-space being filled (top) and the representation of a single slice being acquired (bottom).

GRE sequences only compensate for the dephasing caused by the gradient field. Therefore, magnetic susceptibility among different tissues and/or chemical shifts are not eliminated. These magnetic field inhomogeneities cause faster T_2^* relaxation than when compared with T_2 relaxation. In SE sequences, this dephasing is eliminated by the application of the 180 º RF-pulse [40].

Multiple echoes can be created at different TE by adding additional dephasing and rephasing gradients, originating what is referred to as mGRE, already introduced in section 1. The Quantitative T_2^* imagE (QUTE) sequence is an example of a mGRE sequence [15]. Particularly, the same k-space line is acquired for all the next slices rather than acquiring the next line of the same slice. This is translated in an effective repetition time, TR_{eff} given by

$$TR_{eff} = TR \cdot N_s \tag{2.11}$$

where TR corresponds to the repetition time, the time between the first pulse and the echo formation, and N_s is the number of slices. Additionally, the use of a bipolar read-out gradient (inverted polarity of the readout gradients) decreases the echo spacing, which results in a dense temporal sampling in the time domain. Figure 2.8 shows the QUTE sequence diagram.

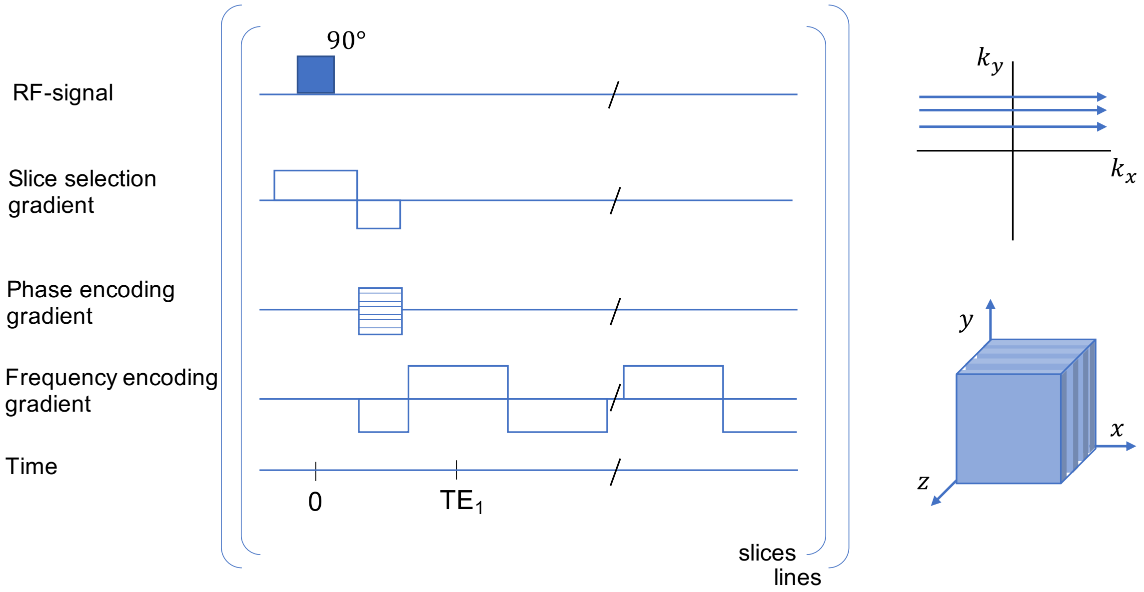

Figure 2.8 - On the left, the QUTE sequence diagram. A 90º pulse is applied to acquire the first line of the k-space. Another 90º pulse is applied to acquire the same line of the next slice. Dephasing and rephasing pulses are used such as in GRE sequences. On the right, the lines of the k-space being filled (top) and the representation of multiple slices being acquired (bottom).

Researchers often choose mGRE sequences over GRE sequences since it has the advantage of generating multiple images with different echoes of the same slice, which can then be used for quantitative analysis.

2.4 Noise in MRI

All physical experiments are corrupted by noise, an undesired interference or a random variation that affects the measurement. In MRI, the generated image is not created by pure MRI signal but instead, the measured signal S, results from a combination of the true underlying signal, s, corrupted with the unavoidable noise, n (see equation 2.12) [8]. Hence, noise can seriously affect the image quality and, therefore, influence not only qualitative but also quantitative results.

$$S = s + n \tag{2.12}$$

Thermal noise is the dominant source of noise in MR measurements arising from electrical fluctuations created by the random motion of electrons in a conductor. The primary sources of noise are generated by the coil, the sample and the electronics [41].

2.4.1 Noise distributions

Probability density functions can be used to describe the relative probability of noise to reach a given value [42]. MR noise is often classified as white noise, a sequence of statistically uncorrelated random variables, with constant intensity at all frequencies [43]. If every variable related to noise is normally distributed with zero mean and variance σ^2, the noise is referred to as Gaussian white noise and its probability density function (PDF) can be expressed as

$$f(x) = \frac{1}{2\pi\sigma^2} \exp\left(-\frac{x^2}{2\sigma^2}\right) \tag{2.13}$$

The real and imaginary part of the k-space are very often corrupted by zero mean Gaussian noise [42]. The Gaussian distribution of the noise is preserved when the complex Fourier transform is applied. When converted to a magnitude image (where nonlinear mapping methods are applied), the noise distribution is no longer Gaussian, but instead, it follows a Rician distribution [42] and becomes dependent of the signal [42].

$$f(x) = \frac{x}{\sigma^2} \exp\left(-\frac{x^2 + |s|^2}{2\sigma^2}\right) I_0\left(\frac{x|s|}{\sigma^2}\right) \tag{2.14}$$

Equation 2.14 is the PDF of a Rician distribution where I_0 is the modified zero-th order Bessel function of the first kind and $|s|$ corresponds to the magnitude of the underlying signal given by

$$|s| = \sqrt{Im_R^2 + Im_I^2} \tag{2.15}$$

being Im_R and Im_I the mean values of the real and imaginary part of data, respectively [44].

2.4.2 Signal-to-noise

The SNR is a way to characterise the degree of corruption of an image. It is usually calculated by dividing the average signal intensity in a ROI by the standard deviation of noise, that can be selected from a region with the same area outside of the tissue, where the signal is expected to be 0. SNR depends on several imaging parameters, where small changes can result in large effects in the image quality [41]. Equation 2.16 describes the SNR dependencies with the spatial resolution in the three directions $\Delta \boldsymbol{x}$, $\Delta \boldsymbol{y}$, $\Delta \boldsymbol{z}$, and the measurement time, T_M.

$$SNR \propto (\Delta \boldsymbol{x})(\Delta \boldsymbol{y})(\Delta \boldsymbol{z})\sqrt{T_M} \tag{2.16}$$

In case of high SNR (curves on the right side), the Rician distribution starts to approximate to a Gaussian distribution as it is shown in figure 2.9.

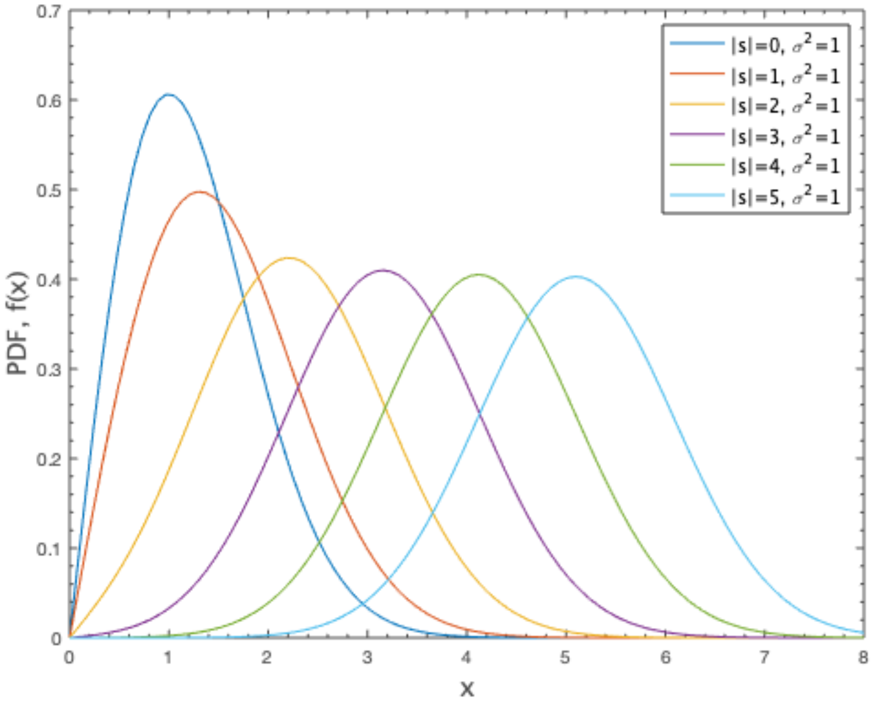

Figure 2.9 - Probability density functions of Rician distributed noise with different $|s|$ *values and fixed* $\sigma = 1$.

The image contrast is degraded in the presence of Rician noise. Rician noise is signal dependent noise, noise and, consequently, removing signal from noise is a hard task, particularly at low SNR. On the other hand, Gaussian noise is Additive and shall be reduced by denoising methods [45].

2.5 Denoising

Denoising is the process of removing noise to highlight the underlying signal. In image processing, it aims to increase image quality, and improve the accuracy and precision of the estimated values in quantitative imaging. It also improves the performance of post processing methods that are sensitive to noise or of signal fitting procedures which are ill-posed [7]. A fundamental problem is to remove the noise without losing relevant information of the image. To do so, several denoising methods can be used, whether linear or nonlinear [46]. In this thesis, the focus is placed on the Gaussian filter and the principal component analysis method.

In linear filters, the output pixel value is a linear combination of the initial value and those of neighbouring voxels [47]. Often, it causes image blurring due to the suppression of image details of the neighbouring voxels. An example of this is the mean filter. It consists of a sliding window spatial filter where the center voxels is replaced by the average of all voxel values in the window. Mean filters are considered convolution filters and therefore the shape and size of the window is based around a kernel [47].

Unlike linear filters, nonlinear filters tend to preserve the voxels representing edges and have been shown to have a better performance while removing noise [45].

2.5.1 Gaussian Filter

A Gaussian filter, much like the mean filter, accomplishes image denoising by means of a convolution operation between the image and a kernel, which represents the shape of a Gaussian function. The smoothing of a Gaussian filter is weighted so that the influence of a pixel decreases with its distance from the filter centre [48]. The Gaussian distribution in two dimensions has the form described by equation 2.17.

$$G(\boldsymbol{r},\sigma)=\frac{1}{\left(\sqrt{2\pi}\sigma\right)^{N}}\exp\left(-\frac{|\boldsymbol{r}|^{2}}{2\sigma^{2}}\right) \tag{2.17}$$

Where r is a vector containing the distance from the origin in each dimensional axis and N the dimension.

Particularly, Gaussian filters work on the assumption that noise follows a Gaussian distribution and thus, are more probable to fail when the noise of the MR image follows a Rician distribution [44].

2.5.2 Principal component analysis

Principal component analysis (PCA) is a nonlinear mathematical technique that uses an orthogonal transform to find a linear combination of variables such that the maximum variance in the data is extracted from those variables [49].

The input features that consist of a large number of correlated variables are transformed into a new lower dimension feature space. The basis of the new feature space is formed by the coordinate vectors referred to as the principal components. The first component has the higher magnitude, as it explains the highest variance in the data. The second component has the second largest variance within the dataset and is orthogonal to the first component. The succeeding components account for the largest possible variance in succeeding order, always orthogonal to each other.

A 2D system is represented in figure 2.10, where the dataset shows to have a structured distribution. The greatest variability is found along the first component (red), whereas the second component (green) is orthogonal to the first component and explains the spread of the data around the first component.

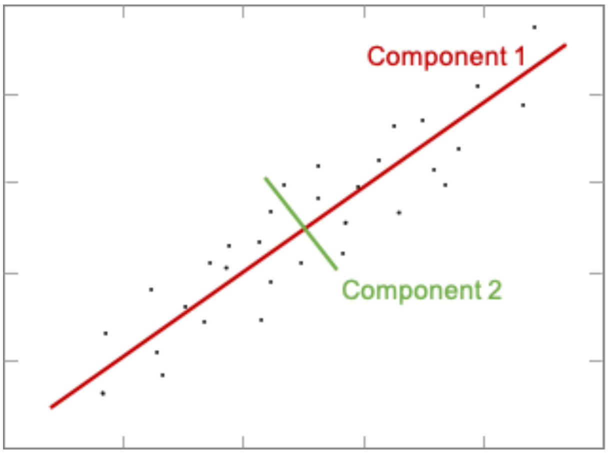

Figure 2.10 - Principal component analysis of a 2D system.

In practice, PCA requires the computation of the eigenvalues and eigenvectors of the covariance matrix. If X denotes the centered (zero mean) data matrix of $m \times n$ size, where m represents the number of datasets and n the number of variables, the covariance matrix, C, of $n \times n$ size, is given by equation 2.18.

$$C = \frac{X^T X}{n-1} \tag{2.18}$$

The covariance matrix is symmetric and thus it can be diagonalized according to equation 2.19,

$$\frac{X^T X}{n-1} = VLV^T \tag{2.19}$$

where V is a matrix containing the eigenvectors and L is diagonal matrix with the eigenvalues as entries.

On the other hand, the covariance matrix of X can also be constructed by using single value decomposition (SVD) as described in equation 2.20

$$X = USV^T \tag{2.20}$$

where U and V are unitary matrixes of size $m \times m$ and $n \times n$, respectively, and S is a diagonal matrix that contains the variances of each dimension of the size $m \times n$. The relationship in equation 2.21 can be obtained from the following decomposition

$$C = \frac{1}{n-1} X^T X = \frac{1}{n-1} VSU^T USV^T = V \frac{S^2}{n-1} V^T \tag{2.21}$$

where the columns of U and the rows of V^T contain the left and the right singular vectors. The singular values of the matrix S are ordered by high to low sorting in such a way that the highest singular value is in the upper left index of S [50], [51].

PCA advantages and limitations

PCA can deal with complex data sets using analytical solutions from linear algebra, being easy to implement and computationally efficient [52]. Removing correlated features is the main advantage of PCA since running algorithms on all the features reduces its performance.

Actually, unlike PCA, many other methods take into account the values of adjacent voxels, and the new value for each voxel will be influenced by the neighbours, depending on the window size chosen [53]. These methods are prejudicial to high resolution since in neighbouring voxels where is possible to see a clear distinction between tissues, the new values should not be dependent on the adjacent voxels. PCA is thereby an advantageous method, because it allows the separation of the noise from the signal decay.

However, PCA-based denoising requires the definition of the number of principal components that will originate the new denoised signal matrix. Once this threshold is defined by the user, it is not possible to predict how biased the generated data will be [54].

2.6 Field inhomogeneities

In SE-based MR experiments, the magnetic field inhomogeneities are removed with the application of the 180º pulse. In mGRE sequences however, a high uniformity of the external magnetic field is required to achieve accurate estimations of the T_2* relaxation time.

In fact, the field inhomogeneities can be classified in three categories according to their length scales: (1) *microscopic field inhomogeneities,* associated with irreversible T_2 decay caused by superparamagnetic iron oxide (SPIO) particles, on a molecular level; (2) *mesoscopic field inhomogeneities,* associated with the heterogeneity in the distribution of SPIO particles in the compartmentalized voxel, on a sub-voxel level; (3) *macroscopic field inhomogeneities,* associated with inhomogeneous external magnetic fields and large scales susceptibility changes between air-tissue interfaces [14]. In this work, we only concern ourselves with the latter.

2.6.1 Sinc modulation of the FID

The effects of macroscopic field inhomogeneities in the FID are extensively described in [13], and will be briefly explained in this section. Assuming that the B_0 field varies linearly across a voxel, it is shown that, in the presence of weak B_0 inhomogeneities, a classic monoexponentially decay is observed (solid line in figure 2.11), while, in moderate B_0 inhomogeneous field (dashed line in figure 2.11), the FID is decaying faster and small deviations from the exponential curve can be seen. Higher inhomogeneous B_0 fields (dotted line in figure 2.11) lead to bigger changes in the decay curve, leading to a sinc modulation of the curve.

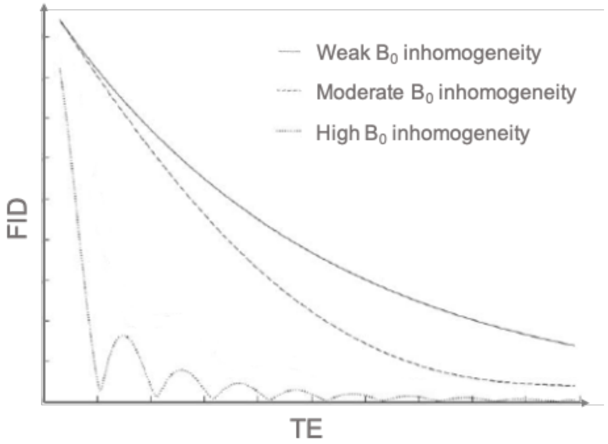

Figure 2.11 - FID amplitude curves showing the influence of different B_0 inhomogeneities strengths in the signal (adapted from [13]).

Macroscopic field inhomogeneities are undesirable because the associated dephasing does not provide true physiologic or pathophysiologic information. In this sense, magnetic field inhomogeneities corrections methods are likely to improve the detection of small lesion changes.

2.6.2 Voxel spread function theory

Both mGRE phase and magnitude images can be used to calculate the contribution of field inhomogeneities ΔB_0. In their work, Yablonsky et al [55] reviewed the basic theory of MRI signal formation and developed a voxel spread function (VSF) method to correct the signal behaviour in the presence of macroscopic magnetic field inhomogeneities.

The MR signal from a voxel detected by a mGRE sequence can be written as

$$S_n(\mathrm{TE}) = s_0 \cdot \exp\left(-\frac{\mathrm{TE}}{\mathrm{T}_2^*} + i \cdot \gamma b_n \cdot \mathrm{TE}\right) \qquad 2.22$$

where s_0 is the expected signal in the absence of macroscopic magnetic field inhomogeneities, and b_n corresponds to the local magnetic field.

However, the actual signal during the readout period t, in the presence of inhomogeneous magnetic field $b(\mathbf{r})$, can be represented as

$$\tilde{S}(\mathbf{k}; \mathrm{TE}) = \int d\mathbf{r} \cdot \rho(\mathbf{r}; \mathrm{TE}) \cdot \exp[-2\pi i \mathbf{k}\mathbf{r} + i\gamma b(\mathbf{r}) \cdot (\mathrm{TE} + \mathrm{t}) + i\varphi_0(\mathbf{r})] \qquad 2.23$$

where $\rho(\mathbf{r}; \mathrm{TE})$ is the spin density, $\mathbf{r}$ is the position of the voxel, t is the difference between the time after the initial RF pulse and TE and $\varphi_0(\mathbf{r})$ corresponds to the signal phase at TE = 0. Each data point in k-space is a continuous Fourier transform of the signal in equation 2.23 and is defined as

$$2\pi k_x = \gamma\, G_x\, t_x; \qquad 2\pi k_y = \gamma\, G_y\, t_y \qquad 2\pi k_z = \gamma\, G_z\, t \qquad 2.24$$

Here, t_x and t_y represent the duration of the gradients G_x and G_y of the phase encoding directions, while G_z represents the read-out gradient.

The MR image is therefore reconstructed by the discrete inverse Fourier transform of k-space data as

$$S_n(\mathrm{TE}) = \frac{1}{N} \cdot \sum_k \tilde{S}(\mathbf{k}; \mathrm{TE}) \cdot \exp[2\pi i \mathbf{k}\mathbf{r}_n] \qquad 2.25$$

The VSF gives the contribution of the neighbour voxel m to the voxel n, η_{nm}. Accordingly, the final signal from the voxel n is the sum of signals contributed by the neighbouring voxels and can be represented as

$$S_n(\mathrm{TE}) = \frac{1}{N} \cdot \sum_m \sigma_m(\mathrm{TE}) \cdot \exp\left(i\gamma b_m \mathrm{T}E + i\varphi_{0,\mathrm{m}}\right) \cdot \eta_{nm} \qquad 2.26$$

where $\sigma_m(\mathrm{TE})$ is the ideal signal from the m-th voxel, resulting from the product of the voxel volume and the spin density

$$\sigma_m(\mathrm{TE}) = V \cdot \rho_m(\mathrm{TE}) \qquad 2.27$$

2.7 T_2* mapping

T_2*-weighted imaging allows the depiction of paramagnetic particles contained in the blood cells, such as oxygenated haemoglobin, which contribute to a signal loss, usually associated with the existence of pathologic conditions [40]. Several lesions, including arteriovenous malformations, haemorrhage in tumours, thrombosed aneurysm, among others, are described in a study published by Chavhan et al. [40] to be visible in T_2*-weighted images. Also, they can be useful to distinguish between schwannomas and other similar brain tumours, since microhaemorrhages are often found in schwannomas [27].

2.7.1 Mono-exponential relaxometry

Although voxels are often inhomogeneous, for many years, mono-exponential fitting of relaxation parameters was used to quantify voxel information of brain pathologies [22]. Accordingly, the MR signal described in equation 2.22 is more often found in its simple form, that is given by

$$S(\mathrm{TE}) = s_0 \cdot \exp\left(-\frac{\mathrm{TE}}{\mathrm{T}_2^*}\right) \qquad 2.28$$

In 2013, an investigation conducted by Oros-Peusquens et al. [56], studied relaxation properties in five patients with glioblastomas mainly located in white matter. The mean T_2* for tumour tissues (69.8 ms) was found to be higher than the mean values for normal white and grey matter (52.3 ms and 52.1 ms, respectively). Four years later, a study aiming to evaluate a multiparametric and multi-modality imaging protocol applied to brain tumours [8] where PCA was applied for noise reduction, reported a mean T_2* value of 70.83 ms for brain tumours and 50.94 ms and 52.01 ms for white and grey matter, respectively. Additionally, the oedema regions were also studied and the mean T_2* value was found to be 71.40 ms.

Both studies were performed in 3T scanners. Furthermore, another report [49] revealed that the bulk values of T_2* in white and grey matter were found to decrease with the field increase. The centroid of the Gaussian distributions which best corresponds to the WM T_2* distributions was found to be 66.5, 48.8 and 39.8 ms at 1.5, 3 and 4 T, respectively. The GM T_2* distribution revealed that the centroid of the Gaussian distributions was 71.5, 49.3 and 41.5 ms at 1.5, 3 and 4 T, respectively.

2.7.2 Multi-exponential relaxometry

The voxel size is very large relative to the microscopic boundaries and volumes it encloses. This means that a voxel will often contain of different types of tissue, each of which with distinct relaxation properties. Discussions around how biased the values obtained with mono-exponential fits are have been reported [30] and a transition to multi-exponential fits is notable as of recently. In multi-exponential relaxometry, equation 2.28 should then be written as a sum of exponential decays as follows

$$S(TE) = \sum_{j=1}^{N} s_{0,j} \exp\left(-\frac{TE}{T_{2,j}^{*}}\right) \qquad 2.29$$

As described in section 2.1, the water found within the voxel can belong to four different pools. In the particular case of white matter, the pools can result from intracellular water, extracellular water and water trapped between myelin sheaths. Multi-exponential relaxometry can then be used to calculate the fraction of water of the different pools when the relaxation times are distinguishable. However, the relaxation times of the intracellular and extracellular water are similar [7], [57], and thus white matter is more commonly described with two distinct pools: myelin water and intra/extracellular water.

Substantial and numerous contributions have been done by Whittall and MacKay in the field of multi-exponential relaxometry, introducing a NNLS approach to T_2 relaxometry [6], [9], [10], [57]. In 1997, Whittall, MacKay and Graeb [10], used NNLS to decompose the analogous signal for T_2 relaxometry in equation 2.31, and the following was found: i) water compartmentalized in myelin sheath has T_2 between 10 and 55 ms; ii) water in cytoplasmic and extracellular spaces have T_2 between 70 and 95 ms; iii) cerebrospinal fluid has T_2 greater than 1s [10].

However, only recently, a paper regarding the distribution of T_2 components in three different human brain tumours has been published [58]. Aiming to evaluate different grades of brain tumours based on a quantitative assessment of T_2 relaxation through means of NNLS, this work reported specific peaks for glioblastoma, oligodendroglioma and meningioma. In the same study, the T_2 distribution profiles in glioblastomas were found to be heterogeneous, with broad T_2 peaks. In oligodendrogliomas, a T_2 peak between 278 ms and 479 ms was estimated, while for meningioma, the majority of the signal was found at 115-124 ms and a smaller component at 466-511 ms. Meningioma-associated oedema was identified to be distinct from the tumour profile and long T_2 relaxation times were found, likely due to the increased water content (see more in section 2.8) in the extracellular space of the oedema area. The main limitation of this study was that the number of patients used was not enough to establish a quantitative profile for each type of tumour, since each tumour has independent characteristics due to the heterogenous nature. The lack of studies regarding multi-exponential T_2* relaxometry is noticeable and therefore, literature values are scarce. In 2018, estimated T_2* values with a NNLS algorithm were published for 12 volunteers in a 3T scanner by Alonso et al. [59]. They reported an average geometric mean T_2* (gmT_2*)

of 51, 53 and 66 ms for WM, deep GM and cortical GM, respectively. To our knowledge, no multi-exponential relaxometry model was used to describe T2* values in brain tumours.

2.8 Water mapping

Water is highly regulated in the healthy human brain [8]. Several pathologies can affect the water content proving its direct physiological meaning [8]. It can be used to measure oedema, that is by definition an increase of the water content, or other kind of diseases such as stroke, multiple sclerosis, alcoholism, among others [15].

Water maps use percentage to define the amount of water in the tissue, 0% for no water and 100% for pure water. The water content is directly proportional to M_0 in the assumptions that the MR visible protons belong only to the brain water and that all water particles can be detected [60]. Yet, M_0 needs to be extrapolated from a time series such as the ones originated from mGRE sequences (see more in section 3.4.1).

In the literature, water content in brain tumours has been found to be similar to the value for normal grey matter tissue (84.5% in tumour and 84.3% in grey matter), even though the tumours were mainly located in white matter [56]. In a report published in 2017 [8], the similarity in the water content of tumour and grey matter tissue was confirmed. The mean water content was reported to be 84% and 83% for tumour and normal grey matter tissue, respectively. Additionally, the mean white matter value was found to be 69% and in the oedema regions 79%.

3. Materials and Methods

3.1 Data acquisition

All experiments were conducted using a commercial 3T Siemens Tim Trio MR system with an integrated Siemens custom-built BrainPET insert of high resolution (approximately 3 mm). The PET detector consists of a 12 × 12 matrix of volume 2.5 × 2.5 × 20 mm^3 lutetium oxyorthosilicate detectors coupled to avalanche photodiodes. The BrainPET insert is a compact cylinder with an inner diameter of 36 cm, which houses the MR head coil. A birdcage coil was used for radiofrequency excitation, whereas an 8-element receiver coil was used for signal reception. Before the MR acquisitions, three-dimensional (3D) shimming was performed, and the shim values were applied to all subsequent scans. The hybrid scanner is equipped with gradients of maximum strength of 40 mT/m per axis. The scanner is located at the Institute for Neurosciences and Medicine-4, Research Centre Jülich, Germany.

For this study, 33 patients with suspicion of a brain tumour or recurrence of a previously treated tumour were recruited. Some of the patients had brain surgery for tumour removal and others received radiotherapy, chemotherapy, or anti-cancer medication. Out of these 33 patients (mean age 50, range 27-76 years old), tumours were identified either by histology or supported by the results of dynamic PET. Data acquisitions for this project were conducted between 2014 and 2016 and therefore all grades were according to the guidelines suggested by the 2007 WHO classification of tumours of the central nervous system [27]. Written informed consent was obtained from all patients prior to scanning.

The patients were scanned with a QUTE sequence where the acquisition parameters were $T_R = 5000$ ms, $TE_1 = 3.34$ ms, $\Delta TE = 2.85$ ms, $\alpha = 25^o$, FOV of 144×210 mm^2, acquisition matrix of 192 × 132, and a resolution of $1 \times 1 \times 1.5$ mm^3. A set of 64 slices and 26 echoes were acquired with a slice gap of 0.75 mm. Partial Fourier acquisition was used with a factor of 0.75 to shorten the overall scan time. The total acquisition time was 4 min 12 s.

3.2 Masks

For each patient, regions of interest were analysed based on masks. WM, GM, and CSF probability maps were computed with SPM12 [61], a MATLAB toolbox often used in neuroimaging for segmentation of the brain [62]. A robust segmentation is achieved with a Gaussian mixture model and with a-priori knowledge of the spatial probability of each normal tissue region. Additionally, it corrects for smooth intensity variations [62].

The hemisphere contralateral to the tumour was manually selected and only voxels with a probability of belonging to that region equal to or higher than 98% were considered for generating the tissue-specific masks. The generated brain masks are the result of the sum of the WM, GM, and CSF masks.

Tumour and oedema masks were available and are mutually exclusive. The tumour masks were obtained from PET by thresholding and the oedema masks were obtained semi-automatically using MP-RAGE (pre- and post-contrast agent administration), SPACE and FLAIR information. Not all of the 33 patients presented oedema regions.

A selected slice of the QUTE data of a representative patient is shown in figure 3.1, as well as its respective masks of tumour, oedema, WM, GM and CSF.

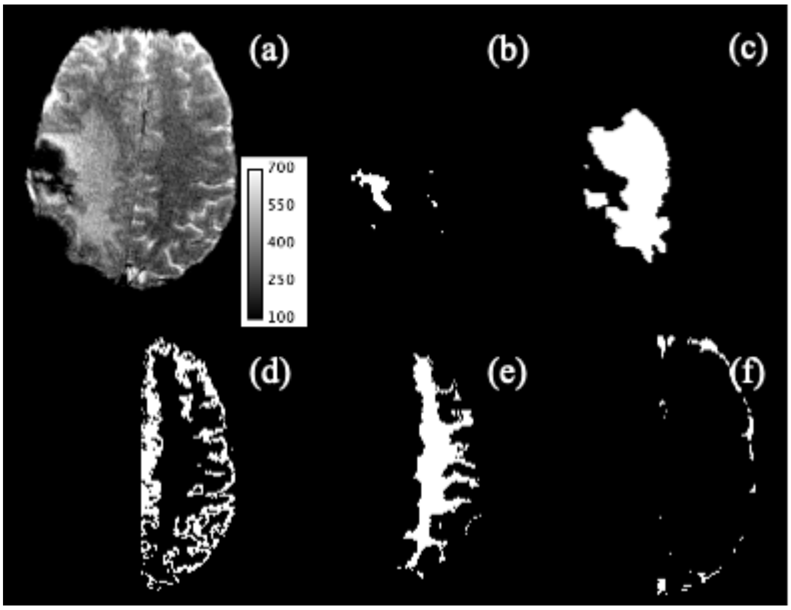

Figure 3.1 - Representation of a selected slice of the original magnitude data (a), tumour mask (b), oedema mask (c), GM mask (d), WM mask (e) and CSF mask of a selected patient. Because the tumour is located in the left hemisphere, only the right hemisphere of the WM, GM and CSF masks is used.

The QUTE data was processed as schematically shown in Figure 3.1 and will be explained in detail bellow. Both mono- and multi-exponential models were applied for all original QUTE datasets and to all processed data with the different noise reduction and inhomogeneities correction methods.

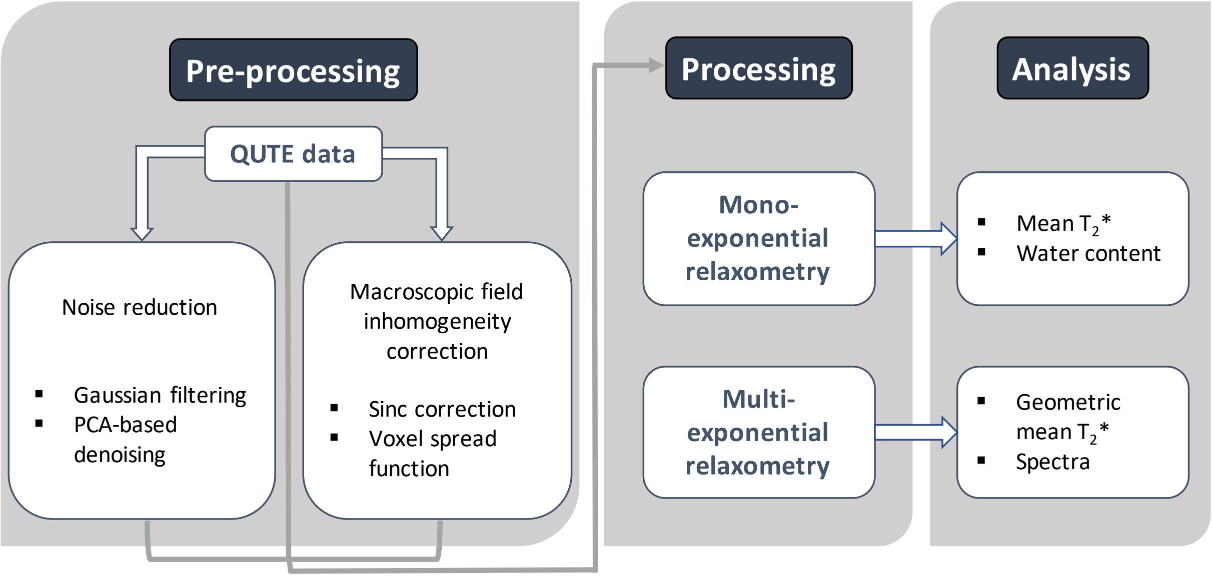

Figure 3.2 - Diagram summarising the pre-processing, processing and analysis steps carried out in this thesis.

3.3 Pre-processing

3.3.1 Noise reduction

This project made used of two distinct noise reduction approaches that were applied separately to the QUTE data. The Gaussian filter was performed with ImageJ [63] and PCA-based denoising was performed with Python 3.7 [64].

Gaussian filtering

A 3D gaussian filter was used to suppress the small fluctuations at individual voxels. This is accomplished by replacing each voxel with a weighted average of neighbouring voxels, defined by the designed kernel. The standard deviation, σ in equation 2.17, plays an important role in its behaviour. In probabilistic terms, the values located in $\pm\,\sigma$ from the mean describe 68% of the set, while values located in $\pm\,2\sigma$ describe 95% and $\pm\,3\sigma$ describe 99.7%. For this work, a factor of 0.4 of the voxel sizes was used, in all directions.

PCA-based denoising

In mGRE sequences, the produced data has one temporal dimension, that defines the respective signal, and other three spatial dimensions. Usually, PCA algorithms take advantage of this fact and the denoising occurs in the temporal dimension, while the spatial dimension is used to estimate the transform matrix.

We assumed that equation 2.20 can explain the corruption of the true signal matrix, X', by noise, Z, as

$$X' + Z = USV^T \tag{3.1}$$

and it would then be doable to extract X' by keeping only the first values of S, which are the most relevant the signal, depending on a pre-defined threshold.

A fundamental question is then, how many components we should keep when defining the threshold. We used the minimum variance filter proposed by Bydder and Du [65] to perform a soft thresholding by combining all the eigenvectors using weights w_k given by:

$$w_k = \sqrt{1 - \frac{\sigma_{noise}^2}{\sigma_k^2}} \tag{3.2}$$

with σ_{noise} a singular value corresponding to noise only (the noise standard deviation) and σ_k the k-th singular value (signal standard deviation of all k components).

The signal and noise components in the matrix S were determined based on the weights given by w_k, and the signal was then reconstructed using

$$X_{new} = US_{new}V^T \tag{3.3}$$

where the smaller eigenvalues in S are close to a zero weight in S_{new}, while the higher eigenvalues continue to describe the signal and dominated the reconstructed signal X_{new}.

3.3.2 Macroscopic field inhomogeneity correction

The consideration and correction of susceptibility-induced field distortions were carried out by two different approaches applied separately to the QUTE data. MATLAB 2019b [66] was used to pre-process the data in both methods.

Sinc correction

The behaviour of the signal intensity as a function of echo time is often described as previously shown in equation 2.30. However, in the presence of inhomogeneities in the applied magnetic field, the signal decay is influenced, and other factors need to be considered.

A sinc modulation is induced by the cross-slice dephasing, as demonstrated in [14]. In the presence of linear ΔB_0, the behaviour of the signal can then be rewritten as follow

$$S(TE) = S_0 \cdot \exp\left(-\frac{TE}{T_2^*}\right) \cdot sinc\left(\frac{\gamma}{2} \cdot g_z \cdot z \cdot TE\right) \qquad 3.4$$

where γ is the gyromagnetic ratio of the proton, and g_z is the background gradient in the z-direction. The sinc correction method calculates the sinc term in equation 3.4 and divides the original signal with the sinc fit to obtain the corrected data (S_{corr}), as described in equation 3.5.

$$S_{corr}(TE) = \frac{S(TE)}{sinc\left(\frac{\gamma}{2} \cdot g_z \cdot z \cdot TE\right)} \qquad 3.5$$

Because the background field inhomogeneities depend also on the subject, the background gradients were determined individually from the acquired phase images. In each spatial direction i, the gradients were calculated according to

$$g_i = \frac{1}{N} \sum_{n=1}^{N} \frac{\Delta\varphi_{i,n}}{\gamma \Delta x_i TE_n} \qquad 3.6$$

where the phase difference in the i-th direction at the n-th echo time TE_n is represented by $\Delta\varphi_{i,n}$ and the voxel size is represented as Δx_i.

As shown in [13], the shape of the signal intensity changes significantly after a certain echo time is exceeded. To avoid including the contaminated signal in the calculation of the gradient maps, only echoes that had an intensity of at least 0.8 the intensity of the first echo were used. Additionally, the critical echo time (maximum echo time without signal dropout due to in-plane gradients in 2D imaging) used in equation 3.5 and for the T_2* fitting, was set according to the minimum of three effects. First, a factor of 0.8 was applied to the gradient in the frequency encoding direction. Second, a factor equal to the partial Fourier parameter (0.75) was applied to the gradient in the phase encoding direction. Third, a factor of 0.9 was applied to the maximum echo time to account for possible errors when calculating the gradients. Therefore, the number of echo times used for the calculation of the background gradients (equation 3.6) is different from the number of the echo times used for generating the corrected map and for the T_2* fitting (equation 3.5) [8], [67].

Voxel spread function

The VSF method uses both magnitude and phase of mGRE data as introduced in section 2.6.2.

As equation 2.26 defines the relationship between the ideal signal and the inhomogeneities contributions, the VSF calculates $S_n(\mathrm{TE})$, by solving the following equation

$$S_n(\mathrm{TE}) = \sigma_n(\mathrm{TE}) \cdot F_n(\mathrm{TE}) \qquad 3.7$$

Once solving equation 2.26 involves inversion of large matrices which is computationally intensive, this method assumes that neighbouring signals have similar decay rates, as follows

$$\sigma_m(\mathrm{TE}) = \sigma_n(\mathrm{TE}) \cdot \frac{|S_m(0)|}{|S_n(0)|} \qquad 3.8$$

Which leads to,

$$F_n^{[1]}(\mathrm{TE}) = \frac{1}{|S_n(0)|} \cdot \sum_m |S_m(0)| \cdot \exp\left(i\gamma b_m TE + i\varphi_{0,m}\right) \cdot \eta_{nm} \qquad 3.9$$

However, the neighbouring voxels at the borders of two different environments can have different decay rates. And so,

$$\sigma_m(\mathrm{TE}) = \sigma_n(\mathrm{TE}) \cdot \frac{|S_m(0)| \cdot \exp\left(-\frac{\mathrm{TE}}{T_{2,m}^*}\right)}{|S_n(0)| \cdot \exp\left(-\frac{\mathrm{TE}}{T_{2,n}^*}\right)} \qquad 3.10$$

is a closer estimation of the ideal signal and $F_n(\mathrm{TE})$ can be rewritten as

$$F_n^{[2]}(\mathrm{TE}) = \frac{1}{|S_n(0)| \cdot \exp\left(-\frac{\mathrm{TE}}{T_{2,n}^*}\right)} \cdot \sum_m |S_m(0)| \cdot \exp\left(-\frac{\mathrm{TE}}{T_{2,m}^*} + i\gamma b_m \mathrm{TE} + i\varphi_{0,m}\right) \cdot \eta_{nm} \qquad 3.11$$

After calculating the F-function, the corrected signals $\sigma_n^{[1]}$ and $\sigma_n^{[2]}$ were obtained by dividing $F_n^{[1]}$ and $F_n^{[2]}$, respectively, in equation 3.7.

The VSF algorithm allows the user to choose the number of neighbouring voxels that will contribute to the final signal. In this thesis, we used the nearest neighbouring voxels in both transversal directions (four voxels around the centered voxel of the same slice).

3.4 Processing

3.4.1 Mono-exponential decay model

The toolbox Quantitative Analysis Tool for MRI (QUanTooM) developed by the host institution (Institute of Neuroscience and Medicine 4 - INM4), was used to compute the water, and T_2* maps.

The framework is fully automatic and the processing steps that lead to the computed water and T_2* maps (long TR method) are showed in figure 3.3.

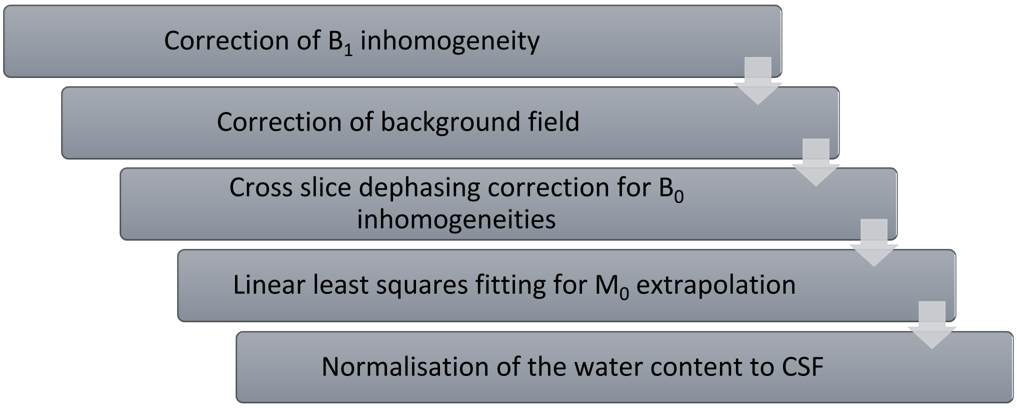

Figure 3.3 - Processing steps of the long TR method for water mapping.

The effects induced by the excitation field (B_1^+) and the received field (B_1^-) cause non-uniformity intensity that can be written as

$$S(TE) = M_0 \exp\left(-\frac{TE}{T_2^*}\right) \sin(B_1^+ \alpha_{nom})\, B_1^- \tag{3.12}$$

with α_{nom} the nominal flip angle. The B_1 bias field field was computed using SPM12 allowing the correction of B_1 inhomogeneities as follow

$$|S_{corr}(TE)| = \frac{|S(TE)|}{\sin(B_1^+ \alpha_{nom}) B_1^-} \tag{3.13}$$

The background phase was removed with a homodyne filter, applied in k-space by using a 2D-Hann window, to separate the local phase from the background phase. The cross-slice dephasing correction follows the same principle as in the sinc correction method. Note that this step was not performed on data already processed with the sinc correction or with the VSF.

The curve fitting was performed by iterating the tissue parameters with the aim to minimise the distance to a series of data points. For M_0 extrapolation, the model was linearised by transforming it into the logarithmic space (equations 3.14 and 3.15).

$$S_{corr}(TE) = M_0 \exp\left(-\frac{TE}{T_2^*}\right) \qquad 3.14$$

$$\rightarrow \log\left(S_{corr}(TE)\right) = \log\left(M_0\right) - \frac{TE}{T_2^*} \qquad 3.15$$

The original phase maps that are acquired from the scanner results from the background phase (w_{BG}) and from the local changing phases of different regions of the brain (w_{local}). To include the phase maps, equation 3.14 was written as

$$S(TE) = M_0 \exp\left(-\left(\frac{1}{T_2^*} - i(w_{local} + w_{BG})\right) TE\right) \qquad 3.16$$

Assuming that all water molecules in the brain are detected by the scanner, M_0 is directly proportional to the water content. Therefore, after calculating M_0 by fitting the exponential function, the water content is normalised to the CSF values, since CSF is assumed to be 100% water. This gives a percentage from 0 to 100% to the water content.

3.4.2 Multi-exponential decay model

To avoid long processing times, one slice from each patient containing the tumour region was visually selected based on the tumour mask.

In this thesis, with the aim of characterising the T_2* distributions within each voxel, we make use of NNLS, which will be explained in the following section. First, to characterise the measured signal y_i, the NNLS algorithm defines a matrix A with M elements of discrete T_{2j}^* relaxation decay curves as follows

$$y_i = \sum_{j=1}^{M} s_j \exp\left(-\frac{t_i}{T_{2j}^*}\right) = \sum_{j=1}^{M} A_{ij} s_j, \qquad i = 1,2,\ldots,N. \qquad 3.17$$

where s_j is the amplitude corresponding to the T_{2j}^* relaxation time, and *N* represents the total number of data points measured at t_i time of data point *i*. The algorithm aims to find a discrete solution of s_j which will minimise the least squares misfit according to

$$\text{minimise } \|\mathbf{A} \cdot \mathrm{x} - \mathbf{y}\| \text{ subject to } x \geq 0. \qquad 3.18$$

However, the number of data points *i* is smaller than the number of elements j in the basis set M, resulting in equation 3.18 describing an ill-posed problem. Also, because noise always remains in the data, Tikhonov regularisation was proposed to overcome this problem and provide a more stable and realistic model by minimising the equation after introducing a regularisation parameter, λ, in equation 3.18.

$$\text{minimise } \left\|\mathbf{A} \cdot \mathrm{x} - \mathbf{y} + \lambda\, \boldsymbol{x}^{\mathbf{2}}\right\| \text{ subject to } x \geq 0. \qquad 3.19$$

The regularised NNLS algorithm then tests a range of λ values until one is found to satisfy the predefined convergence conditions. Equation 3.19 shows that the cost of the norm of the solution is influenced by λ, so that the higher the value of λ, the larger the misfit will be, resulting in a smoother amplitude distribution.

The regularised NNLS requires the user to insert three parameters: the sample interval, a range of regularisation values, and the interval where the χ^2 should lay on. The T_2* space was defined with a linearly spaced vector between 5 and 300 ms, consisting of 295 steps. The solution was regularised iteratively, where each iteration used an increasingly higher value of λ. The regularisation parameters used were determined over a logarithmically spaced vector from -2 to 0.1, with 20 steps. The iterations were stopped when the following constraint was met $1.005 \cdot \chi^2_{min} \leq \chi^2 \leq 1.010 \cdot \chi^2_{min}$. If the maximal χ^2 was exceed, a λ between the two previous ones was used for the next iteration. The choice of the different parameters was based on the literature (T_2*), and by looking at how the L-curves and the produced maps were being affected (see more in section 4.2.2).

L-curve

The L-curve method of determining the regularisation coefficient λ, uses a log-log plot (see equation 3.20) of the regularised solution norm versus the corresponding residual norm, that allows to determine the optimal regularisation parameter [68].

$$(\log(\|Ax_\lambda - y\|_2) , \log (\|x_\lambda\|_2)) \qquad 3.20$$

The curve often presents a L-shape with an initial flat part, and a steep part. The logarithmic scale emphasises the difference between both parts and the optimal regularised solution should lie near the corner of the curve. The optimal regularisation can be found in the point of maximum curvature, when plotting the curvature of the L-curve as a function of λ.

The curvature k, was derived as follow

$$\eta = \|x_\lambda\|_2^2 \qquad \rho = \|Ax_\lambda - y\|_2^2 \qquad 3.21$$

$$\hat{\eta} = \log \eta \qquad \hat{\rho} = \log \rho \qquad 3.22$$

$$\mathrm{k} = 2\,\frac{\hat{\rho}'\,\hat{\eta}'' - \hat{\rho}''\,\hat{\eta}'}{((\hat{\rho}')^2 + (\hat{\eta}')^2)^{3/2}} \qquad 3.23$$

where $\hat{\rho}'$,$\hat{\rho}''$, $\hat{\eta}'$, $\hat{\eta}''$are the first and second derivatives of $\hat{\eta}$ and $\hat{\rho}$ with respect to λ, respectively [68].

3.5 Analysis

While in mono-exponential relaxometry the mean T_2* corresponds to the arithmetic mean T_2*, in multi-exponential models, the gmT_2* is the mean T_2* on a logarithmic scale [59] and was calculated according to equation 3.24.

$$\mathrm{gmT}_2^* = \exp\left[\sum_{j=M_{min}}^{M_{max}} s_j \log\left(T_{2,j}^*\right) / \sum_{j=M_{min}}^{M_{max}} s_j\right] \tag{3.24}$$

For an overall analysis, the WM, GM, CSF, tumour and oedema masks were used to calculate the mean T_2* and the gmT_2*, in each region.

For each patient, small regions inside the PET-based tumour mask were manually drawn to study multiple components in brain tumours and assess heterogeneity. These masks were used to plot the T_2* distribution and to calculate the gmT_2*, of each small ROI. Comparison with the corresponding normal appearing tissue was done by selecting a region with similar area into the contralateral side of the drawn tumour region. When not possible, the normal appearing mask was drawn next to the tumour, such as in patients where the tumour is distributed for both hemispheres.

Statistical analyses were performed with IBM SPSS Statictics [69]. We compared statistically significant differences between (1) the mean T_2* in different regions of interest (ROIs), (2) the mean T_2* calculated with the different correction methods, (3) the gmT_2* in different ROIs, (4) the gmT_2* calculated with the different correction methods, (5) the mean T_2* and the gmT_2* (mono- vs multi-exponential models) and (6) the T_2* distributions obtained in the selected tumour regions and the corresponding normal appearing regions. To do so, different statistical tests were applied according to the goal of the comparison, with a significance level of 0.05.

4. Results and Discussion

This chapter is divided in three main parts in which the results and discussion on *in vivo* data are presented. In the first part, a qualitative comparison of the obtained maps is performed for the different correction methods. Here, differences between the used methods are presented, with respect to the SNR and to the signal decay. In the second part, quantitative T_2* analysis of the different ROIs can be found for mono and multi-exponential relaxometry as well as the study of specific T_2* components in brain tumours. In the third part, water content values are presented and correlated with T_2*.

4.1 MRI signal

4.1.1 Noise reduction

In practice, no background truth, i.e., no original noise-free image is available. Therefore, the performance of the denoising techniques is evaluated based on the SNR. In this study, the SNR was calculated for all 26 echoes in an apparently healthy region. Figure 4.1 shows the SNR improvement for the first echo of both denoising methods over the non-denoised (QUTE) data, demonstrated on a representative axial slice. Gaussian filtered data are shown to have high noise reduction effects when compared to the original data maps, which is accompanied by the higher SNR value. The PCA-based denoised data maps, also shown to have visible noise reduction effects but appear to be less blurry than the Gaussian filtered data maps.

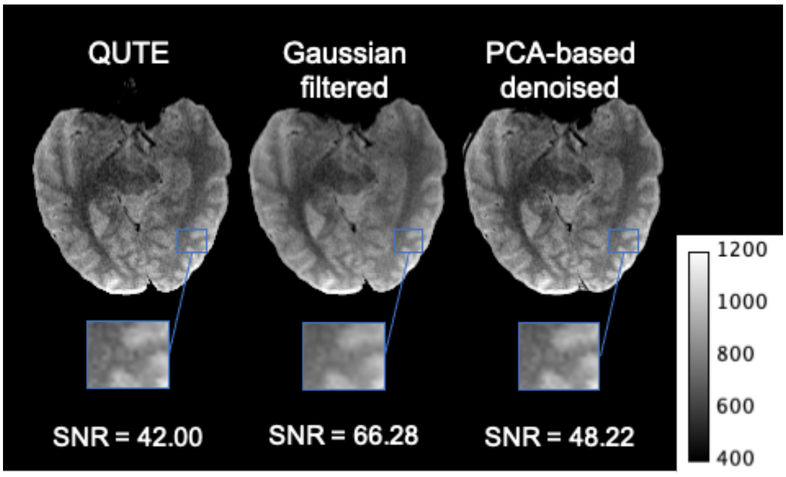

Figure 4.1 - Visual effects of the noise reduction methods on the first echo of a selected slice.

Figure 4.2 presents the calculated SNR for each echo time of the original and both denoised data for the selected region presented in figure 4.1. It can be observed that both Gaussian filtered data and PCA-based denoised data have higher SNR across the echoes, when compared to the QUTE data. Particularly, PCA-based denoised data shows higher SNR gains for the last echoes.

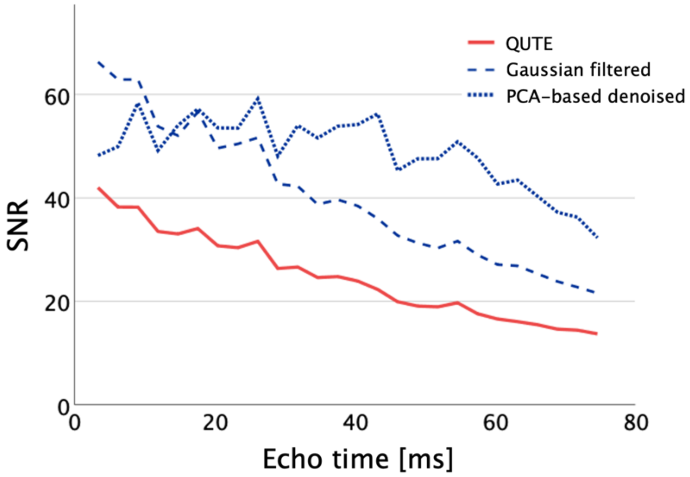

Figure 4.2 - SNR evolution with echo time for the QUTE, Gaussian filtered and PCA-based denoised data of a patient.

In figure 4.3, both denoising methods are seen to have high noise reduction effects across all slices of the brain, leading to a better contrast between the different tissues when compared to the original maps.

In addition, these effects were also noticeable throughout the echoes as shown in figure 4.4. Gaussian filtering is seen to supress details in the image, especially in the last echo times (indicated with a red arrow). In comparison, PCA-based denoised maps are seen to discriminate signal from noise without smoothing of the surrounding neighbour voxels.

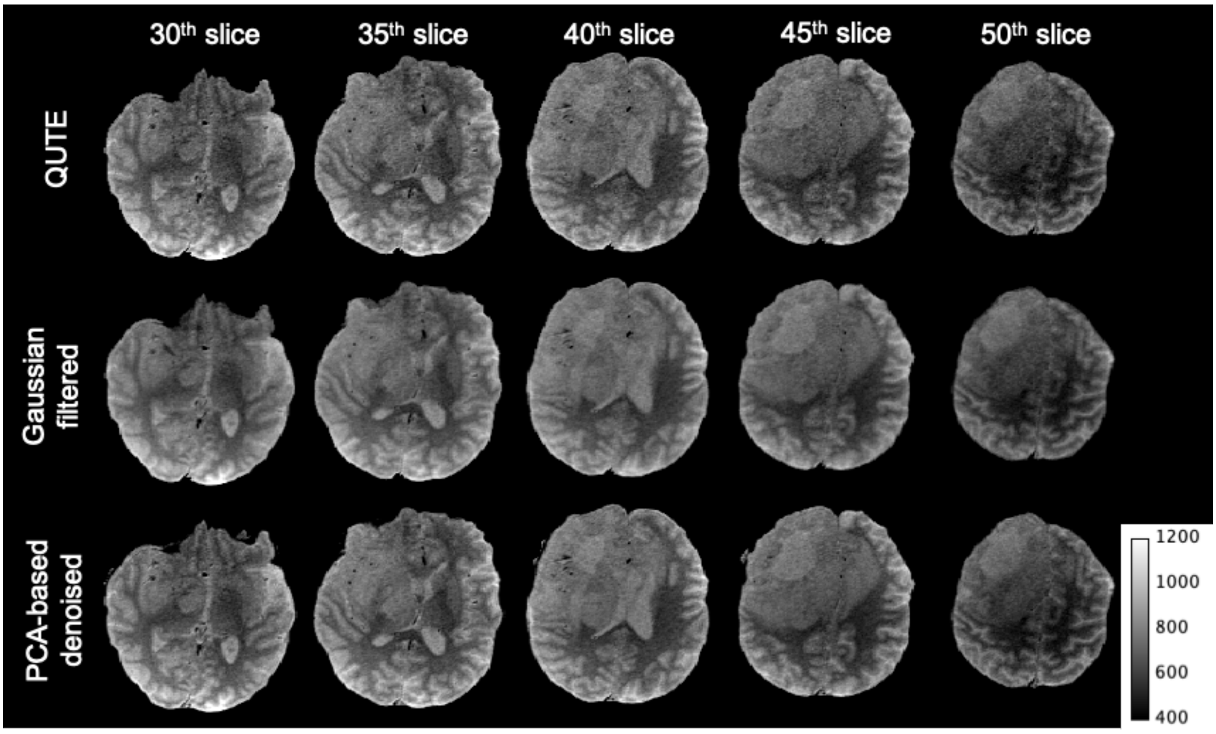

Figure 4.3 – Qualitative effects of the noise reduction methods on the QUTE data for the first echo of different slices.

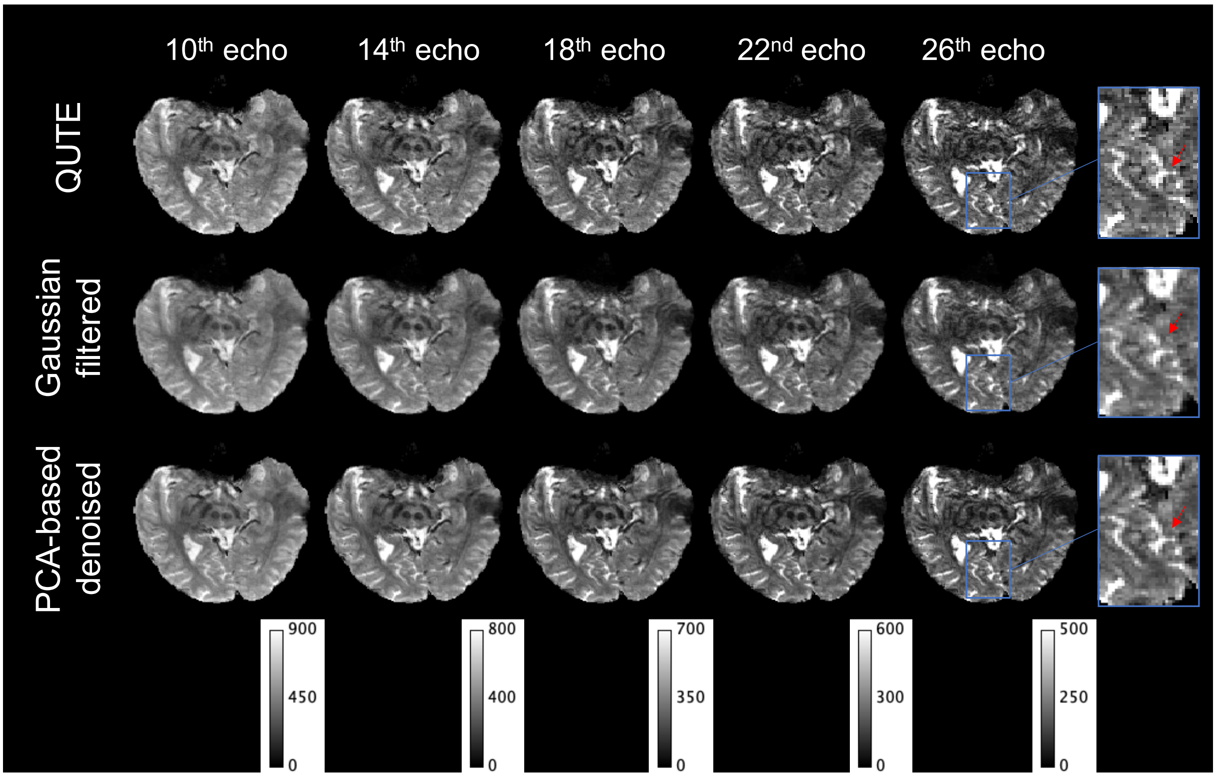

Figure 4.4 - Qualitative effects of the noise reduction methods on the QUTE data for different echo times in the same selected slice.

4.1.2 Macroscopic field inhomogeneity correction

The field corrected maps did not show notable qualitative differences for the first echoes (see figure 4.5). However, the SNR for the same region on the $\sigma^{[1]}$ maps and $\sigma^{[2]}$ maps was found to be lower than the SNR of the original data while that one of the sinc correction maps was found to be equal. Figure 4.6 shows the calculated SNR for each echo time of the original and field corrected data in a selected region near the ear canal.

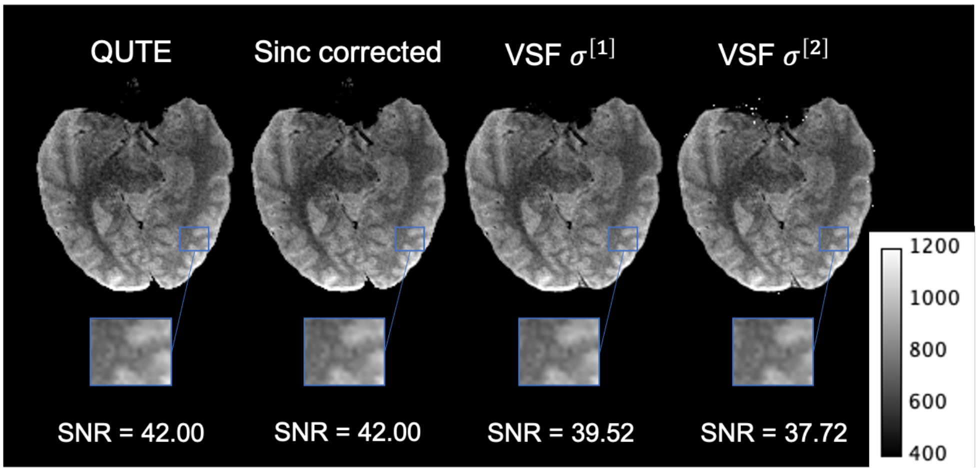

Figure 4.5 - Visual effects of the field inhomogeneity correction methods on the first echo of a selected slice.

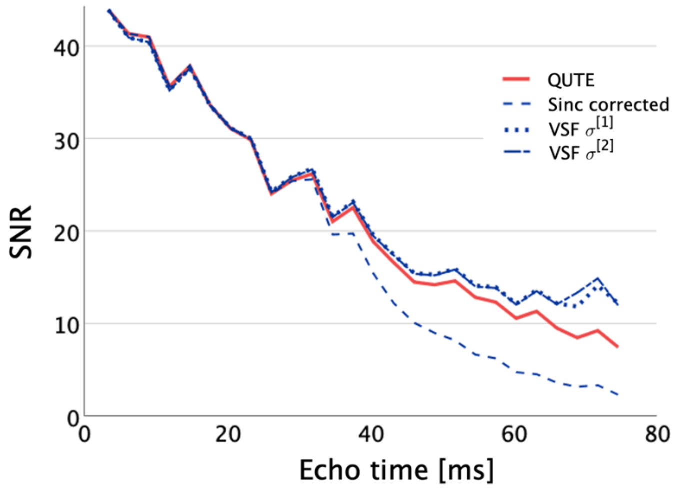

Figure 4.6 - SNR evolution with echo time for the QUTE, sinc corrected, $\sigma^{[1]}$ *and* $\sigma^{[2]}$ *data of a patient.*

Unlike the SNR evolution of the PCA-based denoised data, the SNR for the sinc corrected, $\sigma^{[1]}$ and $\sigma^{[2]}$ data are seen to decrease with TE. In figure 4.6 the SNR of the sinc corrected data decays faster to values close to zero around ($\mathrm{TE} = 40$ ms) than the remaining methods.

In figure 4.7 are shown the effects of the field corrections methods on multiple echoes. Macroscopic field inhomogeneities stand out over time. All three methods try to compensate for this high rate of decay that is notable close to the ear canals and nasal cavities and often surrounded by an undulating effect that distorts the image.

On the one hand, the sinc correction method did not appear to recover the lost signal (red arrow). Instead, the voxels in and around the affected regions seemed to be set to values close to zero. On the other hand, the VSF correction showed that for both, $\sigma^{[1]}$ and $\sigma^{[2]}$, the voxels near the air cavities (green arrows) are being compensated but filled with too high values, higher than those of CSF. Also, the outer brain voxels, near the skull, are being undesirably affected (yellow arrow). For each echo, the percentage of voxels undesirably affected by the VSF approaches was calculated. For the presented slice in figure 4.6, the percentage of voxels with differences in the signal decay higher than 100 between the VSF maps and the non-corrected map was approximately 6.3% and 5.8% in the last echo for the $\sigma^{[1]}$ and $\sigma^{[2]}$, respectively. Visually, both field correction approaches did not appear to compensate for the signal oscillations (undulating patterns) near the signal drop off areas.

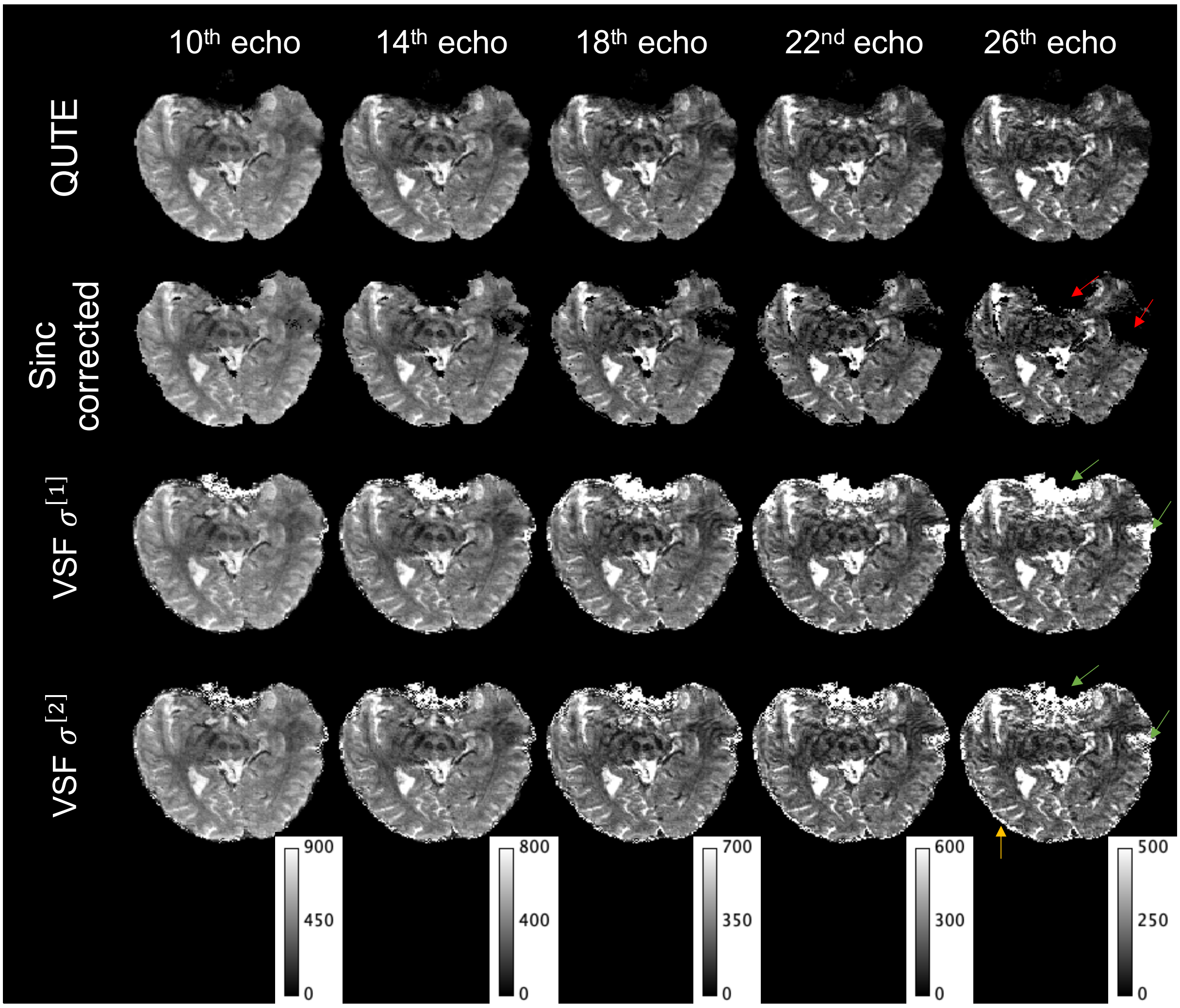

Figure 4.7 - Effects of the field correction methods on the 10th, 14th, 18th, 22nd and 26th echoes of a selected slice. The red and green arrows point at the voxels near the ear canal and the nasal cavities in the sinc corrected and VSF maps, respectively. The yellow arrow points at the outer borders/voxels of the brain.

4.1.3 Signal decay

Figure 4.8 shows the average signal decay for the original, Gaussian filtered and PCA-based denoised data with the residuals of the exponential fit ((a), (b), (c), respectively) of a selected WM region (d). The differences between the original and Gaussian filtered data, and between original and PCA-based denoised data are plotted in (e) and (f), respectively. Figure 4.9 shows the average signal decay of the same selected region as in figure 4.8 for the sinc corrected, $\sigma^{[1]}$ and $\sigma^{[2]}$ data with the residuals of the exponential fit ((a), (b), (c), respectively). The differences between the original and sinc corrected data, original and $\sigma^{[1]}$ data, and original and $\sigma^{[2]}$ data can be seen in (d), (e) and (f), respectively. Table 4.1 summarises the statistics of the exponential regression using the linear model $y = a\,e^{bx} \rightarrow \ln(y) = \ln a + bx$.

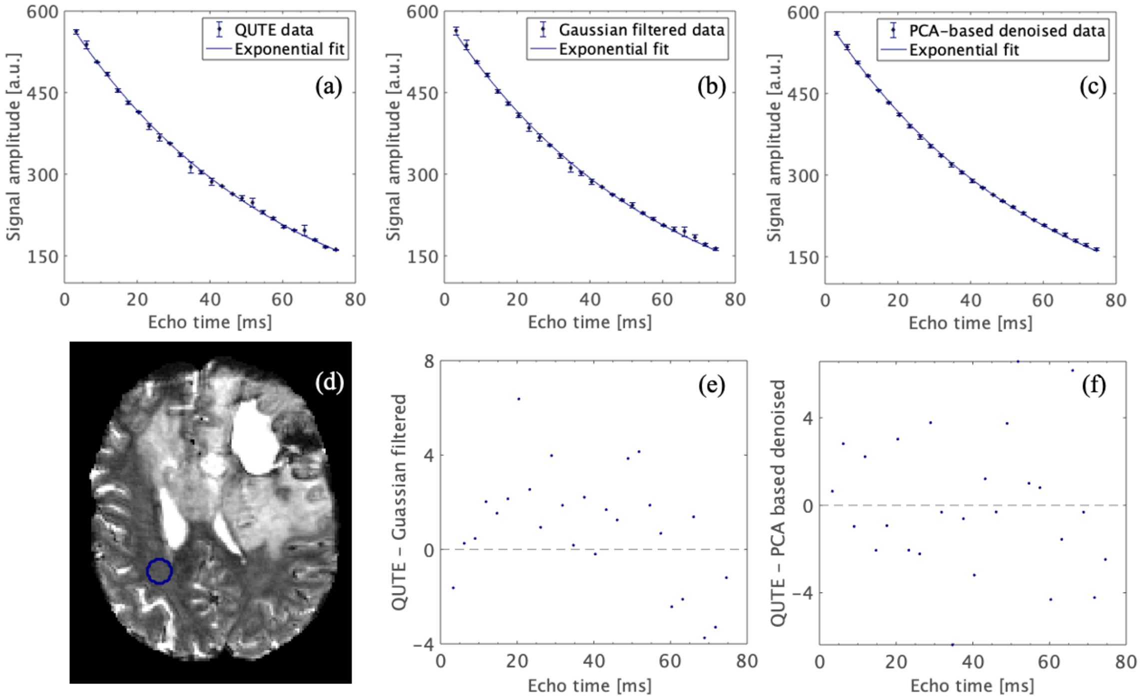

Figure 4.8 - Representation of the signal decay and the exponential fit of the QUTE data (a), Gaussian filtered data (b), PCA-based denoised data (c) of a selected WM region of a patient (d). Plotted differences between QUTE and Gaussian filtered data (e) and QUTE and PCA-based denoised data (f).

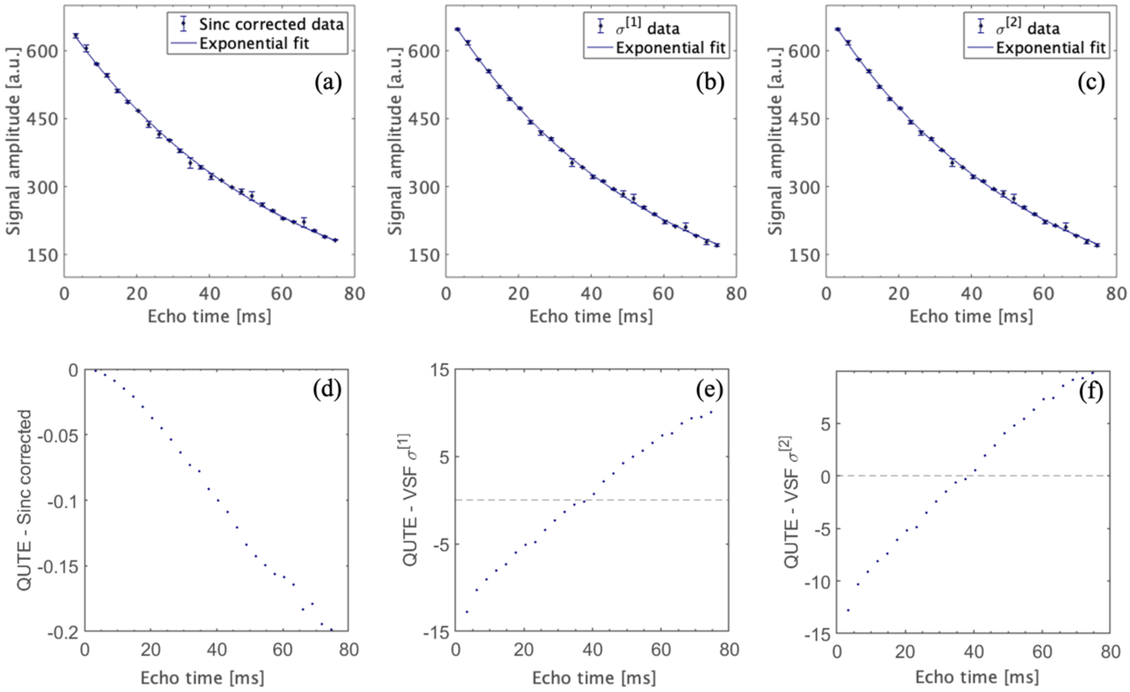

Figure 4.9 - Representation of the signal decay and the exponential fit of the sinc corrected data (a), $\sigma^{[1]}$ data (b), $\sigma^{[2]}$data (c) of the same region as in figure 4.8. Plotted differences between QUTE and sinc corrected data (d), QUTE and $\sigma^{[1]}$ data (e) and QUTE and $\sigma^{[2]}$ data (f).

Table 4.1 – Summary statistics of the average signal decay model for the different methods of the WM region showed in figure 4.8.

	QUTE	Gaussian filtered	PCA-based denoised	Sinc corrected	VSF $\sigma^{[1]}$	VSF $\sigma^{[2]}$
RMSE	0.016	0.015	0.008	0.017	0.016	0.016
r^2	0.998	0.998	0.999	0.998	0.999	0.999
p-value for the F-test of the model	<0.05	<0.05	<0.05	<0.05	<0.05	<0.05

In both, figure 4.8 and figure 4.9, the average signal decay in the selected region presented an exponential behaviour confirmed with the F-test on the regression model, for all the used methods. The differences between the original and sinc corrected data, figure 4.9 (d), are very small, meaning that the signal decay is only slightly affected in that region. In figures 4.9 (e) and (f) it can be seen that the VSF correction is affecting more the first and last echoes than the middle ones.

To test the performance of the corrections in the inhomogeneity regions, the procedure was repeated for a region near the ear canal. The results can be seen in figure 4.10 and 4.11. Table 4.2 summarises the statistics of the exponential regression.

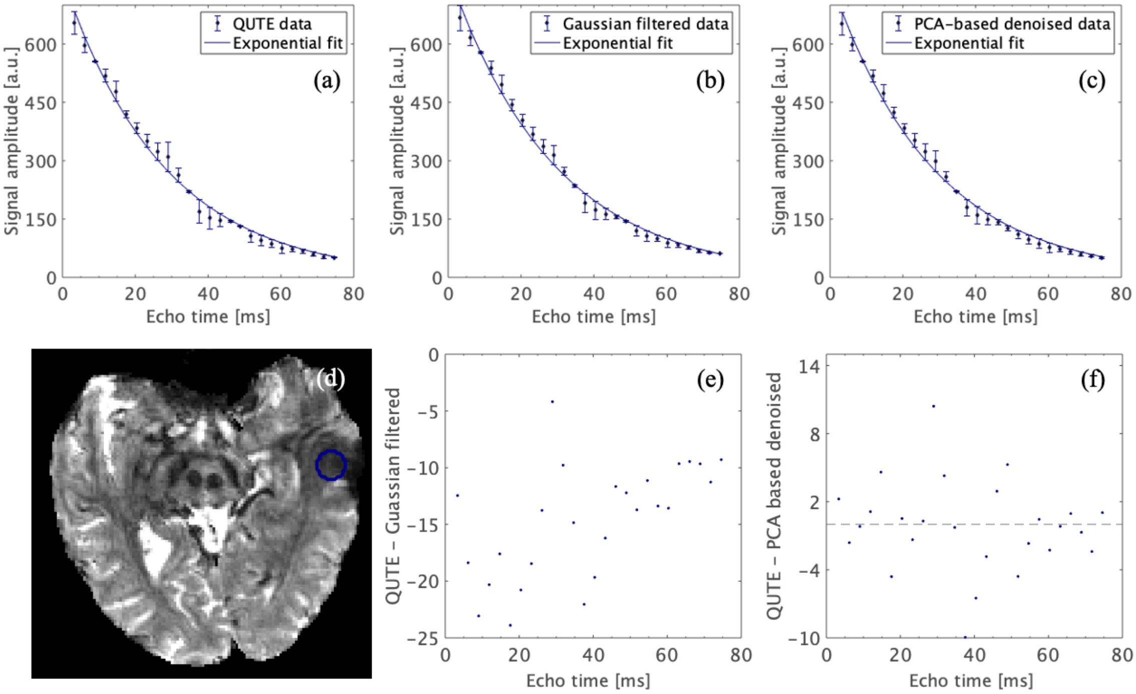

Figure 4.10 - Representation of the signal decay and the exponential fit of the QUTE data (a), Gaussian filtered data (b), PCA-based denoised data (c) of a selected region near the ear canal of a patient (d). Plotted differences between QUTE and Gaussian filtered data (e) and QUTE and PCA-based denoised data (f).

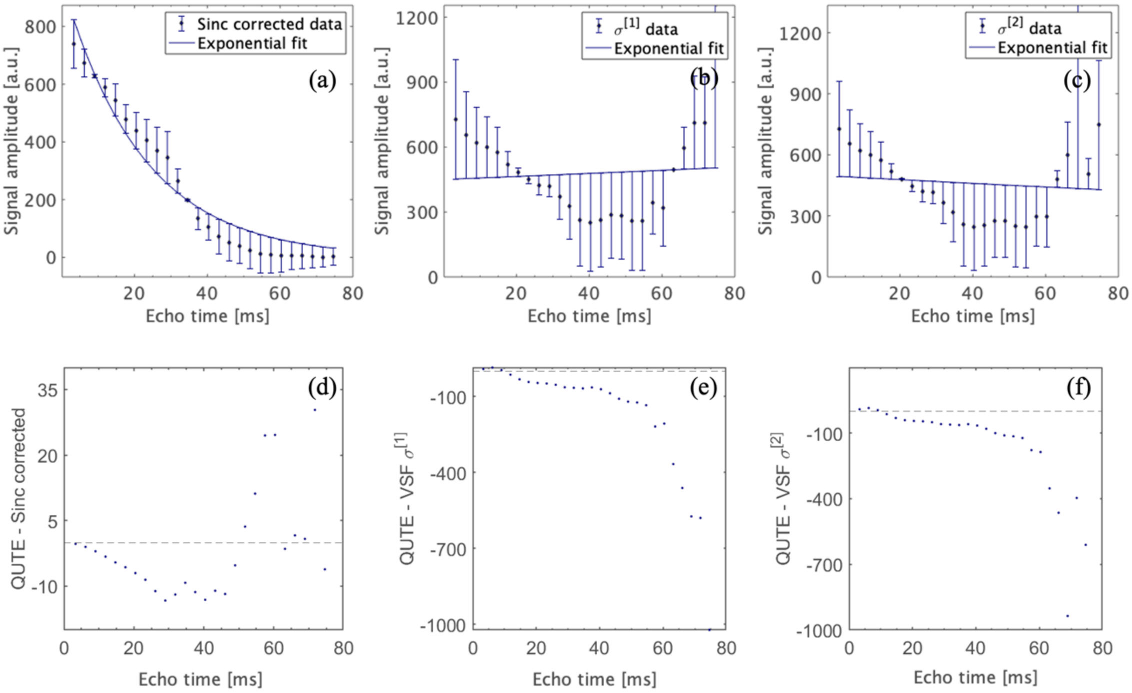

Figure 4.11 - Representation of the signal decay and the exponential fit of the sinc corrected data (a), $\sigma^{[1]}$ data (b), $\sigma^{[2]}$data (c) of the same region as in figure 4.10. Plotted differences between QUTE and sinc corrected data (d), QUTE and $\sigma^{[1]}$ data (e) and QUTE and $\sigma^{[2]}$ data (f).

Table 4.2 - Summary statistics of the average signal decay model for the different methods of the ear canal region showed in figure 4.10.

	QUTE	Gaussian filtered	PCA-based denoised	Sinc corrected	VSF $\sigma^{[1]}$	VSF $\sigma^{[2]}$
RMSE	0.070	0.055	0.054	0.553	0.427	0.425
r^2	0.993	0.995	0.996	0.936	0.006	0.028
p-value for the F-test of the model	<0.05	<0.05	<0.05	<0.05	>0.05	>0.05

The signal decay in figure 4.10 (a) shows small deviations from the previous signal decay found in figure 4.8 (a). Both Gaussian filtering and PCA-based denoised methods presented higher differences from the QUTE data in the region next to the ear canal than in the WM region of figure 4.8, demonstrating the effect of field distortions caused next to the air-tissue interfaces in the average signal decay. Figure 4.11 (a) and (d) show that the sinc correction method appears to compensate the original signal by increasing the signal intensity after the initial echoes, while the last ones are set to values close to zero. The root mean square error (RMSE), in the area next to the ear canal, increased from 0.070 in the original data to 0.553 after applying the sinc correction method. This indicates that the variance of the residuals is much higher than in the original and denoised data. Figure 4.11 (b) and (c) shows that the average signal decay calculated from the VSF maps near the ear canal did not present an exponential behaviour, mainly due to the last echoes. In fact, as previously demonstrated in figure 4.7, the signal amplitude in the last echoes next to air cavities is shown to be overestimated in both $\sigma^{[1]}$ and $\sigma^{[2]}$ approaches. Accordingly, the F-test on the regression model revealed that an exponential curve was no longer suitable for the fit.

In summary, this section presents a comparison between the different corrections approaches used. Both Gaussian filtering and PCA-based denoising methods have been shown to reduce noise in the MR images. Often, denoising approaches assume noise to be Gaussian, which can be effectively removed with a Gaussian filter [70]. However, noise in MRI can depend on the image reconstruction method used and then violate the Gaussian noise assumption [65]. In this study, the type of noise dominating the MR image was not studied, but including the phase data, such as in the PCA-based denoising method, has major advantages. First, the noise distribution of complex data after inverse Fourier transformation is still Gaussian [71], which makes it feasible to assume a Gaussian distribution of the noise without evaluating the type of noise distribution. Second, including the phase into the denoising process allows to provide additional denoised phase information, essential for background field correction. Third, complex denoising leads to an improved denoising in the magnitude for the last echoes, which is also reflected in the SNR, when compared with the remaining methods. Disadvantages arise when phase induced artifacts are undesirable included in the magnitude image. This effect can be compensated with an additional background phase correction step, which makes the inclusion of phase images in complex denoising an advantageous approach.

Moreover, the effects of macroscopic magnetic field correction methods were studied with no prior denoising approach. The behaviour of the signal with increasing TE generally follows an exponential decay, which was not verified in voxels near the ear canal or near the nasal cavities, mainly due to air-tissue susceptibility differences. It was expected that the sinc correction and VSF methods would correct the decay and return its exponential shape. The sinc correction method was testes by varying the number of echoes being considered into the final signal equation. However, this fitting approach did not appear to be robust since in many voxels the sinc modulation and the exponential decay were indistinguishable. In regions where the susceptibility induced field inhomogeneities were critical, the signal decay tended to behave even more complex (non-ideal). The VSF approach was reported to have significant effects in 3D experiments [55]. In this thesis, where the mGRE data were acquired with 2D experiments, this was not verified, which might be related to the fact that VSF does not consider signal contamination from the z-direction. Therefore, the degree of difference may depend on how strong the field inhomogeneity gradient is along the z-direction. Furthermore, in this work, only one neighbouring voxel in the x- and y-directions was used. In principle, an increase in the size of the neighbourhood leads to more accurate the results, although with some limitations. If neighbouring voxels are contaminated significantly by the macroscopic field inhomogeneities, the results are expected to have errors. The higher the number of neighbouring voxels, the higher the memory and computational time needed. Both correction methods revealed to have higher influence in the last echoes than in the first ones, demonstrating the dependency over time.

4.2 T_2* fitting

4.2.1 Mono-exponential relaxometry

The computed T_2* maps with the mono-exponential relaxometry approach can be seen in figure 4.12, where five consecutive slices are shown, with relatively high field inhomogeneities above the nasal cavities, chosen to demonstrate the effect of the corrections. The PCA-based denoised maps are very smoothed which provides a lower T_2* contrast and blurred edges between the different structures. The sinc corrected maps appear to slightly reduce artificial shortening of T_2* in the B_0 inhomogeneity region near the nasal cavities. However, in the outer borders of the brain, it can be seen an over estimation of the typical tissue-specific values. Visually, both VSF approaches do not appear to have differences in the estimated T_2* maps. It can be seen an over estimation in the outer borders of the brain and more significantly in the B_0 inhomogeneity region being considered, i.e. the nasal cavity.

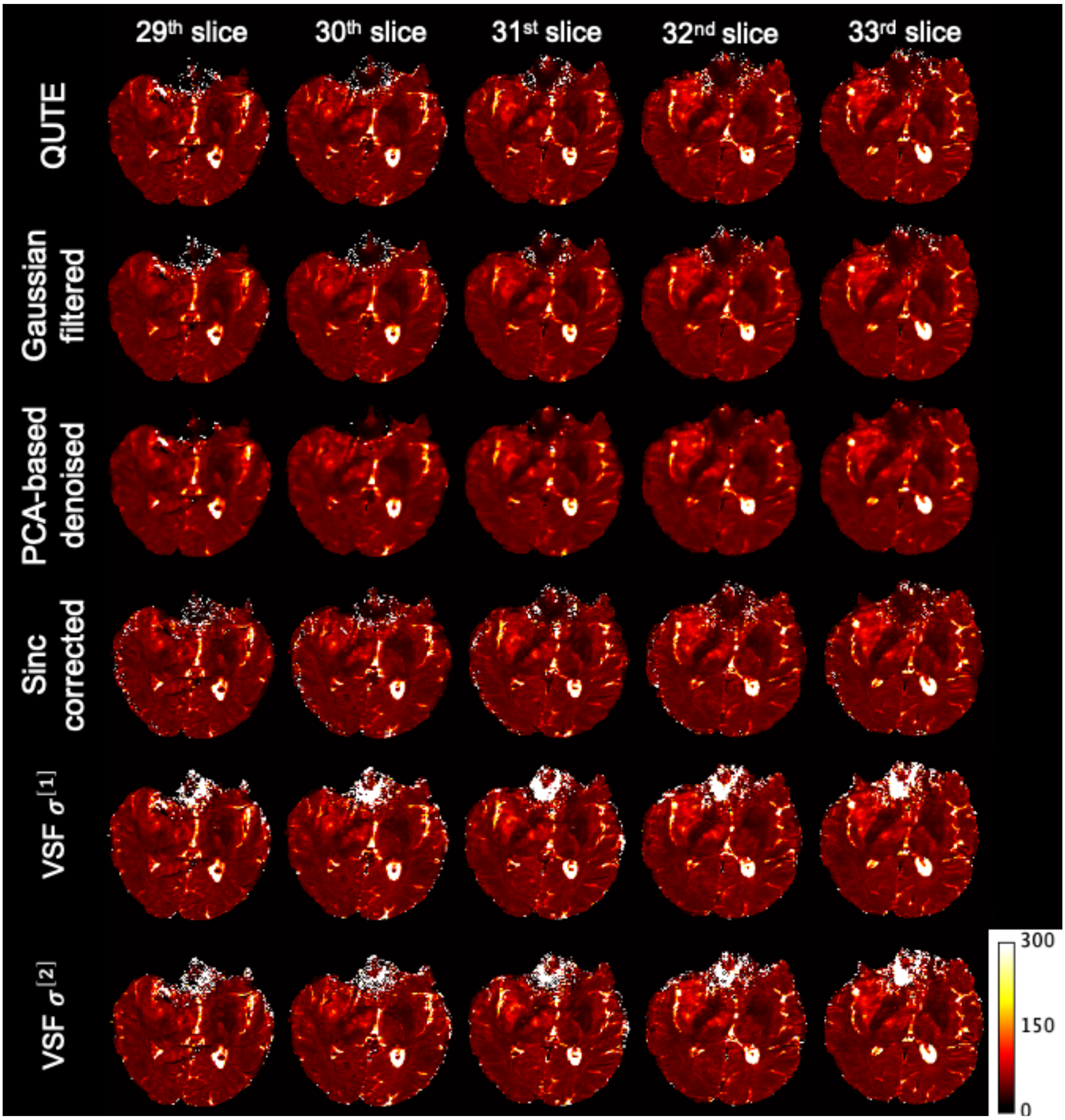

Figure 4.12 - Comparison of the QUTE T_2 maps with the corrected T_2* maps of five adjacent slices. Scale in ms.*

The mean T_2* of each ROI was calculated for the selected slice of each patient and used to plot the boxplots in figure 4.13. Table 4.3 presents the overall mean T_2* of the 33 patients and the standard deviation over the different methods and ROIs.

In figure 4.13, outliers are represented with circles for values between 1.5 and 3 times the interquartile range, and with stars for values with more than 3 times the interquartile range. The presence of outliers in the tumour, oedema and CSF regions was found to be higher, and accompanied with a higher variance of the mean T_2*, when compared to normal tissue regions.

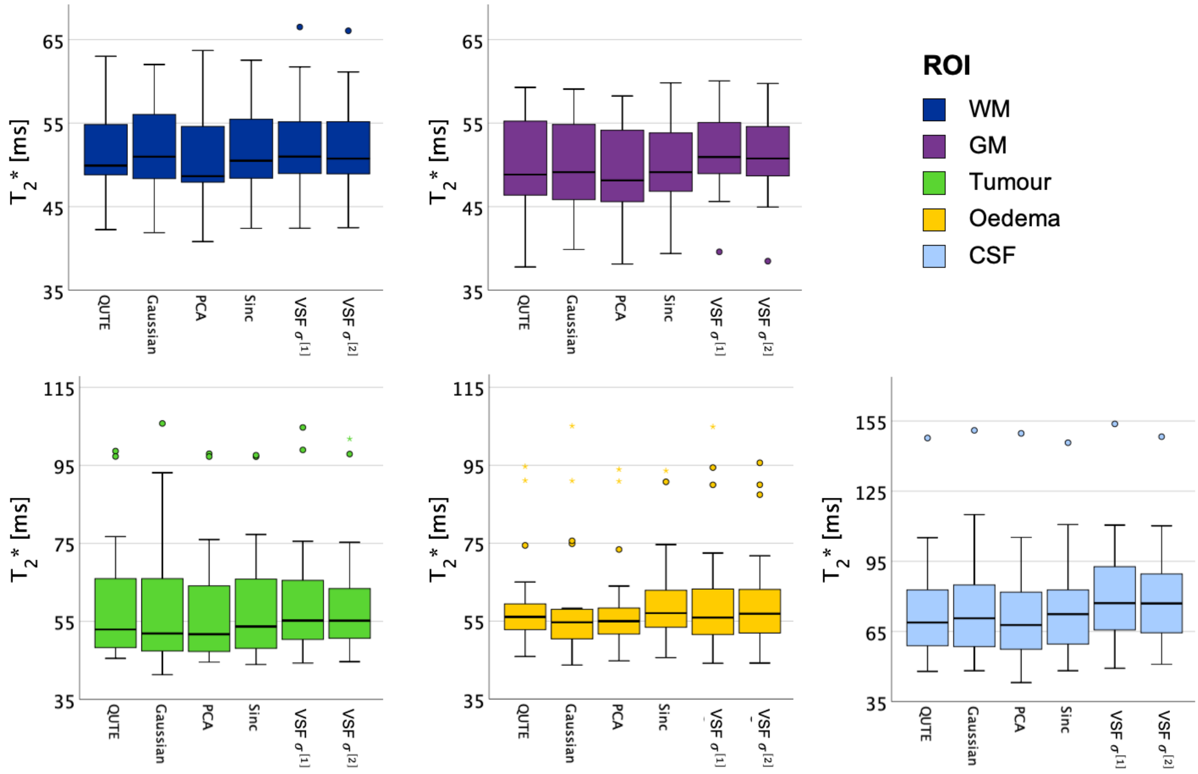

Figure 4.13 - Boxplots of the mean T_2 of the 33 patients in WM, GM, tumour, oedema and CSF for all not corrected and corrected data.*

Table 4.3 – Mean T_2 ± standard deviation of the 33 patients calculated with a mono-exponential approach. The values are given in ms.*

	QUTE	Gaussian filtered	PCA-based denoised	Sinc corrected	VSF $\sigma^{[1]}$	VSF $\sigma^{[2]}$
WM	51.79 ± 4.99	51.77 ± 4.98	50.87 ± 5.23	51.97 ± 4.91	50.30 ± 5.07	52.03 ± 4.97
GM	49.91 ± 5.27	50.02 ± 5.01	49.09 ± 5.14	50.08 ± 5.00	51.81 ± 4.48	51.47 ± 4.52
CSF	72.58 ± 19.77	74.64 ± 20.91	71.70 ± 20.45	74.19 ± 19.36	79.66 ± 19.91	78.53 ± 19.57
Tumour	58.52 ± 13.45	57.78 ± 14.83	57.41 ± 13.56	58.81 ± 13.55	59.53 ± 13.87	59.16 ± 13.22
Oedema	59.10 ± 12.36	58.53 ± 14.79	57.93 ± 12.62	59.78 ± 12.21	61.06 ± 15.78	60.49 ± 13.93

For the statistical analysis, all groups were tested for normality and homogeneity of variances with Shapiro-Wilk test and Levene's test, respectively. The results showed significant evidence to reject the null hypotheses ($p<0.05$) of normality and/or equal variances in all groups. Therefore, the non-parametric Kruskal-Wallis test was used.

Significant differences in the mean T_2* values between ROIs were found and are summarised in table 7.1 of the appendix. The medians of the WM and GM groups and between the tumour and oedema groups did not reveal to be statistically significantly different either for original or corrected data. The differences between the medians of the WM and oedema groups were only not statistically significant for the Gaussian filtered data. Between the WM and the tumour regions, only the VSF approach revealed statically significant differences between the medians. The remaining groups revealed statically significant differences between the medians.

Unlike the values reported in the literature [8], the mean T_2* of WM was found to be slightly higher than for GM, except for the data corrected with the VSF $\sigma^{[1]}$ approach. The calculated mean T_2* in the tumour and oedema regions revealed to be considerably lower than the mean T_2* reported in [8]. While in this work the mean T_2* in both tumour and oedema regions was found to be around 58/59 ms, in the literature the mean T_2* for the same regions was reported to be around 71 ms. Additionally, the standard deviation in the tumour region was found to be smaller than in [8], i.e., the range of the calculated mean T_2* in this study (mean T_2* in the tumour region ranging between 43 and 73 ms) is not fully covered by the reported values in the same region type (mean T_2* in the tumour region ranging between 51 and 90 ms). From a microstructural point of view, tumours are known to be quite heterogeneous [58], which is reflected in the T_2* values. Moreover, a change in the studied sample may imply that the observed T_2* mean is different since each case has its own characteristics. Although this might explain the differences found in the pathological tissues, the values reported in the CSF regions were found to be lower than what would be expected. In fact, CSF regions are generally water regions leading to longer T_2* relaxations. A more reasonable explanation would rely in imperfect masks, as some of normal appearing voxels may be included in the CSF masks.

4.2.2 Multi-exponential relaxometry

In the multi-exponential relaxometry study, data were analysed with the NNLS algorithm with regularisation on a voxel-by-voxel basis. The algorithm needs the user to tune three parameters in order to increase the performance and reduce computational time. These parameters are the T_2* space and the λ range that regularises the solution according to the defined χ^2 restrictions.

The range of T_2* values in the brain are known from the literature and were initially set from 1 to 300 ms. The produced S_0 and T_2* maps, however, were very noisy, as it can be seen on the left in figure 4.14. By increasing the lowest T_2* point to 5 ms, the brighter undesired voxels disappeared as it can be seen on the right of figure 4.14.

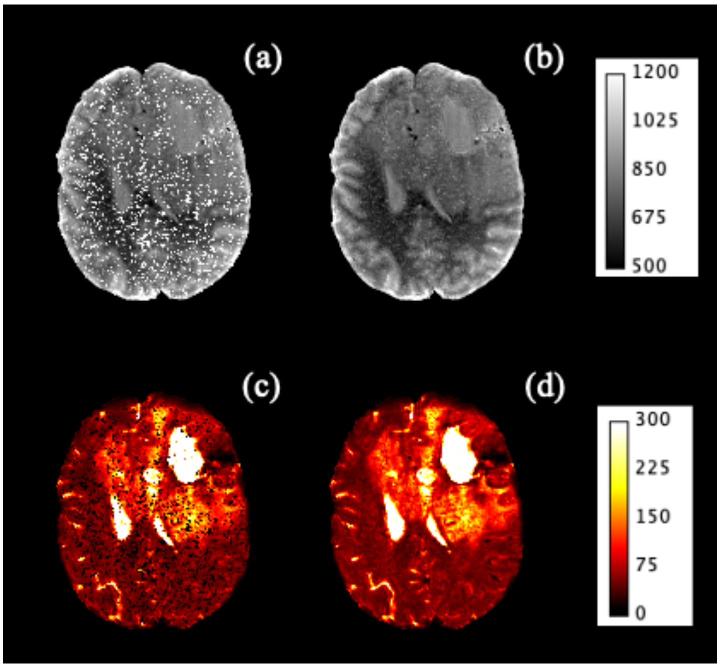

Figure 4.14 - On the left, a) and c) depict the S_0 and T_2 maps obtained with T_2* space between 1 and 300 ms, respectively. On the right, b) and d) depict the S_0 and T_2* maps obtained with T_2* space between 5 and 300 ms, respectively.*

The L-curve method was implemented in order to define the proper range of λ. Additionally, the influences of logarithmically and linearly samples of both T_2* and λ ranges were studied, and the results are shown in figures 4.15 and 4.16. The L-curves of representative voxels (one of each ROI) are plotted in the upper row of figure 4.15, and their respective curvatures with respect to λ in the bottom row. The left-hand side of figure 4.15 has both T_2* and λ logarithmically sampled, while on the hand-right λ is linearly sampled.

Logarithmically spaced points result in a bigger number of data points near the initial value of the interval. We intended to study longer components of T_2* (tumour components) and therefore linear sampling of the T_2* vector would be more appropriated.

Figure 4.16, analogously to figure 4.15, shows the L-curves and respective curvature plots for representative voxels. The left-hand side of figure 4.16 shows the plots for T_2* linearly sampled, while λ is logarithmically sampled; and on the right-hand side, both T_2* and λ are linearly sampled.

The corner of the L-curve corresponds to the ideal regularisation parameter in the considered voxel, given by the maximum curvature value of the L-curve. Only small changes in the regularisation values were found when comparing the logarithmically and linearly sampling of T_2*, by keeping the same sampling for λ. However, the regularisation parameters change significantly when using linear sampling for the λ range, where the shape of the curvature graph shows that only very few regularisation values were used to sample the L-curve corner. To overcome this problem, the number of steps in the regularisation range could be increased which would increase the computation time linearly, since the regularised NNLS algorithm tests all λ values until it finds the first one to satisfy the allowed misfit interval.

Generally, the tumour and oedema voxels showed to have smoother L-curves, i.e. smaller curvature, and therefore the plotted curvatures are blunter when compared with the curvatures of normal appearing tissue voxels.

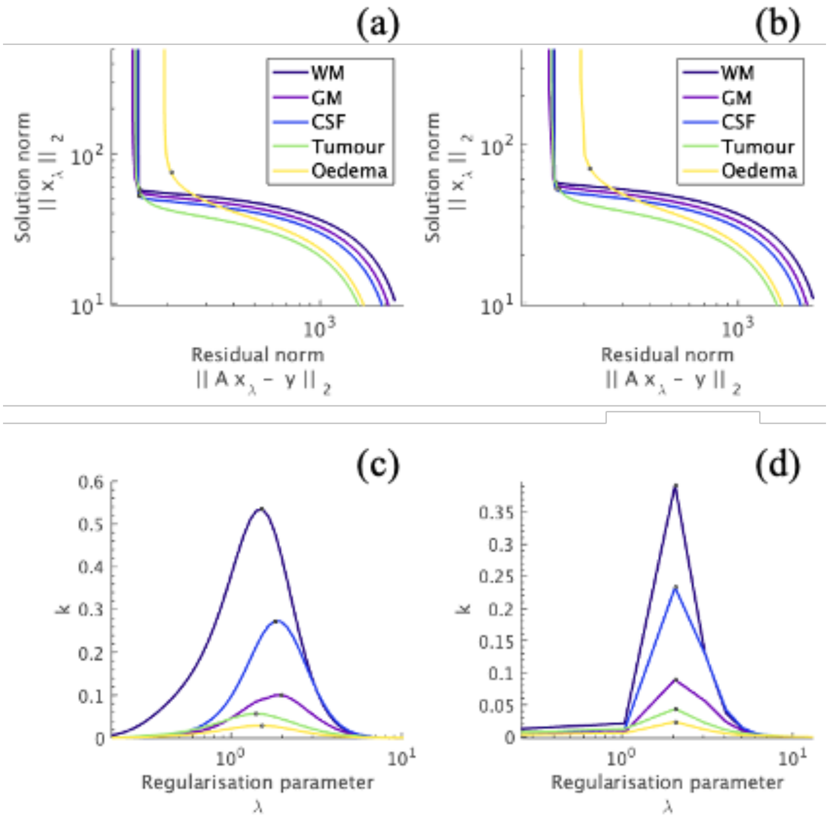

Figure 4.15 - Representation of the L-curves (a) and (b) and the corresponding curvatures (c) and (d) of 5 voxels of each ROI. On the left, the T_2 and the λ ranges are logarithmically sampled. On the right, the T_2* range is logarithmically sampled and the λ range is linearly sampled.*

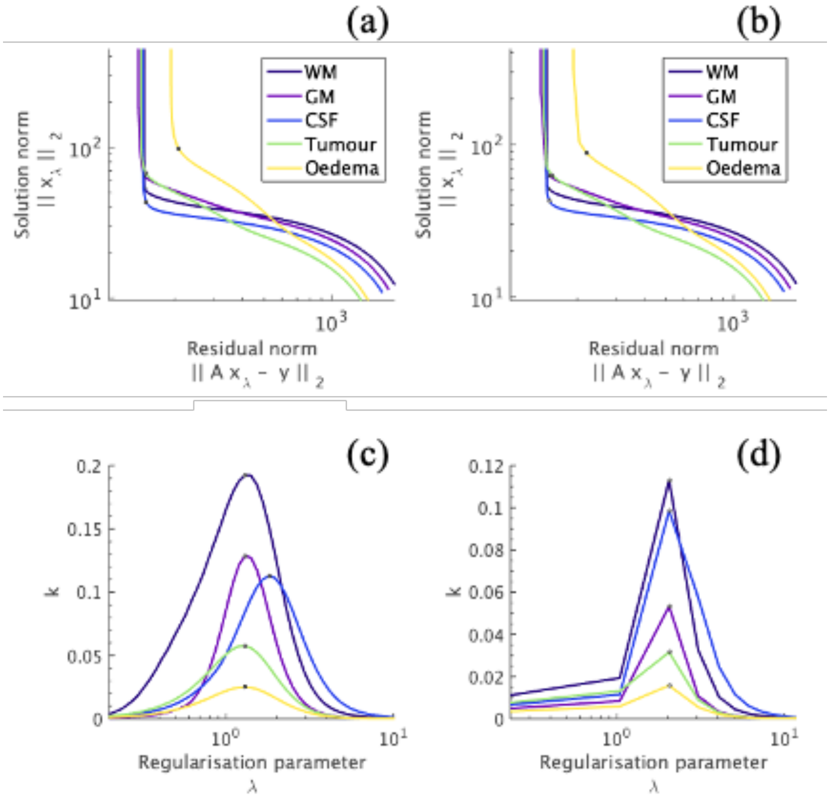

Figure 4.16 - Representation of the L-curves (a) and (b) and the corresponding curvatures (c) and (d) of 5 voxels of each ROI. On the left, the T_2 range is linearly sampled and the λ range is logarithmically sampled. T_2* and the λ ranges are logarithmically sampled. On the right, the T_2* and the λ ranges are linearly sampled.*

The final solution was found iteratively, by increasing the regularisation parameter in each step according to the χ^2 constraint. Although the L-curve method should retrieve the ideal regularisation parameters (to define a range containing all these values), the final solutions were over-regularised and multiple compartments were put together in a blunter spectrum.

Therefore, the range of values of λ over a logarithmically spaced vector was changed from [-1, 0.5] to [-2,0.1], and the allowed interval for misfit was $1.005 \cdot \chi^2_{min} \leq \chi^2 \leq 1.010 \cdot \chi^2_{min}$. Figure 4.17 displays the effect of different regularisation strengths in the NNLS solutions for one voxel.

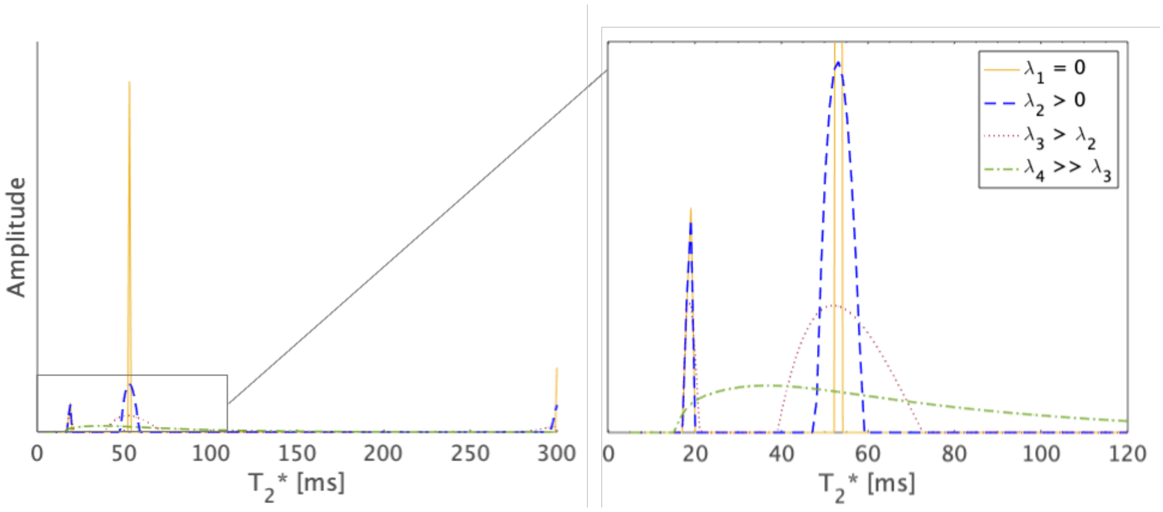

Figure 4.17 - Influence of the regularisation parameter in the NNLS solutions.

When the χ^2constraints are higher, the used λ is also higher, as it can be seen in figure 4.18. Here, both maps show the regularisation values for each voxel used by the regularised NNLS (rNNLS) algorithm. The used inputs were T_2* linearly spaced between 5 and 300 ms (295 steps), λ logarithmically spaced from -2 to 0.1 (20 steps) with the constraint a) $1.020 \cdot \chi^2_{min} \leq \chi^2 \leq 1.025 \cdot \chi^2_{min}$ and b) $1.005 \cdot \chi^2_{min} \leq \chi^2 \leq 1.010 \cdot \chi^2_{min}$.

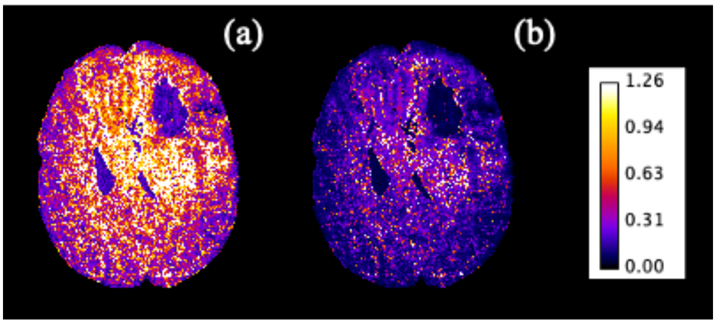

Figure 4.18 - Representation of the regularisation values for each voxel used by the NNLS algorithm. The used inputs were T_2 linearly spaced between 5 and 300 ms (295 steps), λ logarithmically spaced from -2 to 0.1 (20 steps) with the constraint a) $1.020 \cdot \chi^2_{min} \leq \chi^2 \leq 1.025 \cdot \chi^2_{min}$ and b) $1.005 \cdot \chi^2_{min} \leq \chi^2 \leq 1.010 \cdot \chi^2_{min}$.*

Figure 4.18 shows that the regularisation values used in the pathological regions were mostly higher than the regularisation values used in normal appearing tissue. Also, low regularisation values were found in regions consisting mainly of water (ventricles and removed tumour tissue area).

The gmT_2* of each ROI were calculated for the selected slice of each patient and used to plot the boxplots in figure 4.19. Table 4.4 presents the overall gmT_2* of the 33 patients and the standard deviation calculated with the multi-exponential approach.

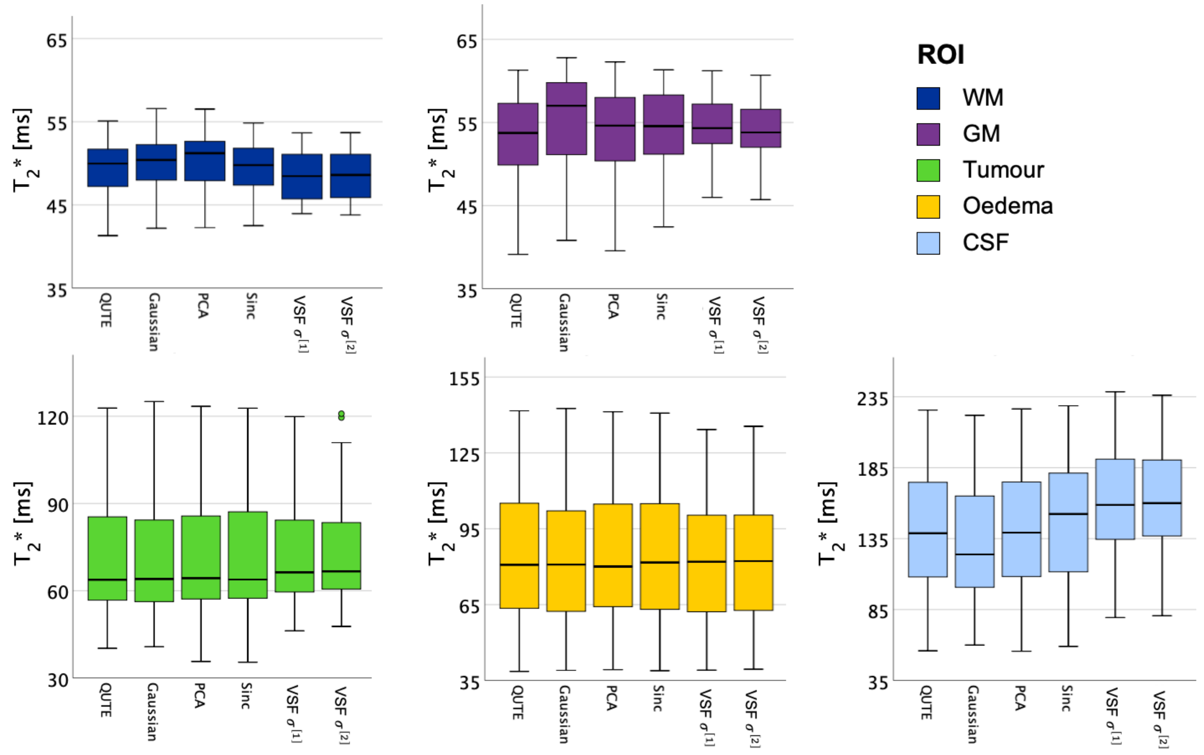

Figure 4.19 - Boxplots of the gm T_2 of the 33 patients in WM, GM, tumour, oedema and CSF for original and corrected data.*

Table 4.4 – Geometric mean T_2 ± standard deviation of the 33 patients calculated with a multi-exponential approach. The values are given in ms.*

	QUTE	Gaussian filtered	PCA-based denoised	Sinc corrected	VSF $\sigma^{[1]}$	VSF $\sigma^{[2]}$
WM	49.34 ± 3.39	50.16 ± 3.30	50.43 ± 5.58	49.43 ± 3.18	48.60 ± 3.01	48.63 ± 2.97
GM	53.42 ± 5.16	55.02 ± 5.39	54.02 ± 5.33	54.15 ± 4.69	54.68 ± 3.89	54.18± 3.84
CSF	140.48 ± 45.08	133.86 ± 44.18	140.52 ± 45.65	146.95 ± 44.52	162.45 ± 40.56	162.71 ± 39.86
Tumour	73.84 ± 28.40	73.56 ± 28.52	73.71 ± 28.54	74.20 ± 28.69	76.70 ± 25.46	77.29 ± 25.63
Oedema	83.49 ± 26.24	83.11 ± 25.99	83.84 ± 26.11	83.44 ± 25.97	82.57 ± 24.99	83.12 ± 25.16

As in the mono-exponential study, all groups were tested for normality and homogeneity of variances with Shapiro-Wilk test and Levene's test, respectively. Kruskal-Wallis test was used to find statically evidences.

The Kruskal-Wallis test did not reveal statistically significant differences between the different methods across the same ROI, except in the CSF region. In this case, significant differences in the medians were found between Gaussian filtered and VSF $\sigma^{[1]}$ data, Gaussian filtered and VSF $\sigma^{[2]}$ data, QUTE and VSF $\sigma^{[2]}$ data, and PCA-based denoised and VSF $\sigma^{[2]}$. Across ROIs, Kruskal-Wallis test did not reveal significant differences in the medians between the tumour and oedema regions, regardless of the used correction. On the other hand, and unlike in mono-exponential relaxometry, multi-exponential relaxometry revealed statistically significant differences between the medians of WM and GM for the Gaussian filtered, sinc corrected and VSF $\sigma^{[1]}$ data. Statistically significant differences were also found between the medians of all the remaining regions (in all used methods) and are summarised in table 7.2 of the appendix.

The gmT_2* in the GM region was found to be higher than the gmT_2* in the WM regions, and for both regions, similar to the literature values reported in [59]. Moreover, we observed that the gmT_2* is mostly higher in both pathological tissues, and CSF regions, when comparing it to the mean T_2* values obtained from a mono-exponential relaxometry. This can also be seen in figure 4.20. Accordingly, statistically significance differences were found between the mean T_2* values and gmT_2* of all ROIs, except for the WM calculated from the QUTE, Gaussian filtered, PCA-based denoised and sinc corrected data.

A wider range of the gmT_2* values was found, and the standard deviation is particularly high in the gmT_2* of CSF. In multi-exponential relaxometry, the outliers are mostly suppressed due to the application of regularisation.

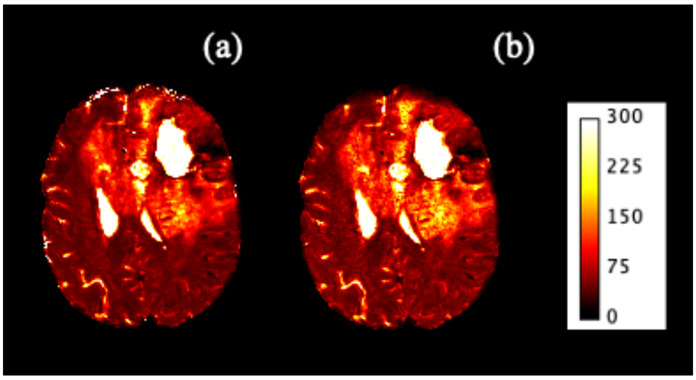

Figure 4.20 - Obtained T_2 maps of the QUTE data of a patient from the (a) mono- and (b) multi-exponential relaxometry approaches. Scale in ms.*

Visual inspection of the T_2* maps indicates that CSF regions would have long T_2* relaxation (~300 ms) which is not verified in the boxplots.

Figure 4.21 displays the boxplots of the gmT_2* for each voxel of the tumour mask in all 33 patients. It can be seen a large variability in the gmT_2* values within each tumour as well as across tumour patients.

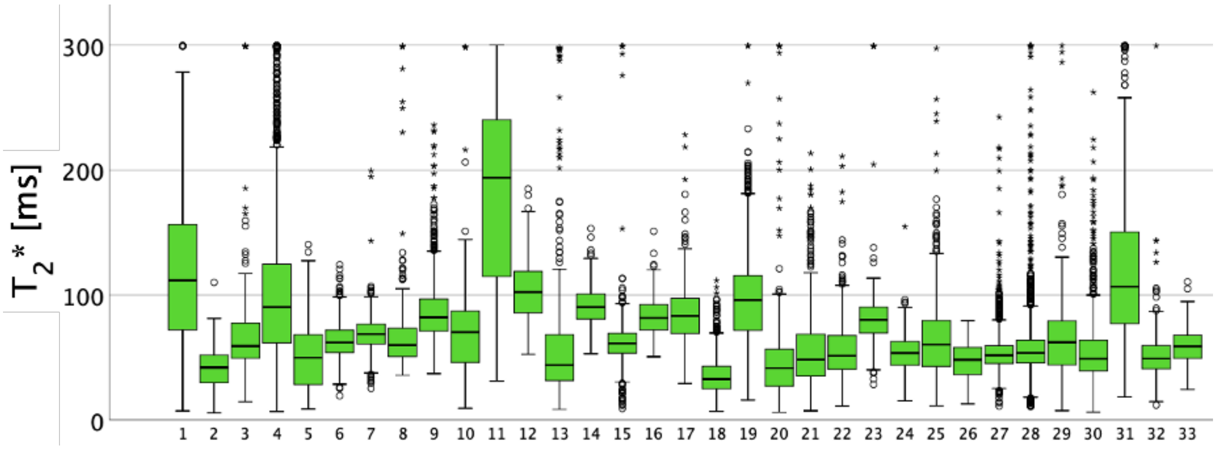

Figure 4.21 - Boxplots of the gmT₂ of all tumour voxels for the PCA-based denoised data across the 33 patients.*

In summary, regularisation algorithms are used in order to produce the most accurate solutions to ill-posed problems, although the ideal method is still a subject of research [68], [72]. In this thesis, the L-curve method was shown to produce a regularisation parameter that over-smooths the final solution, i.e., the estimated regularisation parameter was too large. Therefore, the L-curve criterion is seen to fail for the used mGRE data and other approaches might reveal to be more suitable. The *generalised cross validation criterion* that seeks to minimise the prediction error or the *discrepancy principle* that seeks to reveal when the residual vector is characterised by only noise [72] are examples of criteria to study.

T_2* relaxation curves from *in vivo* brains are very often multi-exponential. In this work, the mono-exponential fit has been shown to miss the initial relaxation components, leading to underestimated T_2* values. Unlike, mono-exponential relaxometry, multi-exponential relaxometry revealed significant differences between WM and GM, and between WM and tumour for the majority of the correction methods used.

4.2.3 Multicomponent T_2* relaxation in brain tumours

Due to the heterogeneity previously demonstrated, the following results were done individually. For an easier explanation, the results and discussion in this sub-section will be taken in 6 patients of different tumour types, and the shown spectra refer to those obtained with the PCA-based denoised data. The spectra corresponding to the other methods can be found in figures 7.2 and 7.3 of the appendix.

Figure 4.22 displays the T_2* distributions of the WM, GM, tumour and oedema regions in the 6 selected patients. It can be seen that the distributions of WM and GM are mostly in the same ranges, while the tumour and oedema distributions vary between patients. The distributions for CSF were not plotted for easy visualization of the other regions. The boxplots of figure 4.21 and the tumour T_2* distributions of all patients confirmed that no specific T_2* range could be defined to characterize the tumour region based on all voxels of the used tumour masks. This is indicative that the heterogeneity inside of the tumour region, as well as between tumours of different patients, might be limiting factors in the identification of a tumour-specific T_2* compartment.

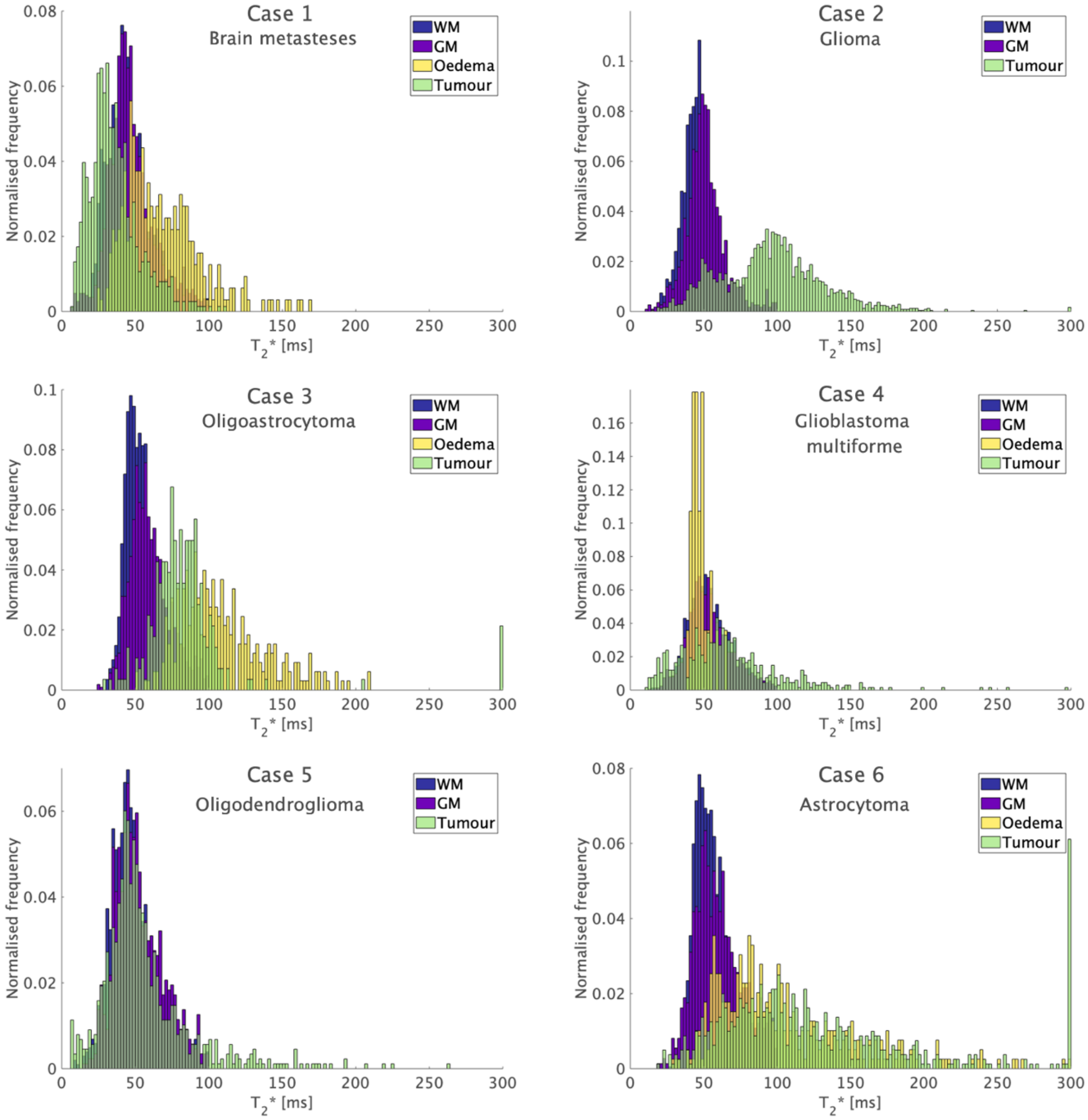

Figure 4.22 - T$_2$ distributions of the different ROIs in 6 patients with different tumour types.*

Small regions inside the tumour mask were manually selected to study multiple components in the T$_2$* spectrum (see figure 4.23). Although hyperintensities in the T$_2$* maps are often associated with pathologic tissue, some of the PET based tumour masks did not contain all of the brain regions characterised by this increased intensity (see figure 7.2 of the appendix).

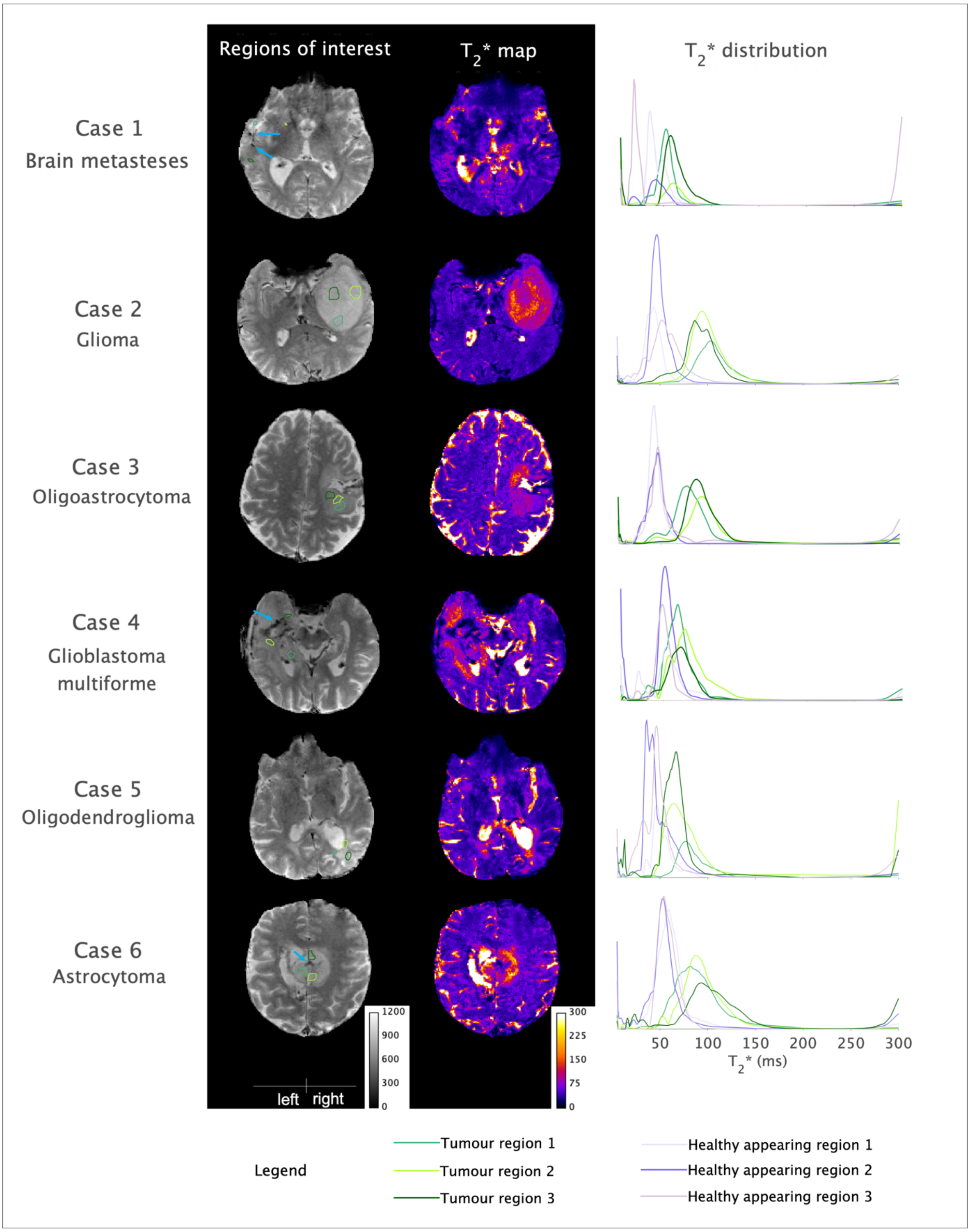

Figure 4.23 - T_2 distributions from various ROIs withing the tumour and from the contralateral regions for 6 patients. Vertical axis on T_2* distributions plots is intensity in arbitrary units. Blue arrows indicate necrotic region.*

Case 1 – Brian metastases

Case 1 corresponds to a patient with cerebral metastases spread throughout the brain and located necrotic tissue characterized by a darker colour in T_2*-weighted image (on the left side indicated by the blue arrow). In this case, the T_2* distributions in figure 4.23 exhibit a fair level of differentiation between the maximum peaks of the three selected pathologic regions (maximum peaks 53, 57 and 60 ms) relative to the corresponding contralateral healthy peaks (maximum peaks 19, 36 and 42 ms). Accordingly, a two-sample Kolmogorov-Smirnov test performed between the distribution of each selected tumour region and the corresponding normal appearing contralateral side revealed that the regions do not have the same continuous distribution at 5% significance level.

Some healthy regions present a short T_2* component around 16-19 ms which might be associated with higher iron concentrations while the T_2* components around 8-10 ms are typically associated to the presence of trapped water in the myelin sheets. The average of the maximum T_2* peaks and the standard deviation can be found in table 4.5.

Table 4.5 – Average ± standard deviation of the three T_2 peaks in the normal appearing and pathologic tissue for all used methods in case 1.*

	Average of maximum T_2* distribution peaks $\pm$ standard deviation (ms)	
	Normal appearing tissue	Pathologic tissue
QUTE	32.7 ± 12.3	55.7 ± 3.2
Gaussian filtered	39.3 ± 13.2	54.0 ± 8.5
PCA-based denoised	32.3 ± 11.9	56.7 ± 3.5
Sinc corrected	36.7 ± 16.9	52.3 ± 2.9
VSF $\sigma^{[1]}$	31.0 ± 13.5	58.3 ± 7.4
VSF $\sigma^{[2]}$	30.0 ± 13.7	57.7 ± 7.6

The gmT_2* of the presented regions can be found in the table 7.3 of the appendix.

Additionally, other small areas of the tumour mask were studied. The distributions of the new regions seemed to be similar to the T_2* spectra previously assigned to intra/extracellular water. The tumour regions appeared to be heterogenous which leads to different spectra of the different ROIs within the tumour region (figure 4.24).

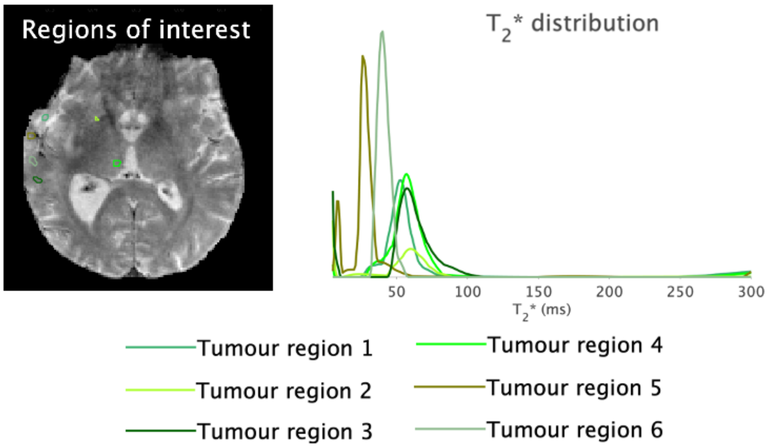

Figure 4.24 - T_2 distributions from 6 ROIs within the tumour for case 1. Vertical axis on T_2* distributions plots is intensity in arbitrary units.*

Case 2 – Glioma

A patient with glioma is presented in case 2. The pathological tissue shows hyperintensities in both T_2* weighted image and T_2* maps, separating it visibly well from the healthy tissue. The T_2* map shows a relatively uniform region in the central part of the tumour, which is surrounded by a region with the highest values of T_2*, and, more externally, by a region with similar intensity as in the centre. The maximum T_2* tumour peaks were found to be well separated from the corresponding contralateral maximum T_2* peaks, and the distributions of each selected tumour region and the corresponding normal appearing contralateral side were found to be statically different ($p<0.05$), according to Kolmogorov-Smirnov test. The average of the maximum T_2* peaks and the standard deviation of case 2 can be found in table 4.6.

Table 4.6 - Average ± standard deviation of the three T_2 peaks in the normal appearing and pathologic tissue for all used methods in case 2.*

	Average of maximum T_2* distribution peaks ± standard deviation (ms)	
	Normal appearing tissue	Pathologic tissue
QUTE	45.7 ± 6.0	90.0 ± 4.0
Gaussian filtered	47.7 ± 6.7	91.3 ± 5.7
PCA-based denoised	47.0 ± 4.6	94.0 ± 8.5
Sinc corrected	47.0 ± 4.6	94.3 ± 8.5
VSF $\sigma^{[1]}$	46.0 ± 5.6	87.0 ± 4.4
VSF $\sigma^{[2]}$	45.0 ± 15.6	86.3 ± 4.6

Unlike in the previous case, the gmT_2* of the tumour distributions in the glioma was found to range between 94 and 104 ms (instead of between 48 and 59 ms), which is considerably different of the gmT_2* found in the contralateral sides, which ranged between 40 and 55 ms (instead of between 40 and 51 ms), for data denoised with PCA (see table 7.3 of the appendix).

Additional areas belonging to the tumour mask were selected and the corresponding distributions can be seen in figure 4.25. The peaks of the distributions of the extra regions can be seen to be shifted towards higher T_2* values. A large variability in the distributions across the ROIs in the tumour region was found but all spectra seemed to be distinguishable from the ones found in normal appearing tissue, which was confirmed with Kolmogorov-Smirnov test ($p<0.05$).

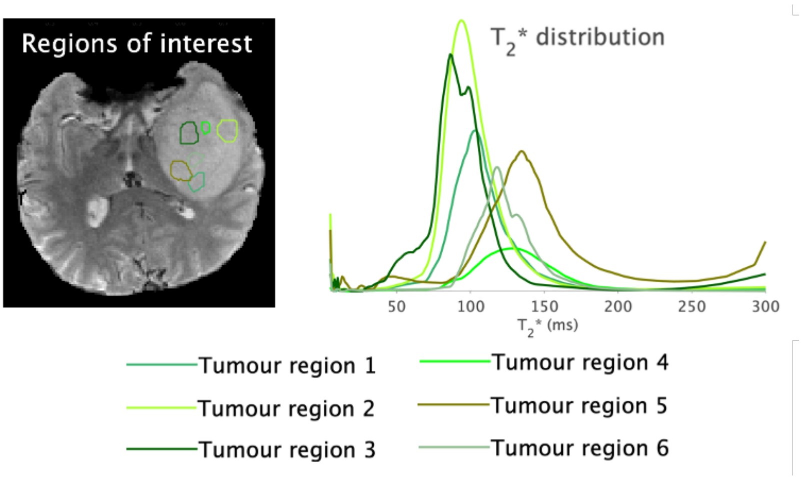

Figure 4.25 - T_2 distributions from 6 ROIs within the tumour for case 2. Vertical axis on T_2* distributions plots is intensity in arbitrary units.*

Case 3 - Oligoastrocytoma

Case 3 corresponds to a patient with an oligoastrocytoma superiorly limited by a region of water. The three selected regions correspond to the total area of the tumour mask and demonstrated a relatively uniform distribution of the T_2* values within the tumour region. The maximum peak values can be found in table 4.7 and the gmT_2* of the selected regions in the table 7.3 of the appendix. Both presented distinguishable distributions between pathologic and apparently healthy tissue, according to Kolmogorov-Smirnov test ($p<0.05$).

Table 4.7 - Average ± standard deviation of the three T_2 peaks in the normal appearing and pathologic tissue for all used methods in case 3.*

	Average of maximum T_2* distribution peaks ± standard deviation (ms)	
	Normal appearing tissue	Pathologic tissue
QUTE	43.3 ± 2.1	81.3 ± 6.4
Gaussian filtered	48.3 ± 2.9	81.7 ± 5.9
PCA-based denoised	45.7 ± 2.3	85.3 ± 7.6
Sinc corrected	44.7 ± 0.6	86.3 ± 9.0
VSF $\sigma^{[1]}$	39.7 ± 2.3	60.3± 42.9
VSF $\sigma^{[2]}$	39.7 ± 2.3	59.7 ± 42.4

Case 4 – Glioblastoma multiforme

A patient with glioblastoma multiforme is presented in case 4. In figure 4.23, it can be seen that some of the ROIs inside the tumour region showed higher T_2* peaks than normal appearing WM. The average of maximum T_2* peaks and standard deviation are reported in table 4.8.

Table 4.8 - Average ± standard deviation of the three T_2 peaks in the normal appearing and pathologic tissue for all used methods in case 4.*

	Average of maximum T_2* distribution peaks $\pm$ standard deviation (ms)	
	Normal appearing tissue	Pathologic tissue
QUTE	50.3 ± 2.1	63.7 ± 4.2
Gaussian filtered	48.7 ± 0.6	70.0 ± 4.4
PCA-based denoised	50.7 ± 2.5	68.3 ± 3.5
Sinc corrected	51.0 ± 4.0	71.0 ± 8.5
VSF $\sigma^{[1]}$	55.0 ± 7.5	65.0 ± 4.0
VSF $\sigma^{[2]}$	54.3 ± 7.5	64.0 ± 4.6

However, the T_2* map of this case depicts a very large affected area with very heterogenous T_2* values. The presence of necrotic tissue is also notorious (indicated by the blue arrow in figure 4.23). This fact may contribute to the huge heterogeneity in the obtained spectra of other ROIs. However, unlike in case 2, the glioblastoma multiform of case 4 showed multiple peaks scattered across a relatively wide range of the spectrum.

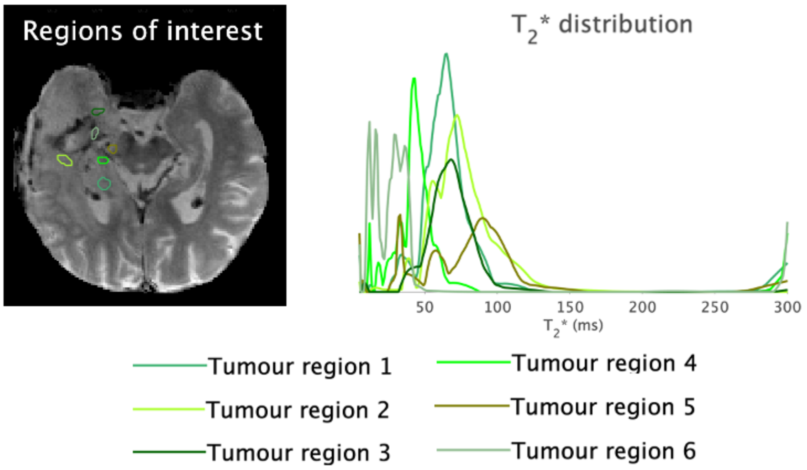

Figure 4.26 - T_2 distributions from 6 ROIs within the tumour for case 4. Vertical axis on T_2* distributions plots is intensity in arbitrary units.*

Case 5 - Oligodendroglioma

Case 5 corresponds to a patient with an oligodendroglioma in the right hemisphere, inferiorly to the lateral ventricle. The maximum T_2* peaks (see table 4.9) in both healthy and pathologic tissues appeared to be distinguishable for the selected and contralateral regions in figure 4.23. The distributions of each selected tumour region and the corresponding normal appearing contralateral side were found to be statically different ($p<0.05$), according to Kolmogorov-Smirnov test. Interestingly, some hyperintense regions in the T_2* map of this patient did not belong to the tumour mask, such as in the inferior region to the lateral ventricle in the left hemisphere. The selected ROIs in figure 4.23 reflect the main area of the tumour region and, therefore, only small differences in the spectrum were found in the remaining regions.

Table 4.9 - Average ± standard deviation of the three T_2 peaks in the normal appearing and pathologic tissue for all used methods in case 5.*

	Average of maximum T_2* distribution peaks $\pm$ standard deviation (ms)	
	Normal appearing tissue	Pathologic tissue
QUTE	43.3 ± 5.5	67.3 ± 9.3
Gaussian filtered	46.3 ± 3.1	68.0 ± 6.6
PCA-based denoised	42.7 ± 5.8	69.0 ± 6.2
Sinc corrected	42.7 ± 4.0	68.3 ± 4.5
VSF $\sigma^{[1]}$	44.3 ± 4.7	64.0 ± 8.7
VSF $\sigma^{[2]}$	43.3 ± 5.0	64.7 ± 8.1

Case 6 - Astrocytoma

The last case corresponds to an astrocytoma that exhibits a non-uniform tumour region, surrounded to the right by an oedema region, characterised by the increased T_2* values. Since the tumour is located adjacent to the long longitudinal fissure, and both hemispheres contain pathological tissue, the healthy regions presented were selected from known normal appearing areas far from the pathological regions. In figure 4.23, the distributions for each health region present a characteristic peak around the 57 ms while the peaks of pathologic tissue of the defined regions are between 82 and 93 ms. The average of maximum T_2* peaks and standard deviation are reported in table 4.10 for the non-corrected and corrected data.

Table 4.10 - Average ± standard deviation of the three T_2 peaks in the normal appearing and pathologic tissue for all used methods in case 6.*

	Average of maximum T_2* distribution peaks $\pm$ standard deviation (ms)	
	Normal appearing tissue	Pathologic tissue
QUTE	55.0 ± 1.7	83.3 ± 9.5
Gaussian filtered	58.0 ± 1.7	98.7 ± 4.0
PCA-based denoised	57.7 ± 3.2	87.3 ± 5.5
Sinc corrected	60.0 ± 7.8	95.7 ± 5.5
VSF $\sigma^{[1]}$	52.0 ± 1.7	82.7 ± 6.8
VSF $\sigma^{[2]}$	52.3 ± 2.5	80.7 ± 6.8

Apart from the necrotic region localised in the centre of the tumour region, the ROIs selected in figure 4.23 occupied the whole tumour area indicated by the PET-based mask. In figure 4.27 it can be seen the oedema spectra. The distribution is shifted to the right when compared with the spectrum of the tumour regions, indicating higher values in the oedema region. Similarly to the high T_2* values found in the CSF regions, this increase in T_2* reflects the higher concentrations of water present in the oedema region.

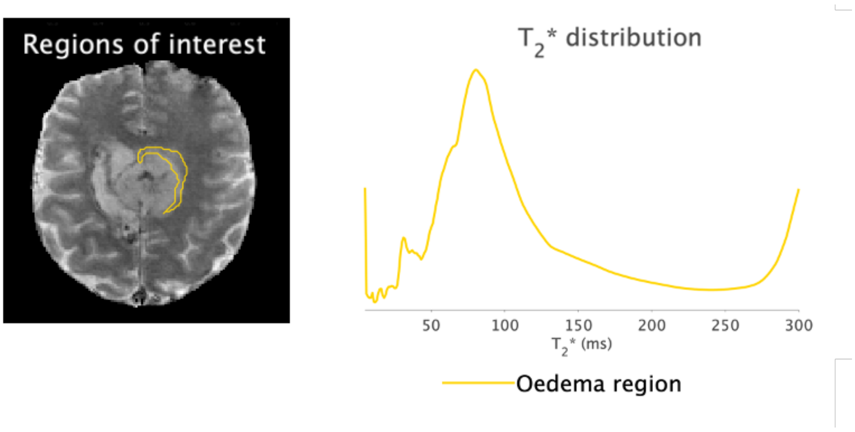

Figure 4.27 - T_2 distributions from the oedema region shown on the left. Vertical axis on T_2* distributions plots is intensity in arbitrary units.*

In most cases, it can be observed the presence of short T_2* components between 5 and 8 ms in all selected regions in different patients. These peaks might not be related with any morphologic or tissue aspect but, instead, with remaining noise in the data, which was reflected with higher amplitudes in the QUTE data. Normal appearing WM regions demonstrated quite uniform distributions across the patients with its maximum peak between 40-55 ms. Many of these WM voxels, presented an additional peak around 8-10 ms which might be associated with water trapped between the myelin cells. This short T_2* component was only observed in few tumour distributions, and therefore its study might be valuable to describe the aggressiveness of the tumours by the myelin cells being destroyed.

Most of the analysed tumours were shown to have tumour characteristic peaks that are shifted in there T_2* values towards the higher end of the spectrum. However, even when smaller regions are selected, the T_2* spectrum characteristic varies between different types of brain tumours and across patients.

The higher intensities in the T_2* maps did not completely match the ones given by the PET-based tumour masks. While PET is a measurement of metabolic activity, T_2* reflects the microstructure of the tissue. Therefore, PET may be better at distinguishing active tumour tissue, while T_2* will be better at identifying regions of heterogeneity in the tumour, as well as the level of damage caused by it.

The oedema distributions were found to vary as well, although in most of the cases oedema appeared to have higher T_2* peaks than the ones found in the tumour region, as would be expected due to the increased water content in this ROI.

To compare the effects of the noise reduction and the field correction methods in the T_2* spectra, the distributions of the same regions of the 6 cases presented for all methods can be found in figures 7.3 and 7.4 of the appendix. Overall, the T_2* spectra obtained with the Gaussian filtered data appeared to describe very smoothed distributions in all ROIs. However, when selecting smaller areas inside the tumour masks, the shape of the spectra seemed to be more similar to the original data than when compared to the distributions obtained with the remaining methods. Additionally, some of the short T_2* components that might include the typically myelin water peaks in the normal appearing regions were found to be supressed in the Gaussian filtering data (e.g. case 4 and case 5 in figure 7.4 of the appendix). The T_2* spectra obtained with the PCA-based denoised data exhibited well defined peaks. In most cases, the PCA-based denoised data revealed lower standard deviation between the maximum T_2* peaks relative to the other methods. The macroscopic field corrections are shown to have high influence in the T_2* distributions. The sinc correction method generated very noisy T_2* spectra, regardless the tumour type or region selected. All distributions of the small selected regions show multiple, apparently random peaks. The VSF on the other hand appeared to have a blunter effect in some of the T_2* spectra, in both healthy and pathologic tissue, and often shifted the peaks in there T_2* values towards the left side of the plots.

In summary, the study of multicomponent T_2* relaxation in brain tumours is a non-trivial task. It requires very precise estimation methods, and the applications of numerous corrections that are essential for the detection of small changes associated to the presence of SPIO particles over susceptibility induced macroscopic field distortions. In this thesis, the used methods for correction of the static magnetic field revealed to fail, and, therefore, the detection of such small changes was not possible.

4.3 Water content

The effect of Gaussian filtering and PCA-based denoising on water content is shown for a slice with no tumour evidence in figure 4.28.

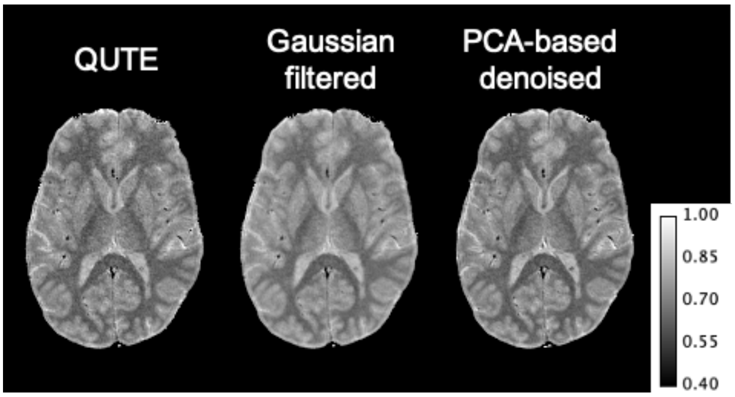

Figure 4.28 – Water content maps of a slice with no tumour evidence, for the different denoising methods.

Figure 4.29 shows the obtained water content histograms with the different methods from the same slice presented in figure 4.28. It can be seen that the brain histogram shows a bi-modal distribution of the white and grey matter. The bi-modal distributions are highlighted in the PCA-based denoising and VSF $\sigma^{[2]}$.

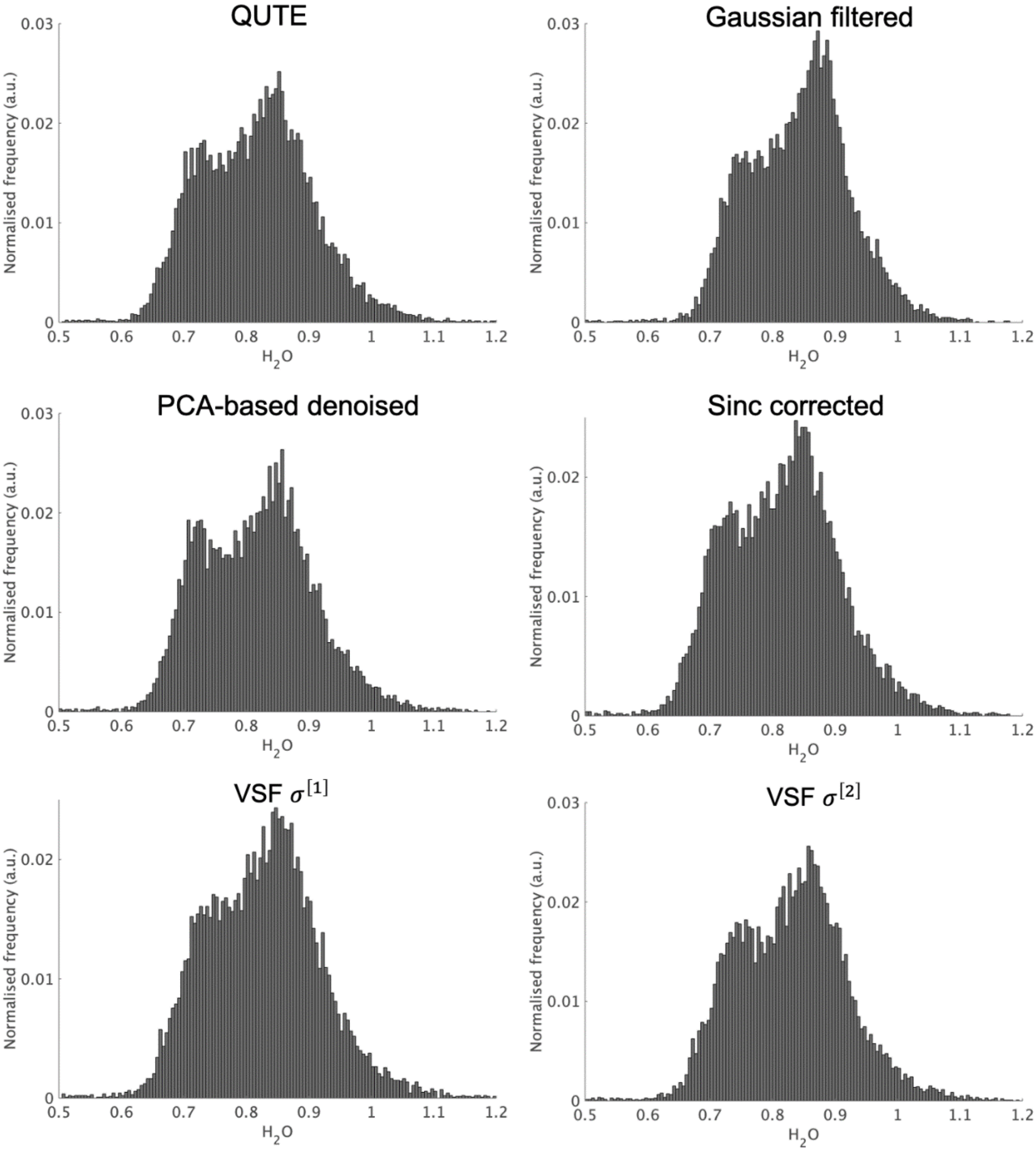

Figure 4.29 – Normalised histograms of a normal appearing slice showing the bi-modal distribution of WM and GM, characteristic of water content maps, for the different methods.

Table 4.11 presents mean and standard deviation of the water content values expressed as fraction of water for each tissue type and method separately. Gaussian filtered and both VSF data revealed the highest standard deviation values across the different ROIs. In most cases, the water content in the tumour region was found to be close to the water content in the GM contralateral side. The water content in the oedema regions was found to be lower than in the tumour regions. The variability of water content in tumour regions was found to be higher than in both WM and GM regions. Figure 4.30 shows an example of the found distributions of each ROI for data processed with PCA-based denoising.

Kruskal-Wallis test revealed statistically significant differences between the medians of the WM and GM groups in all methods used ($p<0.05$). The differences between WM/tumour and WM/CSF were significant across the methods except with VSF $\sigma^{[1]}$ and Gaussian filtering, respectively. Unlike reported in the literature [8], no significant differences were found between the tumour and oedema region.

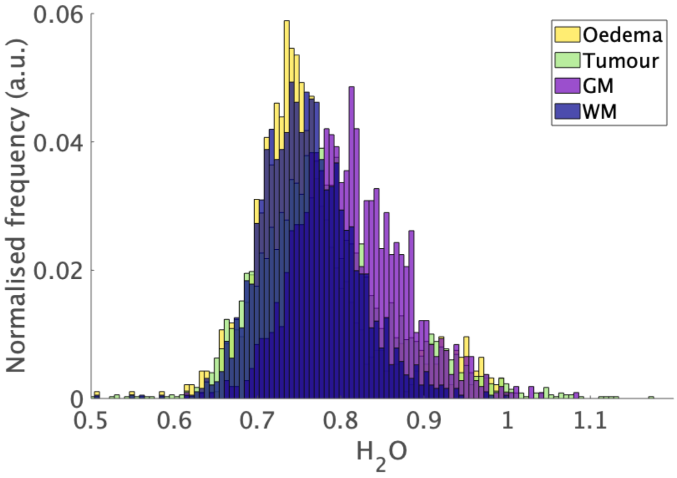

Figure 4.30 - Normalised water content histogram of a representative patient for the different ROIs, with data corrected with PCA-based denoising.

In the literature [48], water content values were reported for five glioblastoma patients with an average of 71.4 %, 84.3% and 84.5% in the WM, GM and tumour regions, respectively. Some years later, a report on eight glioma patients revealed that the average water content was 69%, 83%, 84% and 79% in the WM, GM, tumour and oedema regions, respectively [8]. Therefore, the differences found between the average water content on the literature and the values reported in table 4.11 might result from the heterogenous sample (different tumours types are included).

Table 4.11 – Mean ± standard deviation of the water content values over all patients, for each tissue type and method separately.

	QUTE	Gaussian filtered	PCA-based denoised	Sinc corrected	VSF $\sigma^{[1]}$	VSF $\sigma^{[2]}$
WM	0.762 ± 0.029	0.834 ± 0.124	0.757 ± 0.029	0.763 ± 0.030	0.873 ± 0.156	0.830 ± 0.139
GM	0.808 ± 0.034	0.869 ± 0.114	0.802 ± 0.038	0.804 ± 0.043	0.918 ± 0.132	0.872 ± 0.123
CSF	0.806 ± 0.115	0.822 ± 0.175	0.792 ± 0.123	0.788 ± 0.126	0.904 ± 0.150	0.867 ± 0.138
Tumour	0.798 ± 0.041	0.858 ± 0.118	0.792 ± 0.043	0.797 ± 0.043	0.903 ± 0.139	0.859 ± 0.117
Oedema	0.775 ± 0.070	0.829 ± 0.116	0.772 ± 0.071	0.773 ± 0.080	0.872 ± 0.156	0.838 ± 0.140

Figure 4.31 shows the scatter plots of all voxels for the different ROIs of water content vs gmT_2* for the 6 cases previously presented in section 4.2.3. The WM and GM regions appeared to have a consistent area across the patients, while the tumour and oedema regions are characterised with higher variability in both axes. However, some patients demonstrated distinct distributions between tumour tissue and the distributions of apparently normal tissue, which might be useful for tumour characterisation.

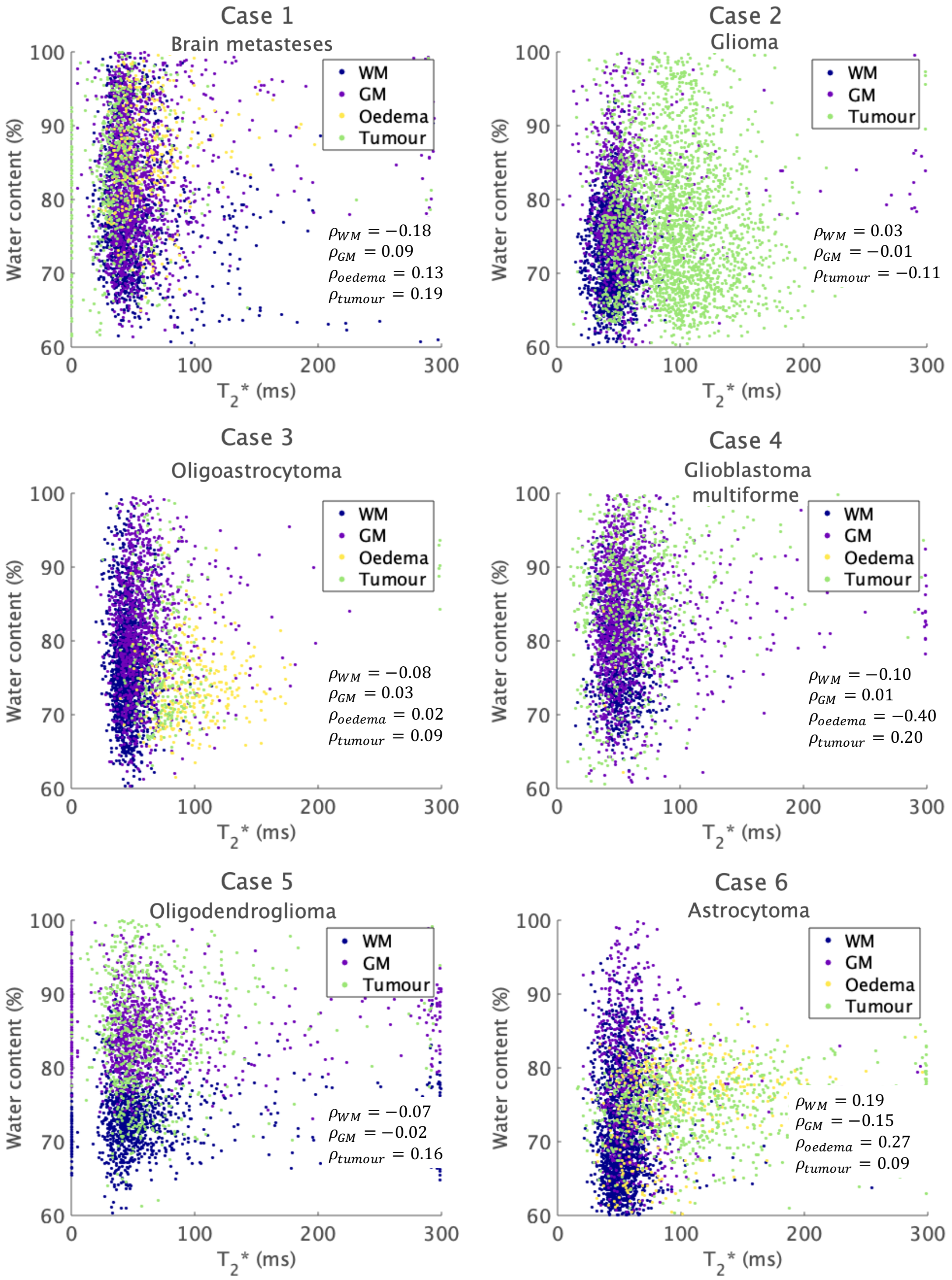

Figure 4.31 - Water content vs T_2 scatter plots for the 6 cases previously showed in section 4.2.3, for data corrected with PCA-based denoising and the corresponding correlation coefficients (ρ) for each ROI.*

In summary, the accuracy of water content mapping is highly dependent of the MR signal and on the applied correction methods [15]. Water content in apparently healthy slices of the brain shows a bi-modal distribution, similar to the ones found in previous studies [8], [59]. Across all patients, the T_2* values in the tumour regions were found to have larger variability than WM and GM regions, while the water content values have been shown to have similar variability between tumour, WM and GM tissue.

T_2* is known to have longer components in pure water due to the fast movement of water molecules. Accordingly, the slower motion of water molecules is associated to shorter T_2* components. Therefore, in this thesis, the relation between water content and T_2* values was studied, although no correlation between the parameters was found.

5. Conclusion

In this thesis, the topic of qMRI using a mGRE sequence was investigated, from which tissue T_2* and water content were estimated. qMRI provides several advantages compared to qualitative MRI since the pursuit of acquiring scanner independent tissue characteristics provides with information regarding the integrity of the tissue, an assessment that may be valuable to diagnose the type of tumour, evaluate tumour changes and/or response to therapy in a non-invasive way. However, qMRI is a challenging task mainly due to its prolonged acquisition times as well as it demands high accuracy and precision of the used processing methods for the estimation of the parameters.

The results presented throughout this dissertation, show that the stated aims have been fulfilled. Briefly, the goals of this work included studying the influence of denoising and magnetic field inhomogeneity correction, characterising the brain with mono and multi-exponential models, studying tumour characteristic peaks, and studying the relation between water content and T_2*.

First, the effects of noise and B_0 inhomogeneities in the 2D experiments were considered and different correction methods were applied. Noise reduction was achieved with the application of Gaussian filtering and PCA-based denoising, separately. The influence of susceptibility-induced field distortions was expected to be compensated with the application of a sinc modulation correction as well as by the application of a VSF algorithm. This was, however, not verified and the high S_0 and short T_2* values in regions close to interfaces with high B_0 inhomogeneities were not corrected to their normal tissue values. Particularly, further investigation can be done with the VSF algorithm by increasing the number of neighbouring voxels. If macroscopic magnetic field inhomogeneity correction methods are optimised for 2D experiments, their performance together with noise reduction methods are of very relevant interest.

Second, we confirmed that voxels exhibit multiple compartments that can be described by their specific relaxation time and compared the results with the ones obtained with a mono-exponential approach, across the different ROIs. Multi-exponential relaxometry was performed by a regularised version of the NNLS algorithm since the estimation of the distribution of relaxation times within each voxel is an ill-posed problem. The L-curve method was implemented to define the ideal regularisation range but revealed to fail at over-smoothing the final solutions. Due to the limited time of this study, no additional criteria were used to find the ideal regularisation range. Future studies could condensate the information of the different criteria, which would be valuable in many multi-exponential relaxometry studies.

Third, multiple T_2* components in brain tumours were studied. Challenges arise by the fact that each patient was confirmed to have unique and highly heterogeneous quantitative T_2* tumour characteristics, also visible on the conventional T_2* weighed images. We presented significant differences between the distributions of pathological tissue regions and the corresponding contralateral distributions of normal appearing tissue. However, these regions were manually drawn from inside the PET-based tumour mask, which in itself has some limitations. Additionally, the T_2* distributions might be biased since both macroscopic field inhomogeneity correction methods revealed poor results in the 2D experiments. In line with this, future work could include the comparison between T_2 and T_2* distributions in order to evaluate the performance of B_0 inhomogeneity correction methods, and to study small changes that might be associated with the presence of paramagnetic particles (but not associated with field distortions).

In this thesis, due to the small sample of patients and because not all tumours were histologically confirmed, the study was not taken either by the grade, either by the type of the tumour, which is probably related to the large variability found within the tumour regions and across patients. Additionally, the tumour masks are highly depend on the accuracy of PET-MR coregistration and extent of partial volume effects [8], which is an unavoidable limitation.

Finally, water content values were calculated from the S_0 maps and were demonstrated to not be correlated with T_2* values obtained with the regularised NNLS algorithm. Future work in this field could include the implementation of multiple compartment models on water content in the brain to correlate possible distinct water peaks with the different peaks found in the T_2* distributions.

6. References

[1] "Cancer." [Online]. Available: https://www.who.int/news-room/fact-sheets/detail/cancer [Accessed: 20-Mar-2020].

[2] "A Patient's Guide to Brain Diseases and Other Neurological Conditions." [Online]. Available: https://health.usnews.com/conditions/brain-disease [Accessed: 20-Mar-2020].

[3] "Globocan 2018 – Global Cancer Observatory." [Online]. Available: https://www.cancer.org/cancer/cancer-causes/genetics/genes-and-cancer/oncogenes-tumor-suppressor-genes.html [Accessed: 21-Feb-2020].

[4] S. C. L. Deoni, "Quantitative Relaxometry of the Brain:," *Topics in Magnetic Resonance Imaging*, vol. 21, no. 2, pp. 101–113, Apr. 2010, doi: 10.1097/RMR.0b013e31821e56d8.

[5] M. Nilsson, E. Englund, F. Szczepankiewicz, D. van Westen, and P. C. Sundgren, "Imaging brain tumour microstructure," *NeuroImage*, vol. 182, pp. 232–250, Nov. 2018, doi: 10.1016/j.neuroimage.2018.04.075.

[6] K. P. Whittall and A. L. MacKay, "Quantitative interpretation of NMR relaxation data," *Journal of Magnetic Resonance (1969)*, vol. 84, no. 1, pp. 134–152, Aug. 1989, doi: 10.1016/0022-2364(89)90011-5.

[7] M. Zimmermann *et al.*, "Multi-Exponential Relaxometry Using l1-Regularized Iterative NNLS (MERLIN) With Application to Myelin Water Fraction Imaging," *IEEE Trans. Med. Imaging*, vol. 38, no. 11, pp. 2676–2686, Nov. 2019, doi: 10.1109/TMI.2019.2910386.

[8] A. M. Oros-Peusquens, R. Loução, M. Zimmermann, K.-J. Langen, and N. J. Shah, "Methods for molecular imaging of brain tumours in a hybrid MR-PET context: Water content, T_2*, diffusion indices and FET-PET," *Methods*, vol. 130, pp. 135–151, Nov. 2017, doi: 10.1016/j.ymeth.2017.07.025.

[9] K. P. Whittall, A. L. MacKay, and D. K. B. Li, "Are mono-exponential fits to a few echoes sufficient to determine T_2 relaxation for in vivo human brain?," 1999, doi: 10.1002/(sici)1522-2594(199906)41:6<1255::aid-mrm23>3.0.co;2-i.

[10] A. Mackay, K. Whittall, J. Adler, D. Li, D. Paty, and D. Graeb, "In vivo visualization of myelin water in brain by magnetic resonance," *Magn. Reson. Med.*, vol. 31, no. 6, pp. 673–677, Jun. 1994, doi: 10.1002/mrm.1910310614.

[11] X. Li, P. van Gelderen, P. Sati, J. A. de Zwart, D. S. Reich, and J. H. Duyn, "Detection of demyelination in multiple sclerosis by analysis of T_2* relaxation at 7 T," *NeuroImage: Clinical*, vol. 7, pp. 709–714, 2015, doi: 10.1016/j.nicl.2015.02.021.

[12] D. Hwang, D.-H. Kim, and Y. P. Du, "In vivo multi-slice mapping of myelin water content using T2* decay," *NeuroImage*, vol. 52, no. 1, pp. 198–204, Aug. 2010, doi: 10.1016/j.neuroimage.2010.04.023.

[13] X. Yang, S. Sammet, P. Schmalbrock, and M. V. Knopp, "Postprocessing correction for distortions in T2* decay caused by quadratic cross-slice B0 inhomogeneity," *Magn. Reson. Med.*, vol. 63, no. 5, pp. 1258–1268, May 2010, doi: 10.1002/mrm.22316.

[14] H. Dahnke and T. Schaeffter, "Limits of detection of SPIO at 3.0 T using T_2* relaxometry," *Magn. Reson. Med.*, vol. 53, no. 5, pp. 1202–1206, May 2005, doi: 10.1002/mrm.20435.

[15] N. J. Shah, V. Ermer, and A.-M. Oros-Peusquens, "Measuring the Absolute Water Content of the Brain Using Quantitative MRI," in *Magnetic Resonance Neuroimaging*, vol. 711, M. Modo and J. W. M. Bulte, Eds. Totowa, NJ: Humana Press, 2011, pp. 29–64.

[16] M. M. J. J. Modo and J. W. M. Bulte, Eds., *Magnetic resonance neuroimaging: methods and protocols*. New York: Humana Press, 2011.

[17] S. G. Hormuzdi, M. A. Filippov, G. Mitropoulou, H. Monyer, and R. Bruzzone, "Electrical synapses: a dynamic signaling system that shapes the activity of neuronal networks," *Biochimica et Biophysica Acta (BBA) - Biomembranes*, vol. 1662, no. 1–2, pp. 113–137, Mar. 2004, doi: 10.1016/j.bbamem.2003.10.023.

[18] R. Dringen, "Oxidative and Antioxidative Potential of Brain Microglial Cells," *Antioxidants & Redox Signaling*, vol. 7, no. 9–10, pp. 1223–1233, Sep. 2005, doi: 10.1089/ars.2005.7.1223.

[19] R. M. Stassart, W. Möbius, K.-A. Nave, and J. M. Edgar, "The Axon-Myelin Unit in Development and Degenerative Disease," *Front. Neurosci.*, vol. 12, p. 467, Jul. 2018, doi: 10.3389/fnins.2018.00467.

[20] M. Simons and K.-A. Nave, "Oligodendrocytes: Myelination and Axonal Support," *Cold Spring Harb Perspect Biol*, vol. 8, no. 1, p. a020479, Jan. 2016, doi: 10.1101/cshperspect.a020479.

[21] A. L. MacKay and C. Laule, "Magnetic Resonance of Myelin Water: An in vivo Marker for Myelin," *BPL*, vol. 2, no. 1, pp. 71–91, Dec. 2016, doi: 10.3233/BPL-160033.

[22] C.S. Raine "Morphology of myelin and myelination". In: Morell P., editor. Myelin. 2nd Edition ed. New York: Plenum Press, 1984.

[23] "Brain tumours: an introduction." [Online]. Available: https://mayfieldclinic.com/pe-braintumor.htm [Accessed: 22-Mar-2020].

[24] "Oncogenes and tumor suppressor genes." [Online]. Available: https://www.cancer.org/cancer/cancer-causes/genetics/genes-and-cancer/oncogenes-tumor-suppressor-genes.html [Accessed: 22-Mar-2020].

[25] "What Causes Chronic Myeloid Leukemia." [Online]. Available: https://www.cancer.org/cancer/chronic-myeloid-leukemia/causes-risks-prevention/what-causes.html [Accessed: 26-Mar-2020].

[26] A. Gupta and T. Dwivedi, "A Simplified Overview of World Health Organization Classification Update of Central Nervous System Tumors 2016," *Journal of Neurosciences in Rural Practice*, vol. 08, no. 04, pp. 629–641, Oct. 2017, doi: 10.4103/jnrp.jnrp_168_17.

[27] D. N. Louis *et al.*, "The 2007 WHO Classification of Tumours of the Central Nervous System," *Acta Neuropathol*, vol. 114, no. 2, pp. 97–109, Jul. 2007, doi: 10.1007/s00401-007-0243-4.

[28] D. N. Louis *et al.*, "The 2016 World Health Organization Classification of Tumors of the Central Nervous System: a summary," *Acta Neuropathol*, vol. 131, no. 6, pp. 803–820, Jun. 2016, doi: 10.1007/s00401-016-1545-1.

[29] A. Gupta and T. Dwivedi, "A Simplified Overview of World Health Organization Classification Update of Central Nervous System Tumors 2016," *Journal of Neurosciences in Rural Practice*, vol. 08, no. 04, pp. 629–641, Oct. 2017, doi: 10.4103/jnrp.jnrp_168_17.

[30] T. N. Seyfried and L. C. Huysentruyt, "On the Origin of Cancer Metastasis," p. 37, 2014.

[31] "Diagnostic imaging." [Online]. Available: https://www.who.int/diagnostic_imaging/en/ [Accessed: 14-Apr-2020].

[32] D. G. Nishimura, Principles of magnetic resonance imaging. Standford Univ., 2010. Chapter 4, p. 55-65.

[33] R. W. Brown, Y.-C. N. Cheng, E. M. Haacke, M. R. Thompson, and R. Venkatesan, Eds., *Magnetic Resonance Imaging: Physical Principles and Sequence Design*. Chichester, UK: John Wiley & Sons Ltd, 2014.

[34] D. G. Nishimura, Principles of magnetic resonance imaging. Standford Univ., 2010. Chapter 6, p. 107-120.

[35] D. G. Nishimura, Principles of magnetic resonance imaging. Standford Univ., 2010. Chapter 5, p. 67-98.

[36] D. Moratal, A. Valles-Luch, L. Marti-Bonmati, and M. Brummer, “k-Space tutorial: an MRI educational tool for a better understanding of k-space,” *Biomed. Imaging Interv. J.*, vol. 4, no. 1, Jan. 2008, doi: 10.2349/biij.4.1.e15.

[37] F. Liu, Y. Duan, B. S. Peterson, and A. Kangarlu, “Compressed sensing MRI combined with SENSE in partial *k* -space,” *Phys. Med. Biol.*, vol. 57, no. 21, pp. N391–N403, Nov. 2012, doi: 10.1088/0031-9155/57/21/N391.

[38] C. Malamateniou *et al.*, “Motion-Compensation Techniques in Neonatal and Fetal MR Imaging,” *AJNR Am J Neuroradiol*, vol. 34, no. 6, pp. 1124–1136, Jun. 2013, doi: 10.3174/ajnr.A3128.

[39] B. A. Jung and M. Weigel, “Spin echo magnetic resonance imaging,” *J. Magn. Reson. Imaging*, vol. 37, no. 4, pp. 805–817, Apr. 2013, doi: 10.1002/jmri.24068.

[40] G. B. Chavhan, P. S. Babyn, B. Thomas, M. M. Shroff, and E. M. Haacke, “Principles, Techniques, and Applications of T2*-based MR Imaging and Its Special Applications,” *RadioGraphics*, vol. 29, no. 5, pp. 1433–1449, Sep. 2009, doi: 10.1148/rg.295095034.

[41] D. G. Nishimura, Principles of magnetic resonance imaging. Standford Univ., 2010. Chapter 7.

[42] H. Gudbjartsson and S. Patz, “The rician distribution of noisy mri data,” *Magn. Reson. Med.*, vol. 34, no. 6, pp. 910–914, Dec. 1995, doi: 10.1002/mrm.1910340618.

[43] “MR Quality Control: SNR.” [Online]. Available: http://mriquestions.com/signal-to-noise.html [Accessed: 10-Sep-2020].

[44] D. Ray, D. Dutta Majumder, and A. Das, “Noise reduction and image enhancement of MRI using adaptive multiscale data condensation,” in *2012 1st International Conference on Recent Advances in Information Technology (RAIT)*, Dhanbad, India, Mar. 2012, pp. 107–113, doi: 10.1109/RAIT.2012.6194489.

[45] L. Chandrashekar and A. Sreedevi, “Assessment of non-linear filters for MRI images,” in *2017 Second International Conference on Electrical, Computer and Communication Technologies (ICECCT)*, Coimbatore, Feb. 2017, pp. 1–5, doi: 10.1109/ICECCT.2017.8117852.

[46] S. Tania and R. Rowaida, “A Comparative Study of Various Image Filtering Techniques for Removing Various Noisy Pixels in Aerial Image,” *IJSIP*, vol. 9, no. 3, pp. 113–124, Mar. 2016, doi: 10.14257/ijsip.2016.9.3.10.

[47] S. Suhas and C. R. Venugopal, “MRI image preprocessing and noise removal technique using linear and nonlinear filters,” in *2017 International Conference on Electrical, Electronics, Communication, Computer, and Optimization Techniques (ICEEECCOT)*, Mysuru, Dec. 2017, pp. 1–4, doi: 10.1109/ICEEECCOT.2017.8284595.

[48] P. Bankhead, “Analyzing fluorescence microscopy images with ImageJ,” 2014.

[49] Jolliffe I. “Principal Component Analysis.” In: Lovric M. (eds) International Encyclopedia of Statistical Science. Springer, Berlin, Heidelberg. 2011. https://doi.org/10.1007/978-3-642-04898-2_455

[50] W. Renkjumnong, “SVD and PCA in Image Processing,” 2007.

[51] M. D. Does *et al.*, “Evaluation of PCA Image Denoising on Multi -Exponential MRI Relaxometry,” p. 30.

[52] B. Mwangi, T. S. Tian, and J. C. Soares, “A Review of Feature Reduction Techniques in Neuroimaging,” *Neuroinform*, vol. 12, no. 2, pp. 229–244, Apr. 2014, doi: 10.1007/s12021-013-9204-3.

[53] T. Tr, “Dimensionality Reduction: A Comparative Review,” 2009.

[54] F. Bunea, Y. She, H. Ombao, A. Gongvatana, K. Devlin, and R. Cohen, “Penalized least squares regression methods and applications to neuroimaging,” *NeuroImage*, vol. 55, no. 4, pp. 1519–1527, Apr. 2011, doi: 10.1016/j.neuroimage.2010.12.028.

[55] D. A. Yablonskiy, A. L. Sukstanskii, J. Luo, and X. Wang, “Voxel spread function method for correction of magnetic field inhomogeneity effects in quantitative gradient-echo-based MRI:

Correction of Magnetic Field Inhomogeneity Effects,” *Magn. Reson. Med.*, vol. 70, no. 5, pp. 1283–1292, Nov. 2013, doi: 10.1002/mrm.24585.

[56] F. Keil, K. J. Langen, H. Herzog, G. Stoffels, C. Weiss, and N. J. Shah, “Fast and accurate water content and T2∗ mapping in brain tumours localised with FET-PET,” *Nuclear Instruments and Methods in Physics Research Section A: Accelerators, Spectrometers, Detectors and Associated Equipment*, vol. 734, pp. 185–190, Jan. 2014, doi: 10.1016/j.nima.2013.09.045.

[57] K. P. Whittall, A. L. Mackay, D. A. Graeb, R. A. Nugent, D. K. B. Li, and D. W. Paty, “In vivo measurement ofT2 distributions and water contents in normal human brain,” *Magn. Reson. Med.*, vol. 37, no. 1, pp. 34–43, Jan. 1997, doi: 10.1002/mrm.1910370107.

[58] C. Laule *et al.*, “Characterization of brain tumours with spin–spin relaxation: pilot case study reveals unique T 2 distribution profiles of glioblastoma, oligodendroglioma and meningioma,” *J Neurol*, vol. 264, no. 11, pp. 2205–2214, Nov. 2017, doi: 10.1007/s00415-017-8609-6.

[59] E. Alonso-Ortiz, I. R. Levesque, and G. B. Pike, “Multi-gradient-echo myelin water fraction imaging: Comparison to the multi-echo-spin-echo technique: MGRE-MWF Imaging: Comparison to the MESE-MWF Technique,” *Magn. Reson. Med.*, vol. 79, no. 3, pp. 1439–1446, Mar. 2018, doi: 10.1002/mrm.26809.

[60] A.-M. Oros-Peusquens, R. Loução, Z. Abbas, V. Gras, M. Zimmermann, and N. J. Shah, “A Single-Scan, Rapid Whole-Brain Protocol for Quantitative Water Content Mapping With Neurobiological Implications,” *Front. Neurol.*, vol. 10, p. 1333, Dec. 2019, doi: 10.3389/fneur.2019.01333.

[61] K. J. Friston, Ed., *Statistical parametric mapping: the analysis of funtional brain images*, 1st ed. Amsterdam ; Boston: Elsevier/Academic Press, 2007.

[62] J. Ashburner and K. J. Friston, “Unified segmentation,” *NeuroImage*, vol. 26, no. 3, pp. 839–851, Jul. 2005, doi: 10.1016/j.neuroimage.2005.02.018.

[63] D. M. D. Abràmoff, “Image Processing with ImageJ,” 2004.

[64] Van Rossum, G. and Drake, F.L., 2009, *Python 3 Reference Manual*, Scotts Valley, CA: CreateSpace.

[65] M. Bydder and J. Du, “Noise reduction in multiple-echo data sets using singular value decomposition,” *Magnetic Resonance Imaging*, vol. 24, no. 7, pp. 849–856, Sep. 2006, doi: 10.1016/j.mri.2006.03.006.

[66] MATLAB, 2018. *9.7.0.1190202 (R2019b)*, Natick, Massachusetts: The MathWorks Inc.

[67] V. G. Kemper, “Decomposition of signal decay and recovery of T2* information in quantitative MRI,” 2011.

[68] P. C. Hansen, “The L-curve and its use in the numerical treatment of inverse problems,” p. 24.

[69] IBM Corp. Released 2019. IBM SPSS Statistics for Windows, Version 26.0. Armonk, NY: IBM Corp.

7. Appendix

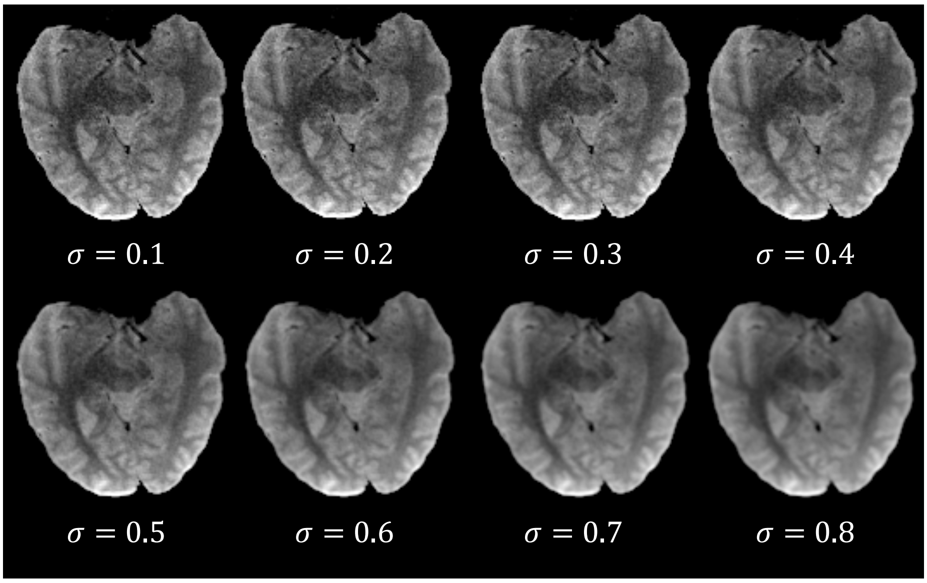

Figure 7.1 – Visual effects of increasing σ *in Gaussian filtering.*

Table 7.1 - Summary of the p-values between all ROI for each applied method in the mono-exponential relaxometry approach.

	QUTE	Gaussian filtered	PCA-based denoised	Sinc corrected	VSF $\sigma^{[1]}$	VSF $\sigma^{[2]}$
WM-GM	0.272	0.247	0.321	0.227	0.865	0.820
WM- Tumour	0.747	0.276	0.085	0.089	0.031	0.019
WM-Oedema	0.017	0.117	0.028	0.017	0.022	0.013
WM-CSF	0.000	0.000	0.000	0.000	0.000	0.000
GM-Tumour	0.004	0.025	0.007	0.004	0.020	0.019
GM-Oedema	0.001	0.009	0.002	0.000	0.014	0.013
GM-CSF	0.000	0.000	0.000	0.000	0.000	0.000
Tumour-Oedema	0.442	0.562	0.527	0.396	0.730	0.716
Tumour-CSF	0.000	0.000	0.001	0.000	0.000	0.000
Oedema-CSF	0.015	0.001	0.012	0.007	0.000	0.000

Table 7.2 - Summary of the p-values between all ROI for each applied method in the multi-exponential relaxometry approach.

	QUTE	Gaussian filtered	PCA-based denoised	Sinc corrected	VSF $\sigma^{[1]}$	VSF $\sigma^{[2]}$
WM-GM	0.050	0.024	0.080	0.025	0.006	0.092
WM- Tumour	0.000	0.000	0.000	0.000	0.000	0.000
WM-Oedema	0.000	0.000	0.000	0.000	0.000	0.000
WM-CSF	0.000	0.000	0.000	0.000	0.000	0.000
GM-Tumour	0.003	0.010	0.005	0.006	0.002	0.011
GM-Oedema	0.000	0.001	0.000	0.001	0.004	0.023
GM-CSF	0.000	0.000	0.000	0.000	0.000	0.000
Tumour-Oedema	0.364	0.300	0.295	0.389	0.978	1.000
Tumour-CSF	0.000	0.000	0.000	0.000	0.000	0.000
Oedema-CSF	0.003	0.004	0.003	0.001	0.000	0.002

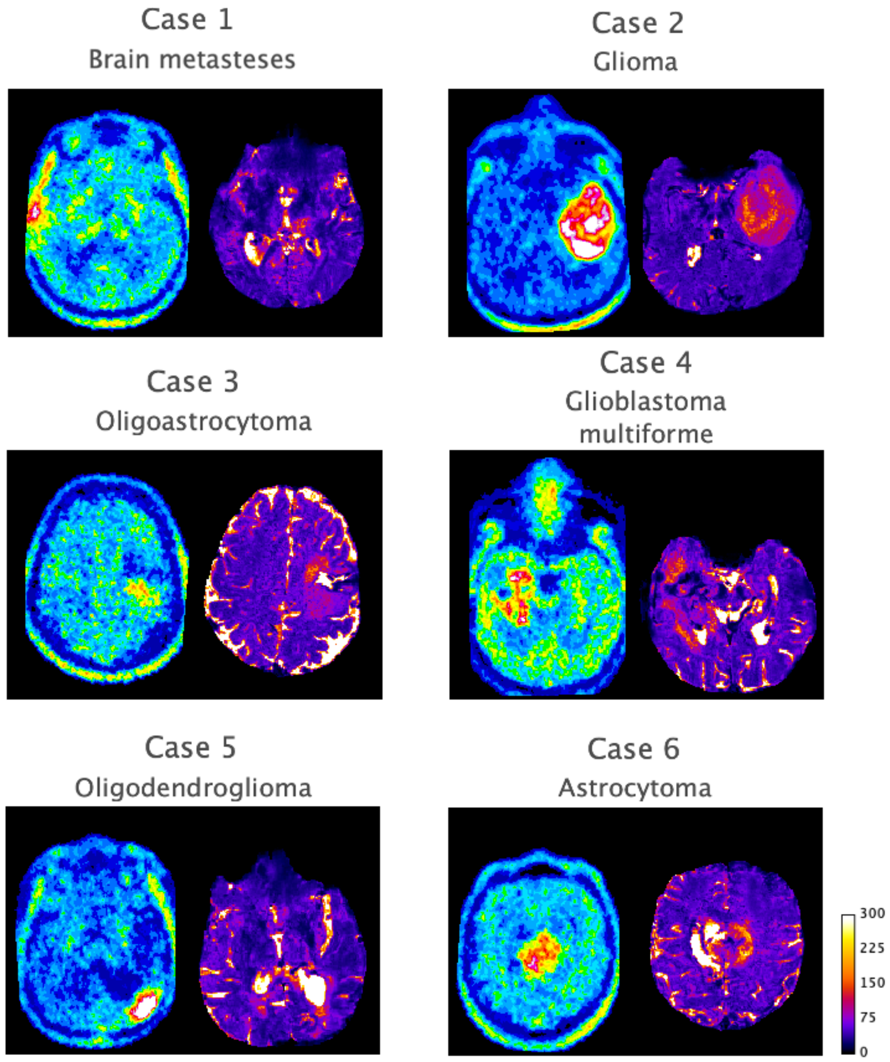

Case 1
Brain metasteses

Case 2
Glioma

Case 3
Oligoastrocytoma

Case 4
Glioblastoma multiforme

Case 5
Oligodendroglioma

Case 6
Astrocytoma

Figure 7.2 - On the left, the PET images and, on the right, the gmT_2 map of the 6 tumour cases.*

Table 7.3 – Geometric mean T_2 of the manually selected regions in the original and corrected data of each tumour case. ‘T.region’ corresponds to a tumour region and ‘H. region’ to the normal appearing contralateral region.*

		QUTE	Gaussian filtered	PCA-based denoised	Sinc corrected	VSF $\sigma^{[1]}$	VSF $\sigma^{[2]}$
	Region	gmT_2* (ms)					
Case 1 (Brain metasteses)	T. region 1	58.96	66.07	59.04	59.24	57.00	57.10
	T. region 2	46.45	39.28	47.81	45.44	48.29	49.06
	T. region 3	52.08	47.34	52.09	51.14	47.96	47.81
	H. region 1	42.03	52.76	42.07	42.51	41.22	40.44
	H. region 2	38.54	35.91	39.73	35.52	39.67	39.51
	H. region 3	50.48	53.26	51.27	50.56	48.92	48.97
Case 2 (Glioma)	T. region 1	105.54	105.27	104.20	103.44	99.21	99.23
	T. region 2	98.40	98.08	97.45	97.80	96.89	97.09
	T. region 3	94.97	98.01	94.27	95.10	89.28	89.35
	H. region 1	39.43	40.19	39.78	39.16	39.96	40.00
	H. region 2	47.67	47.32	47.68	48.20	50.82	50.84
	H. region 3	55.03	53.70	55.02	55.34	54.63	54.75
Case 3 (Oligoastrocytoma)	T. region 1	79.11	81.54	79.76	79.14	78.03	77.98
	T. region 2	91.08	88.74	91.23	89.70	86.40	86.85
	T. region 3	82.96	83.02	83.56	81.62	75.43	75.68
	H. region 1	47.50	50.56	48.24	47.64	44.54	44.40
	H. region 2	47.27	51.22	48.20	47.52	42.94	42.96
	H. region 3	60.18	63.86	61.10	60.61	54.19	54.39
Case 4 (Glioblastoma multiforme)	T. region 1	66.04	76.61	66.62	66.38	69.15	68.74
	T. region 2	73.75	75.16	73.47	73.63	71.21	71.55
	T. region 3	66.05	65.08	66.30	71.07	67.69	68.10
	H. region 1	48.50	49.49	48.85	47.75	50.02	50.30
	H. region 2	41.86	44.23	42.35	41.40	43.34	43.33
	H. region 3	51.60	50.17	51.83	53.71	58.24	59.40
Case 5 (Oligodendroglioma)	T. region 1	78.55	73.18	78.54	77.67	76.23	76.35
	T. region 2	93.10	100.16	92.94	92.92	87.76	87.17
	T. region 3	64.51	65.24	64.73	64.28	61.38	61.50
	H. region 1	48.83	50.43	49.30	48.66	50.67	50.54
	H. region 2	48.51	50.24	49.02	49.01	50.00	49.89
	H. region 3	51.45	54.34	52.07	51.83	51.40	51.15
Case 6 (Astrocytoma)	T. region 1	88.36	106.02	88.35	87.96	86.44	86.67
	T. region 2	91.14	106.53	90.90	89.67	95.85	96.23
	T. region 3	102.95	106.03	103.02	102.37	92.87	93.25
	H. region 1	58.37	61.34	59.32	58.21	56.19	56.28
	H. region 2	51.06	51.09	53.26	50.66	48.30	48.20

H. region 3	54.80	54.39	55.17	54.28	47.93	47.97

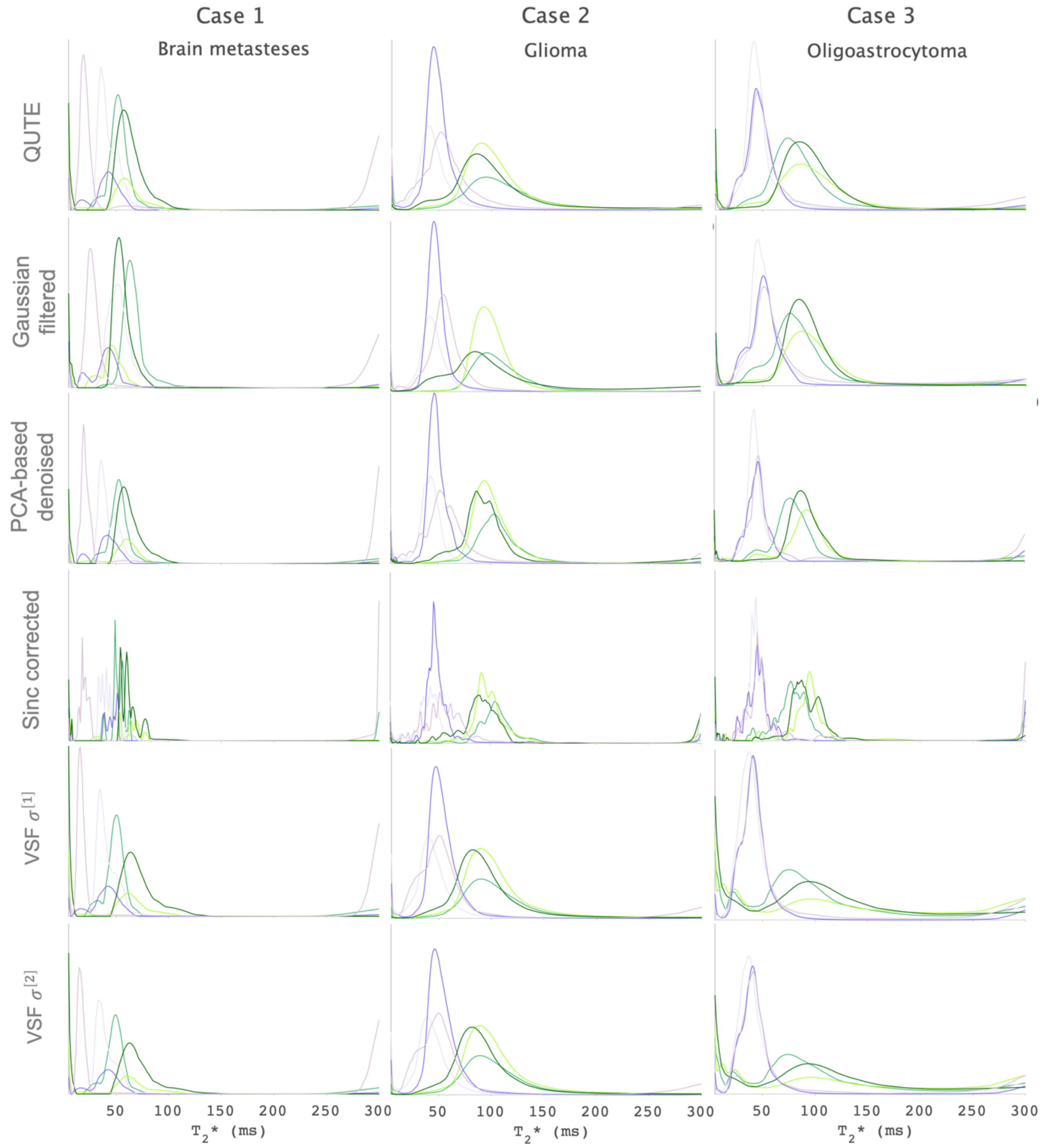

Figure 7.3 - Comparison of the T_2 distributions between the original and corrected data of the manually selected regions of interest of figure 4.22 and the contralateral normal appearing region in 3 cases: brain metastases, glioma and oligoastrocytoma. Vertical axis on T_2* distributions plots is intensity in arbitrary units.*

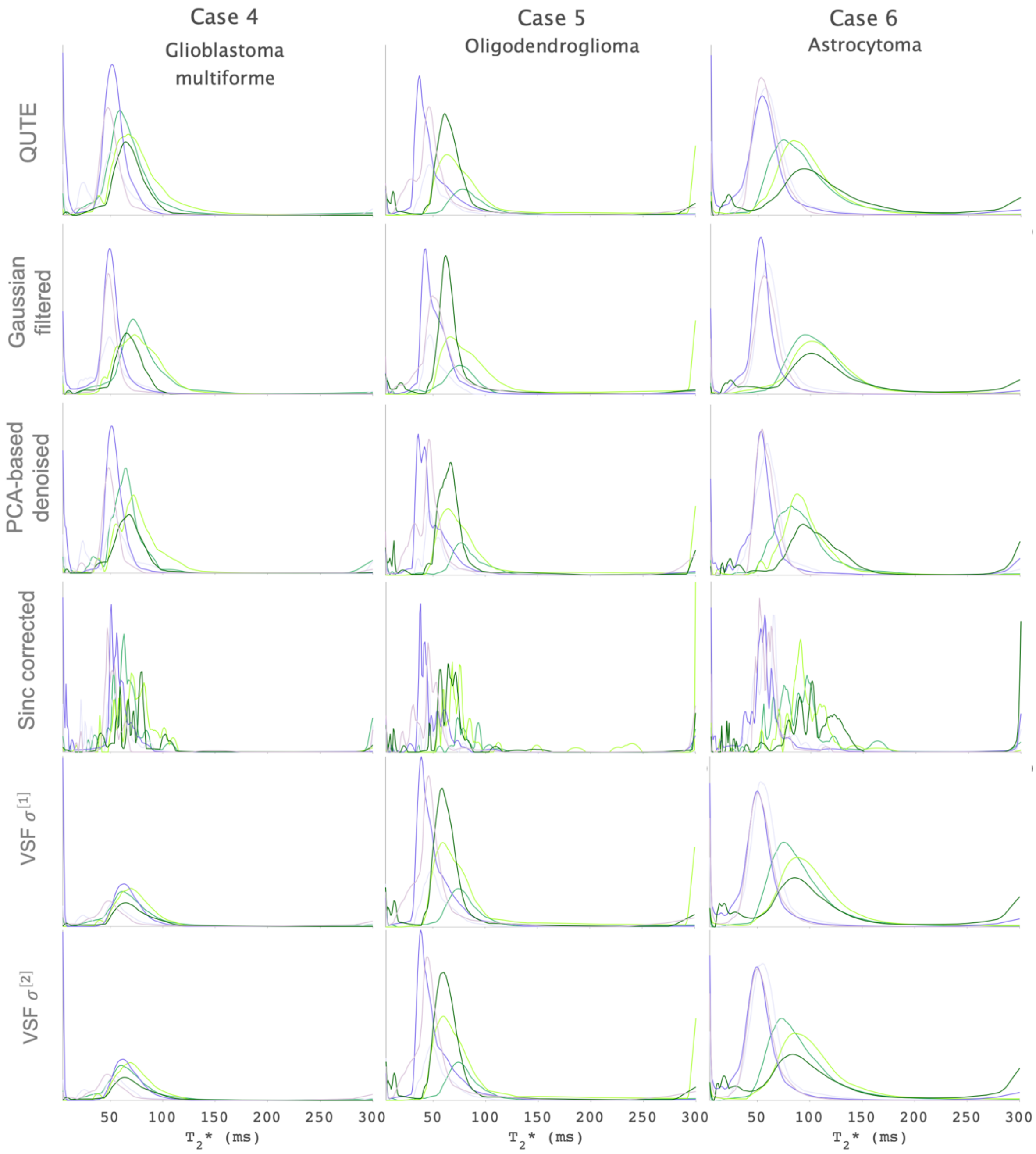

Figure 7.4 - Comparison of the T_2 distributions between the original and corrected data of the manually selected regions of interest of figure 4.22 and the contralateral normal appearing region in 3 cases: glioblastoma multiforme, oligodendroglioma and astrocytoma. Vertical axis on T_2* distributions plots is intensity in arbitrary units.*